Domino Collapse on Historical Masonry Structures in Urban Settings

CIEM0500 – Master Thesis

Aldy Riza Dhiandra

TU Delft

Final Thesis Report: Studying Domino Collapse on Historical Masonry Structure in Urban Settings

Written by:

Aldy Riza Dhiandra (5025958)

This thesis was prepared as part of the MSc programme in Civil Engineering and Geosciences, Delft University of Technology.

Chair: Dr.ir. Paul Korswagen E. (Assist. Prof. Structural Mechanics, 3MD)

Committee Member: Dr. Florentia Kavoura (Assist. Prof. Steel & Composite Structures, ES)

Supervisor: Dr. Abide Aşıkoğlu (Postdoctoral researcher, Structural Mechanics, 3MD)

External committee member: Prof. Dr. Özgür Avşar (Eskişehir Technical University, Türkiye)

Faculty of Civil Engineering and Geosciences, Delft

Cover image: *Adıyaman Ulu Mosque before the earthquake* (Serkan Ficici, 2023, X/Twitter)

TU Delft

Acknowledgement

This thesis owes a great deal to the guidance of my supervisory and committee team. I am especially thankful to **Dr.ir. Paul Korswagen**, **Dr. Florentia Kavoura**, **Dr. Abide Aşıkoğlu**, and **Prof. Dr. Özgür Avşar** for their thoughtful advice, critical questions, and steady encouragement.

To **my wife, Dina**, and my parents: thank you for the love, prayers, and countless small acts of support that kept me going.

I gratefully acknowledge funding from the **Indonesia Endowment Fund for Education (LPDP)**, which made this study possible.

Abstract

This study investigates the seismic performance of the Adıyaman Grand Mosque, a historical masonry mosque in the East Anatolian Fault Zone, with emphasis on its response during the 2023 Kahramanmaraş earthquake sequence. The two main objectives are: (i) to evaluate the mosque's inherent seismic vulnerability in isolation, and (ii) to assess how the collapse of adjacent buildings may have aggravated damage.

The work combines nonlinear static and dynamic analyses in DIANA within a macro-modelling framework using a Total Strain Fixed Crack model calibrated from literature. Pushover analyses establish direction-dependent capacity, drift limits, and mechanism trends; nonlinear time-history analyses capture transient response under recorded ground motion. Neighbouring building collapse was examined through an exploratory numerical study in which a simplified sustained lateral pressure was applied to the south wall during the strong-motion window. The representation is non-calibrated and used to indicate trend-level shifts in demand rather than predictive values.

In isolation, results indicate moderate lateral capacity with strain localisation at openings and roof–wall/dome–drum junctions. Dynamic peaks remain within the pushover plateaus, and control-point drifts lie in a range consistent with no indications of triggering full collapse scenario, noting that principal-strain maps reflect upper-bound transient demand because cracks open and close cyclically. A simplified interaction case was included only as a sensitivity check; because it neglects contact transients, friction, eccentricity and vertical load transfer, no quantitative findings are reported from it. At most, the check suggests that adding a sustained lateral pressure could redistribute demand toward out-of-plane action on the loaded façade. These indications motivate future, higher-fidelity interaction modelling rather than supporting a firm conclusion here. Taken together with field evidence, this supports the interpretation that neighbouring collapse plausibly acted as a trigger for the most severe local failures, while the mosque alone would likely have sustained repairable damage.

The findings clarify seismic risk for historical masonry located in dense urban settings and motivate interaction-aware assessment, including explicit contact or bounded pulse models, to study cascading failure mechanisms.

Table of Contents

List of Figures

List of Tables

1. Introduction

1.1. Research Context

In urban areas with prominent earthquake risk, preserving historical structures, which in many cases were made from masonry, is a challenging issue. These structures are valuable as cultural assets but are particularly vulnerable to seismic events due to their inherent material properties and construction techniques. Urban environments further magnify these vulnerabilities, with the number of surrounding buildings and inadequate design, application or retrofitting solutions often contributing to progressive failures. The Adıyaman Grand Mosque was affected during the 2023 Kahramanmaraş earthquake sequence. It stood in a dense urban block where several neighbouring buildings failed, and photographs show debris of a collapsed reinforced concrete (RC) building found within the mosque's-built area. In this thesis, this interaction is referred to as a "domino effect," meaning damage induced by the collapse of nearby construction. The core analyses, however, consider the mosque as a stand-alone structure; the neighbourhood context is cited only to frame later qualitative comparisons.

Advancements in numerical modelling have increased the understanding of masonry structures' behaviour under seismic loads. Structures of interest are often developed under the assumption that they exist as isolated entities. However, when dealing with historical structures in urban environments, it is crucial to first document the surrounding buildings. This process should include an assessment of their current condition, compliance with seismic design codes, and whether they are structurally substandard. This consideration is especially relevant in Türkiye, where a substantial portion of RC buildings constructed before 1999 are presumed to be substandard, meaning that the seismic code requirements are not satisfied. While research on seismic retrofitting and dynamic analysis of isolated masonry structures has progressed, there is a lack of focus on the interaction between historical buildings and adjacent urban structures during earthquakes. These interactions may amplify stresses, trigger cascading failures, and increase the risk of catastrophic damage to heritage sites.

This research addresses these gaps by employing numerical modelling methodologies to investigate the seismic capacity of historical masonry structures in urban environments. The study focuses on analysing the effects of seismic loading, understanding the structural behaviour of masonry under complex urban conditions, and evaluating the dynamic interactions between adjacent buildings. By exploring these aspects, the study aims to provide actionable insights into mitigating seismic risks while preserving the architectural integrity of historical masonry structures.

1.2. Research Problems

The seismic response of historical masonry structures is inherently complex, involving nonlinear behaviour, progressive damage, and collapse mechanisms. Existing modelling strategies often oversimplify these aspects, making it difficult to capture phenomena such as crack propagation, stiffness degradation, and redistribution of demand. Lourenço (1998) highlighted the importance of robust finite element methods calibrated with field data to realistically simulate these processes. Case studies, such as the Monastery of Jeronimo, further

demonstrate how numerical tools must be able to replicate both material softening and large-scale structural interaction in order to meaningfully assess seismic safety.

First, the challenge lies in assessing the seismic survivability of a historical masonry building in isolation. Many such buildings lack effective diaphragm action, reducing their ability to act as rigid “boxes” under lateral loading. This makes them particularly vulnerable to direction-dependent capacity limits and localised cracking around openings and transitions. For the Adıyaman Grand Mosque, which collapsed during the 2023 Kahramanmaraş earthquake sequence, understanding its isolated performance provides a baseline measure of how much lateral load it could sustain, how it would deform, and which damage mechanisms were most likely to govern.

Figure 1-1 Adıyaman Grand Mosque before the 2023 earthquake

Figure 1-2 Adıyaman Grand Mosque after the 2023 earthquake

Second, the urban context introduces an additional dimension of risk. In densely built settings, neighbouring structures may fail first and impose secondary loads on otherwise stable buildings. In Adıyaman, the collapse of substandard adjacent buildings directly contributed to the failure of the Grand Mosque. This raises the need for strategies to model interaction effects, whether through direct debris impact or equivalent lateral loading. Yet, the timing, location,

and magnitude of such interactions are inherently uncertain, making simplified representations necessary but also limiting.

The two central research problem are therefore: to determine the mosque's seismic survivability when assessed in isolation, and to explore how simplified neighbour-interaction input modifies its seismic demand. Taken together, these perspectives highlight both the intrinsic vulnerability of the structure and the external risks arising from its dense urban surroundings.

1.3. Research Objectives

The main objective of this research is to establish the seismic vulnerability of the Adıyaman Grand Mosque in an isolated analysis by setting up and verifying a finite-element model from available drawings and documentation, and quantifying direction-dependent capacity, deformation capacity, and governing damage mechanisms under monotonic horizontal loading.

While the specific objectives are:

1. Build and assess a finite-element model that reproduces a credible gravity equilibrium and plausible fundamental modal properties, sufficient to proceed to nonlinear analyses.
2. Determine direction-dependent lateral strength and deformation capacity by pushover analysis, reporting for each direction the elastic limit, onset of the post-peak plateau or strength drop, peak base reaction, and the associated control-point drifts; map the façade mechanisms at these stages.
3. Identify and classify governing damage mechanisms, including horizontal cracking along opening and floor levels, diagonal cracking between openings, vertical cracking beside openings, and out-of-plane flexural response of wall segments.
4. Establish an isolated dynamic baseline under recorded ground motion and compare global indicators with the pushover reference, using base reactions, control point drifts, and hysteresis.
5. Evaluate a simplified neighbouring building impact and assess key limitations of the simplified approach.
6. Provide a qualitative estimation of how the identified mechanisms depend on key modelling choices (for example damping, crack model option, assumed neighbour mass and load footprint). A formal probabilistic sensitivity analysis is outside the scope.

1.4. Research Scope

This study concerns the mosque as an isolated building under gravity and monotonic horizontal loading. Self-weight and eigenvalue analyses act as an initial assessment of elastic behaviour before the nonlinear analysis is interpreted.

- Isolated building analysis under gravity and monotonic horizontal loading (pushover).

- Model assessment via self-weight equilibrium (reaction ≈ weight; stress sanity) and modal plausibility (periods, shapes, mass participation).
- Pushover in primary lateral directions with reporting of load factors, drifts, and a possible crack progression.
- Qualitative validation against field evidence on walls that survived.
- Full nonlinear dynamic impact modelling is not undertaken; instead, a simplified approximation is explored and checked for plausibility.

1.5. Research Questions

1. What is the seismic capacity and failure mechanism of the Adıyaman Grand Mosque when analysed in isolation?

   Sub-questions:

   - Does the model exhibit a credible gravity (self-weight) equilibrium state?
   - Are the fundamental modal properties plausible and diagnostic of likely governing façades?
   - What are the elastic limits and peak capacities from pushover per direction?
   - Which cracking/hinge mechanisms develop, and how do they propagate?
   - How do predicted mechanisms compare qualitatively with observed damage on the surviving walls?

2. How do external interaction effects, specifically equivalent loading from the collapse of the adjacent reinforced concrete building, modify the structural response and introduce additional failure mechanisms?

   Sub-questions:

   - How does a sustained one-sided impact load qualitatively change structural response relative to the isolated case?
   - How sensitive are the results to the instant of impact, footprint/height of load, and assumed neighbour participation?
   - Which façade(s) and directions are most affected, and does the damage sequence align with observations?

2. Literature Studies

2.1. Seismic Vulnerability of Historical Masonry

Historical masonry structures are inherently vulnerable to seismic actions due to the brittle nature of their constituent materials. Masonry relies primarily on compressive strength, with very limited tensile and shear resistance. Unlike modern engineered systems, it lacks ductility and energy dissipation capacity, meaning that once cracking initiates, damage can progress rapidly and irreversibly (Tomaževič, 1999; Betti & Vignoli, 2011). This makes the assessment of failure modes under earthquake loading particularly important for understanding the safety of such structures.

Recurring patterns of seismic damage have been documented in past earthquakes. In-plane behaviour is often governed by diagonal cracking or shear sliding within walls, while out-of-plane behaviour can lead to overturning or instability of slender wall panels. Vertical cracks frequently develop near openings due to stress concentrations, further weakening local stability. In many cases, the lack of box behaviour occurs, where walls no longer act as an integrated three-dimensional system but instead deform independently, substantially reducing seismic capacity (Lagomarsino & Cattari, 2015).

Monumental masonry buildings such as mosques, churches, and temples present additional challenges due to their distinctive geometries. Large spans, domes, vaults, and tall minarets introduce stress concentrations and slenderness effects that heighten seismic vulnerability. Domes are highly sensitive to horizontal displacements at their supports, while minarets are especially prone to instability and base cracking under strong shaking. Recent studies of historic mosques in Türkiye have confirmed that minarets are among the most seismically fragile elements, with failures ranging from local cracking to complete overturning (Işık, 2023; Kocaman, 2024).

Regional earthquake evidence reinforces these vulnerabilities. The February 2023 Kahramanmaraş earthquakes caused widespread damage to heritage mosques in the affected region, including partial dome collapses, out-of-plane wall failures, and the toppling of minarets (Işık et al., 2023; İzol et al., 2024). These observations underline the need for numerical models capable of realistically capturing such mechanisms, particularly in cases where detailed material data are unavailable.

Understanding these vulnerabilities is critical not only for interpreting past failures but also for guiding the selection of modelling strategies and analysis methods. The following section (2.2) therefore reviews available approaches to simulate masonry behaviour, ranging from simplified to detailed strategies, and evaluates their suitability for heritage case studies such as the Adıyaman Grand Mosque.

The vulnerabilities outlined above, particularly the recurring in-plane and out-of-plane weaknesses of masonry walls, domes, and minarets, provide the basis for selecting appropriate modelling strategies. Section 2.2 therefore reviews the principal numerical approaches used to represent these mechanisms and assesses their suitability for application to the Adıyaman Grand Mosque.

2.2. Modelling and Analysis

2.2.1. Choice of Modelling Approach

The analysis of historical masonry structures presents unique challenges due to the complex nature of the materials, construction techniques, and often limited documentation of their original design. Numerical modelling is therefore essential to understand their behaviour, preserve their integrity, and ensure continued safety.

Broadly, three numerical strategies are applied in masonry analysis:

1. **Macro-modelling:**
   Masonry is treated as a homogeneous continuum, with properties averaged across units and mortar. This strategy is computationally efficient and suitable for large-scale performance studies, such as assessing the global seismic response of mosques (Kiral et al., 2024). However, it cannot reproduce detailed fracture mechanisms or stress concentrations at the unit level, which limits its accuracy in capturing localised failures under seismic loading (Lourenço, 2011; D'Altri et al., 2020).

2. **Detailed micro-modelling:**
   Masonry units and mortar joints are modelled separately, explicitly capturing stress–strain distributions and crack propagation. This method achieves the highest accuracy but is computationally demanding and requires detailed input data that are rarely available for heritage structures (Lourenço, 2002).

3. **Simplified micro-modelling:**
   This method provides a compromise, modelling units and mortar separately but using interface elements to approximate their interaction. It is more realistic than macro-modelling while remaining more efficient than full micro-modelling (Lourenço, 2002).

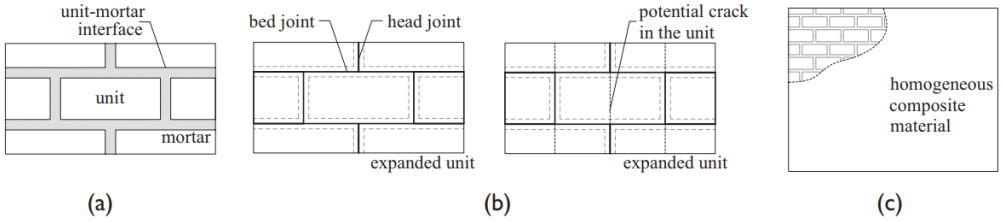

Figure 2-1 Modelling strategies for masonry structures: (a) detailed micro-modelling, (b) simplified micro-modelling without and with potential cracks in units, and (c) macro-modelling (Lourenço & Gaetani, 2021)

Given the objective to capture the global seismic response of the mosque with credible damage mechanisms at façade and roof level, a macro-modelling strategy with a Total Strain Crack (TSC) formulation is adopted. In TSC models, cracking and crushing are represented by a reduction of stiffness within the finite elements rather than by discrete discontinuities, which reproduces overall stiffness loss, cyclic degradation, and the spatial distribution of damage typical of masonry aggregates under seismic actions (e.g. Lourenço, 2002; Betti & Vignoli, 2011; D'Altri et al., 2020).

A fixed-crack concept is used so that, once initiated, the crack orientation remains constant during subsequent loading. This avoids artificial crack rotation or unreal "healing" under reversing cycles, yields a conservative envelope of post-peak stiffness, and is a standard option for masonry in DIANA (DIANA User Manual, Total Strain Crack models). This choice aligns

with the study aim of robust global trends rather than exact local crack kinematics. The adopted uniaxial law consists of exponential tensile softening governed by fracture energy, parabolic compression with softening, and reduced shear stiffness, as sketched in Fig. 2-X; the parameter values and sources are listed in Section 3.2.

2.2.2. Analysis Method

The choice of analysis method determines how the seismic behaviour of masonry structures is evaluated and is strongly linked to both the objectives of the study and the available computational resources. In the literature, several approaches are widely employed for unreinforced masonry (URM), ranging from simplified elastic approximations to fully nonlinear dynamic simulations (Lourenço, 2002; Lagomarsino & Cattari, 2015).

1. **Linear Elastic Analysis**
   This is the most straightforward method, assuming elastic material behaviour and small deformations. It provides valuable information on global stiffness, modal properties, and mode shapes, which help identify potential weaknesses in the structure. However, linear elastic analysis cannot capture inelastic processes such as cracking, plastic deformations, or post-peak softening, making it unsuitable for performance-based seismic assessment of brittle URM (Roca et al., 2010).

2. **Nonlinear Static Analysis (Pushover)**
   Pushover analysis is extensively used for heritage buildings due to its balance between simplicity and capacity to approximate nonlinear behaviour. A monotonically increasing lateral load is applied until collapse or a target displacement is reached, producing a capacity curve that reflects the structure's strength and deformation capacity. This method is particularly effective in identifying weak zones, global capacity, and hinge/crack formation mechanisms. Its main limitation is that it assumes a predefined lateral load distribution and cannot capture higher-mode effects or time-dependent degradation (Fajfar, 2000; Lagomarsino & Cattari, 2015).

3. **Nonlinear Dynamic Analysis**
   NLTHA offers the most detailed insight by applying ground motion records directly to the structure in the time domain. It captures cyclic degradation, progressive cracking, and redistribution of stresses, thereby overcoming some limitations of pushover. However, NLTHA is computationally demanding, requires careful input selection, and results are highly sensitive to modelling assumptions (Betti & Vignoli, 2011; D'Altri et al., 2020).

Table 2-1 Summarises the main analysis methods applied to unreinforced masonry

Method	Strengths	Limitations	Typical Applications
Linear Elastic Analysis	Simple, fast; provides modal properties and stiffness	Cannot capture cracking or post-peak behaviour	Preliminary assessment, identification of weak zones
Nonlinear Static Analysis (Pushover)	Provides capacity curve, collapse mechanisms, global strength; relatively efficient	Assumes predefined lateral load distribution; ignores higher modes	Performance-based assessment, identification of weak mechanisms
Nonlinear Time History Analysis (NLTHA)	Most realistic; captures cyclic degradation, progressive cracking	Computationally expensive; sensitive to input motions and modelling assumptions	Detailed seismic response studies, validation of pushover results

In practice, pushover and NLTHA are often used in combination: pushover provides a rapid estimate of global capacity, while NLTHA delivers a detailed response under realistic seismic input. This combination is particularly suitable for heritage masonry, where both global performance and localised damage patterns must be assessed. Other approaches, such as limit analysis, are also cited in the literature (e.g. Milani, 2011), but are not within the scope of this thesis.

2.2.3. Seismic Behaviour of Masonry Structures

The seismic performance of masonry is governed by its brittle nature, negligible tensile capacity, and dependence on wall-to-wall and wall-to-roof connections. A substantial body of research documents recurrent failure mechanisms in historic structures, many of which are directly applicable to mosques and minarets.

Foundational studies (Tomazevic, 1999; Lourenço, 2011; Betti & Vignoli, 2011; Aşıkoğlu et al., 2020) consistently identify both in-plane and out-of-plane behaviours, illustrated schematically in Figure 2-2.

- **In-plane shear cracking:** Diagonal cracks form across wall panels as a result of shear forces. These are often the earliest indicators of structural degradation (Lourenço, 2011).
- **Diagonal tension and sliding:** Horizontal or stepped cracking develops near openings due to stress concentrations; commonly reported in post-earthquake field surveys (Betti & Vignoli, 2011; Aşıkoğlu et al., 2020).
- **Out-of-plane mechanisms:** Out-of-plane mechanisms: Walls lose stability by out-of-plane flexural rotation (rocking) when floor-to-wall or roof restraints are inadequate. This behaviour is particularly critical in tall façades and slender minarets (Kocaman, 2024).
- **Cracking beside openings:** Vertical cracks along door and window edges reflect tensile overstress (Kocaman, 2024).
- **Lack of box behaviour:** Separation at wall intersections undermines global stability, a frequent cause of collapse in monumental structures such as churches and mosques (Işık et al., 2023).

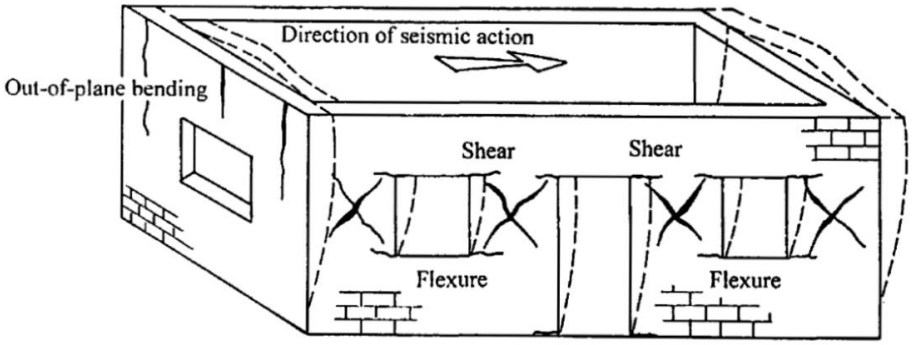

Figure 2-2 Common seismic failure mechanisms in unreinforced masonry walls, showing in-plane shear, diagonal tension, flexural cracking, and out-of-plane bending (Tomaževič, 1999).

These mechanisms have been observed across both static pushover and dynamic analyses, though their relative severity may differ. Reports from the 2023 Türkiye earthquakes confirm that mosques and minarets often sustain cracking at domes and drum–wall junctions, underlining the need to evaluate both global stability and localised responses (Ergün & Tayfur, 2024; Kocaman et al., 2024).

2.2.4. Numerical Model Implementation

The choice of numerical implementation strongly influences the ability of a model to reproduce realistic masonry behaviour under seismic loading. A widely applied formulation for unreinforced masonry is the Total Strain Crack (TSC) model, which represents cracking through a smeared-crack continuum approach. The TSC formulation can be implemented in two orientations: fixed or rotating, each with distinct implications for post-cracking behaviour.

The fixed crack model maintains the crack orientation after it has formed, preventing "healing" when the loading direction changes. This results in more conservative predictions, as cracks persist in their original orientation and continue to influence the material response. The rotating crack model, by contrast, allows the orientation of cracks to adjust with the changing principal strain direction, often producing smoother stress–strain curves but at the risk of underestimating persistent local damage (Lourenço & Gaetani, 2021; Betti & Vignoli, 2011). A comparison of the two formulations is presented in Table 2-2.

Table 2-2 Comparison of Crack Models in FEA Environment

Crack Model	Strengths	Limitations	Typical Applications
Fixed	Preserves crack orientation once initiated, ensuring persistence and avoiding unrealistic "healing"; conservative post-peak behaviour; consistent with brittle masonry failure modes.	May produce stiffer post-peak response; less adaptable to changing principal stress directions.	Heritage masonry, seismic loading cases with dominant pre-existing weaknesses (e.g. around openings and junctions).
Rotating	Adjusts crack orientation with changing principal stresses; more flexible representation of stress redistribution; smoother convergence.	Can allow unrealistic crack "healing" under cyclic or reversed loads; less conservative for brittle systems.	Reinforced concrete, ductile materials, cases with significant stress redistribution

For this study, the fixed TSC model is adopted in combination with a macro-modelling strategy. This decision reflects the emphasis on capturing global structural response of the Adıyaman Grand Mosque, including drifts, base reactions, and strain localisation, while maintaining computational feasibility. The fixed crack formulation provides a conservative and physically consistent representation of progressive cracking in masonry, which is especially important when assessing the vulnerability of tall façades, domes, and minarets under seismic actions.

The choice of DIANA as the modelling platform is consistent with its established application in heritage masonry research. Previous studies (Lourenço et al., 2011; Betti & Vignoli, 2011) have demonstrated DIANA's reliability in simulating the nonlinear seismic response of unreinforced masonry, including both pushover and nonlinear dynamic analyses. The software's dedicated library for brittle materials and proven record in masonry case studies make it particularly suited for this investigation.

This selection also sets the foundation for the methodological framework presented in Section 3, where the DIANA environment is used to implement pushover and dynamic analyses. The combination of macro-modelling with a fixed TSC model enables the study to realistically capture both the global performance and the localised vulnerabilities of the mosque under isolated and interaction scenarios.

For building-scale models of historic masonry, a smeared-crack continuum is widely used to capture stiffness loss, cyclic degradation, and the spatial spread of damage without resolving unit-mortar interfaces. In the Total Strain Crack (TSC) family, cracking and crushing are represented by reductions of element stiffness driven by the total strain, which is well suited to global mechanism interpretation under seismic actions reported in the literature. Within TSC, two orientations are common: fixed-crack, which keeps the crack direction once formed and avoids unrealistic "healing" under load reversals, and rotating-crack, which lets crack orientation follow the evolving principal strain. For brittle masonry where persistence of cracks is critical and conservative post-peak envelopes are acceptable, the fixed-crack option is generally preferred in macro-FE assessments. The present study therefore, adopts a fixed TSC formulation for the mosque model. The specific uniaxial laws and parameter values are given later in Section 3.2.

While the choice of modelling strategy and numerical implementation defines how internal behaviour of the structure is captured, the external context must also be considered. In dense urban settings such as Adıyaman, seismic interaction with neighbouring buildings may significantly alter demand distribution. Section 2.3 therefore examines the literature on pounding and secondary impact, clarifying why simplified interaction loads are adopted in this study.

2.3. Neighbouring Buildings and Seismic Interaction

The seismic performance of masonry structures cannot be fully understood in isolation when located in dense urban contexts. Interactions with neighbouring buildings or detached elements often play a significant role in redistributing seismic demand, particularly when separation gaps are insufficient. This interaction, commonly referred to as structural pounding, has been widely

documented as a critical phenomenon during earthquakes (Miari et al., 2019; Brown & Elshaer, 2022).

Pounding can alter the dynamic equilibrium of adjacent structures by constraining relative displacements or transferring abrupt forces at points of contact. Studies confirm that the severity of impact outcomes depends strongly on relative stiffness, geometry, vibration phase, and wall-to-floor connections (Abdel Raheem et al., 2019; Manjatakis et al., 2018). In masonry aggregates, this behaviour is further complicated by irregularities in building typology and the vulnerability of façade openings and corners. Numerical and discrete element studies have demonstrated that pounding may reduce global displacements but simultaneously intensify localised damage at vulnerable connections (Malomo & DeJong, 2024; Bianchini et al., 2024).

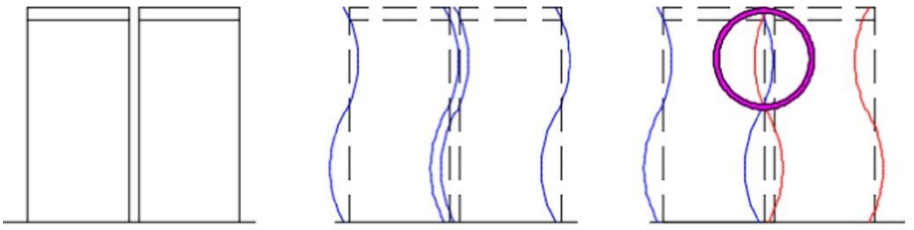

Figure 2-3 General schematics of seismic pounding showing (a) buildings before earthquake, (b) in-phase vibrations, and (c) out-of-phase vibrations leading to contact. (Miari et al., 2019)

While structural pounding is a widely recognised interaction mechanism in dense urban aggregates, it generally requires very small separation gaps that allow direct wall-to-wall contact (Maison & Kasai, 1990; Anagnostopoulos, 1996; Miari et al., 2019; Brown & Elshaer, 2022). In the present case, the spacing between the Adıyaman Grand Mosque and the neighbouring reinforced-concrete buildings cannot be categorised as a dilatation gap normally left between adjacent buildings. This geometric condition makes direct pounding an unlikely primary contributor to the observed damage.

Instead, the more credible interaction mechanism is secondary impact loading, where partial collapse or debris from the adjacent buildings imposes concentrated local stresses on the mosque's façades and minaret (Ezzelarab & Griffith, 2019). In masonry contexts this is better represented as sustained one-sided pressing and/or debris impact rather than cyclic contact (Malomo & DeJong, 2024; Bianchini et al., 2024). Pre-earthquake photographs show a paved roadway separating the mosque from the adjacent reinforced-concrete building (Figure 2-4), indicating a street-scale open space rather than a narrow construction joint. This site condition further disfavours classical wall-to-wall pounding and motivates treating neighbour interaction as debris-induced loading.

Figure 2-4 Adıyaman Grand Mosque and surrounding reinforced-concrete buildings before the 2023 Kahramanmaraş earthquakes, illustrating building gaps that exceed typical thresholds for pounding interaction. Source: Cultural Inventory (Ahmet Yurtbakan, Caner Cangül, Inan Kenan Olgar), kulturenvanteri.com

Such findings are particularly relevant to historic mosques, where minarets or adjacent structures may fail first and transmit sudden loads to the main prayer hall. While most pounding studies have focused on conventional urban aggregates, the application of secondary impact mechanisms to monumental heritage remains limited. For historical structures such as mosques, the potential for impact-induced demand redistribution remains understudied, despite field observations suggesting that debris from neighbouring structures may contribute to partial wall failures.

This context motivates a simplified approach that captures the essential effect of neighbour interaction without prohibitive contact modelling. In this study, the interaction is represented as a sustained lateral loading applied to the south façade over the strong-motion window, rather than as explicit transient contact. This choice is consistent with the methodological framework presented in Chapter 7.

2.4. Literature Review Summary

Research on historical masonry has long sought to explain how these structures behave under seismic loading and how their performance can be assessed at the building scale. Foundational contributions by Lourenço (1998, 2001, 2002) established the mechanics and modelling of masonry, tracing the evolution from simple thrust-line methods to nonlinear finite element simulations suitable for entire buildings. These works, together with case-based studies, emphasise that nonlinear analysis can only be relied upon when its assumptions are transparent and verification steps are carefully performed (Lourenço et al., 2006; Betti & Vignoli, 2011).

Comparative reviews of modelling strategies consistently highlight the balance between efficiency and physical realism. Macro-continuum approaches are often recommended for global capacity assessment, provided their limitations are clearly recognised and validation is

undertaken (Giamundo et al., 2014; D'Altri et al., 2020). Applications on historic churches and earthen structures demonstrate that these models can reproduce both overall capacity and critical mechanisms, especially when results are interpreted in terms of deformation patterns rather than isolated peak values (Silva et al., 2018; Karamnikoloudis & Lourenço, 2018).

For mechanism interpretation, the literature identifies recurring patterns such as in-plane shear sliding, diagonal tension and splitting beside openings, and out-of-plane instability at upper wall or floor-to-wall connections (Lourenço, 2011; Betti & Vignoli, 2011; Aşıkoğlu et al., 2020). These mechanisms are practical references for interpreting crack maps and simulation outputs, enabling comparison with field surveys. Studies on post-earthquake damage and retrofitting provide further evidence of these weaknesses, particularly the decisive role of poor box behaviour in façades (Ergün & Tayfur, 2024; İzol et al., 2024). Reports from the 2023 Türkiye earthquakes confirm these vulnerabilities in mosques and minarets, strengthening the link between simulated mechanisms and observed failures (Işık et al., 2023; Kocaman, 2024).

In methodological terms, these sources inform how this thesis structures its analyses. The model is first checked under self-weight and eigenvalue analysis to ensure a credible starting point, then nonlinear pushover simulations are performed in each principal direction to establish lateral capacity, deformation limits, and failure mechanisms. These results are interpreted using the mechanism language developed in the literature and compared qualitatively with field evidence from surviving walls (Silva et al., 2018; Işık et al., 2023). Subsequently, nonlinear time history analysis (NLTHA) extends the investigation by applying seismic input and incorporating simplified interaction loads, enabling the study of demand redistribution beyond the pushover stage.

International guidelines such as the ISCARSAH Recommendations (ICOMOS, 2003) emphasise that heritage assessments must integrate engineering judgement, qualitative interpretation, and careful validation. This principle is particularly relevant for monumental mosques, where domed prayer halls and slender minarets combine in-plane and out-of-plane vulnerabilities. Field observations confirm that the dome-to-drum interface and adjacent wall panels attract high stresses, while minarets are prone to cracking or overturning under strong shaking (Kocaman, 2024; Işık et al., 2023). These typological sensitivities reinforce the need to interpret nonlinear results not only in terms of global strength but also through the lens of architectural configuration.

Overall, the literature confirms that pushover and NLTHA are robust tools for assessing the seismic capacity of historical masonry. However, gaps remain in their application to Ottoman-era mosques, where slender minarets and dome–drum connections introduce distinctive vulnerabilities, and where the effects of neighbouring building interaction are seldom addressed systematically. This thesis positions itself within these gaps, combining established nonlinear modelling strategies with a simplified interaction framework tailored to the Adıyaman Grand Mosque.

The literature review thus highlights both the strengths of established nonlinear analysis methods and the gaps that remain in their application to monumental mosques and interaction scenarios. These insights frame the specific research framework presented in Section 2.5 and provide the methodological foundation for the analyses described in Chapter 3.

2.5. Research Framework

From as-built sources, a 3D geometry is built and checked for consistency and units, then partitioned and exported to DIANA for material definition, boundary conditions and meshing. An analytical model check confirms mesh quality and a stable gravity run before analysis continues (pass if: geometry closed and connected, mesh within quality limits, gravity solution converges, base reactions ≈ total weight within a small tolerance, no unintended uplift). A detailed overview of the preparation framework is evident in

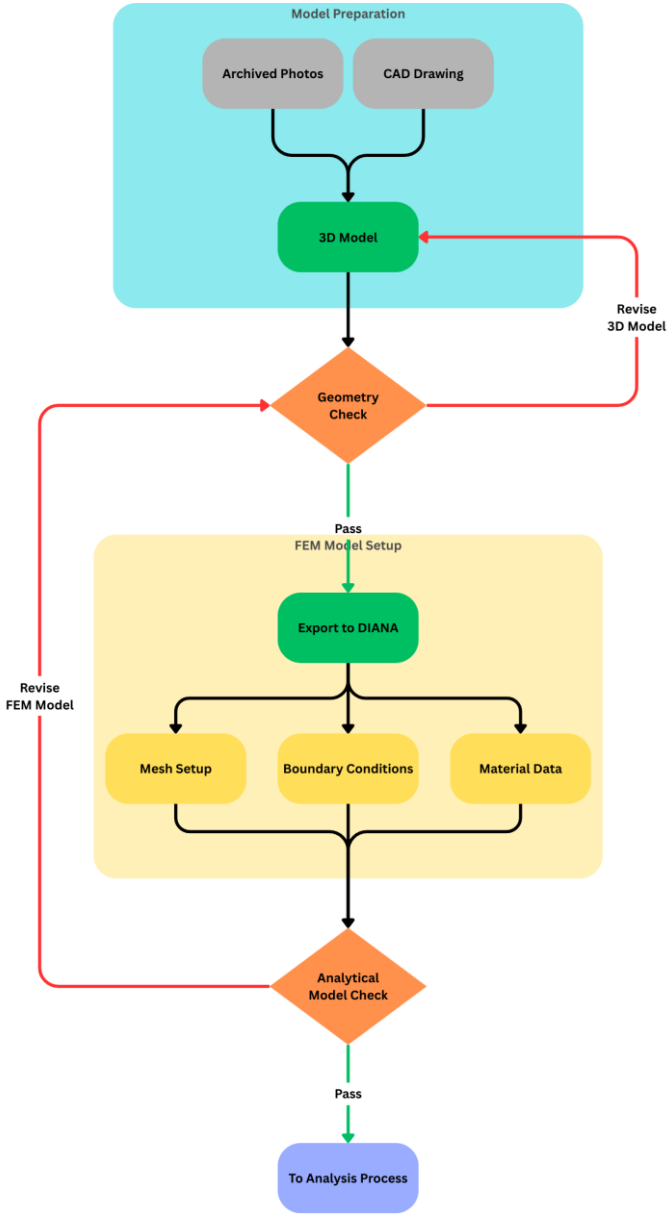

Figure 2-5 Preparation Framework

The verified model undergoes self-weight, and eigenvalue checks as entry gates. Self-weight confirms reaction–weight balance and plausible thrust paths. Modal results confirm plausible periods, global first modes and adequate cumulative mass participation in the loading directions. On passing these checks, direction-dependent pushover analyses (X±, Y±) are run with defined control DOFs. Outputs are capacity curves and mechanism maps read from principal tensile strain and crushing fields to identify in-plane and out-of-plane hinge patterns.

Figure 2-6 Analysis Framework

3. Research Methodology

This section sets out the methodology used to build and check the finite-element model of the Adıyaman Grand Mosque. It describes the geometry and partitioning from the available documentation, the FE model setup (element types, material model and parameters), boundary conditions, mass definition and meshing. It then defines the verification checks to be applied under self-weight and eigenvalue analysis, followed by the pushover configuration in X± and Y±, the selected monitors, and the post-processing metrics that will be used to interpret results in later chapters. No analysis outcomes are reported here, only the procedures, assumptions and acceptance criteria.

Before the structural analysis process can take place, a numerical model to represent the structure needs to be prepared. Several types of models can be generated based on computational requirements and the level of detail within the analysis. A 3D model is preferred for a more detailed overview of the structure on the macro-analysis level, with expected heavier computational loads and a more complex model. A simpler model will also be prepared to form the basis of a sanity check for the full 3D model.

3.1. Geometry Modelling

This subsection describes how the building geometry was assembled from the available floor plans and photographic records, how the model was partitioned for analysis, and which simplifications were applied to ensure a reliable mesh in DIANA. All dimensions are in mm unless stated otherwise, and the global axes are defined as X east–west, Y north–south, and Z vertical.

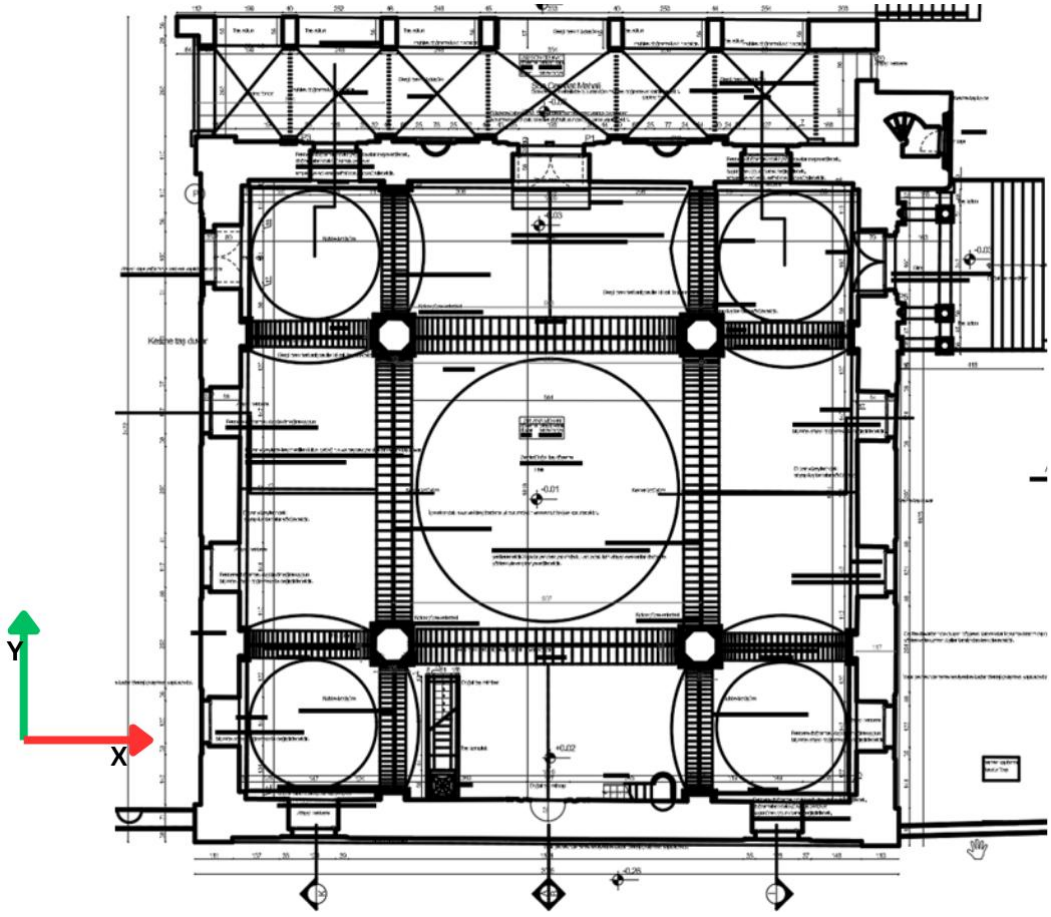

Figure 3-1 Floor plan from restored drawing

The global geometry was reconstructed from the restored drawings and cross-checked against archived photographs to confirm features not explicit in the plans (Figure 3-1, Figure 3-3). Where drawings and photos conflicted, priority was given to the most recent measured information. Small ornamental features and sub-unit irregularities were omitted where they do not affect global stiffness or load paths. The 3D model was created in Revit and exported to DIANA for analysis. Using CAD first was deliberate: it handles compound curved elements (arches, vaults, drum and dome) more reliably than direct modelling in an FE pre-processor and reduces the chance of geometric artefacts that later destabilise the mesh.

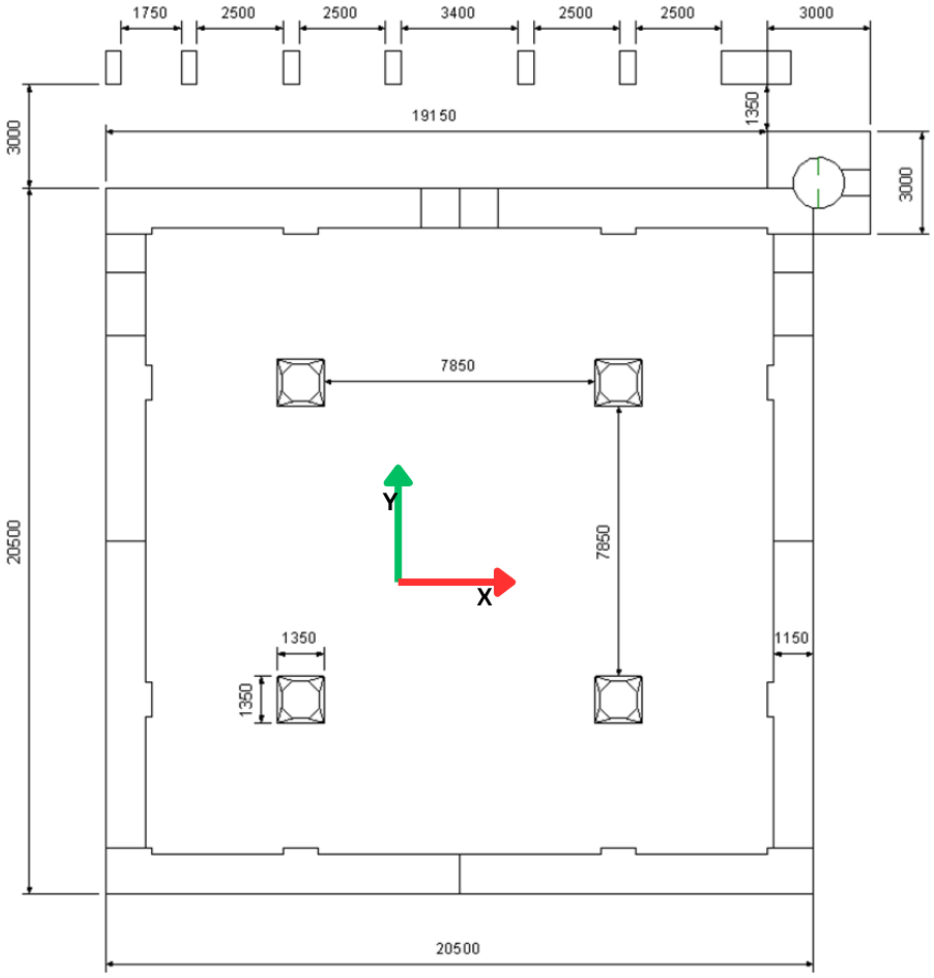

Figure 3-2 Design floor plan used in the model

To keep the FE model tractable, several controlled simplifications were introduced. They target meshing feasibility and numerical robustness while preserving the load-bearing intent. The main differences between the drawings and the analysis model are summarised in Table 3-1 below.

Table 3-1 Difference between drawing and 3D model

No	Comparison	Drawing	3D Model
1	Floor Plan	Non-rectangular	Rectangular
2	Wall thickness	Uneven	Consistent
3	Columns crown	Appears	Removed/Smoothed
4	Arches/Vaults	Ellipsoid with sharp peak	Smooth circular
5	Wall railings (Minaret)	Appears	Removed
6	Dome transition	Sharp angles	Smooth curve

Following Table 3-1, the analysis model regularises the slightly skewed plan to a near-rectangular footprint and homogenises wall thickness by storey, which improves element quality and avoids artificial stress peaks at abrupt offsets. Curved masonry (arches, vaults, and the dome transition) is rendered with smoothed circular or filleted profiles rather than sharp ridges to prevent geometric singularities and stabilise the mesh (Figure 3-3 and Figure 3-4).

Purely architectural details such as crowns, railings, and small mouldings are omitted because they add meshing complexity without influencing global stiffness or capacity.

The model therefore retains the structurally active core, including load-bearing walls and their openings, arches and vaults, the drum and dome, and any abutment portions that provide restraint, while excluding minor surface features and undulations with negligible effect. These idealisations keep the geometry faithful to the structural intent yet efficient and numerically robust for the DIANA analyses that follow.

These choices were guided by practical meshing feasibility, the need for numerical stability in curved regions, and a focus on structurally relevant components.

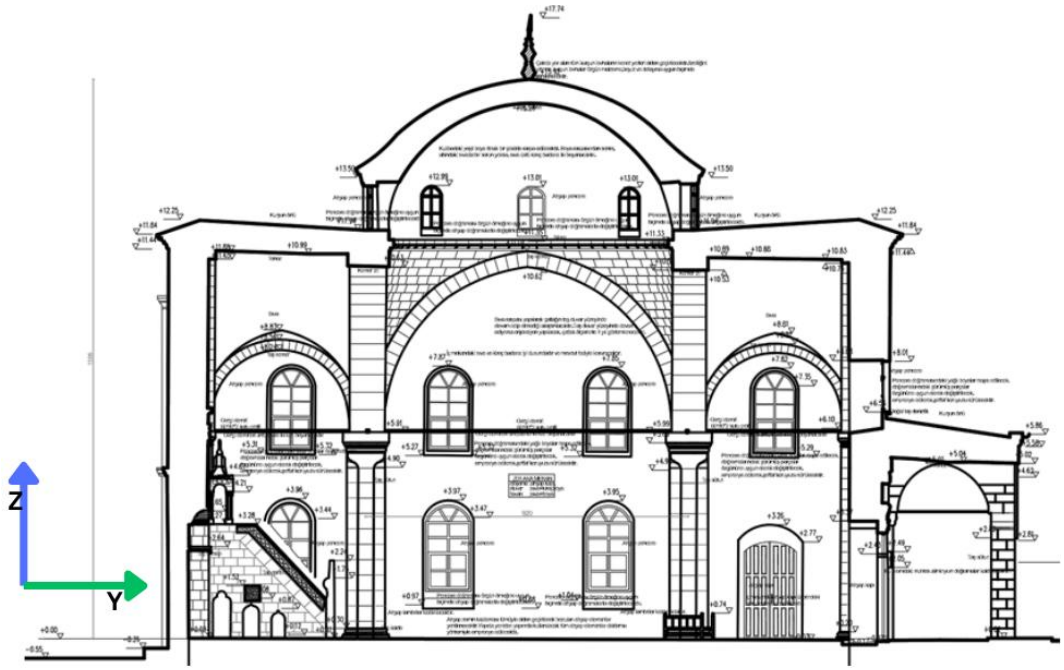

Figure 3-3 Cross-section view of the mosque

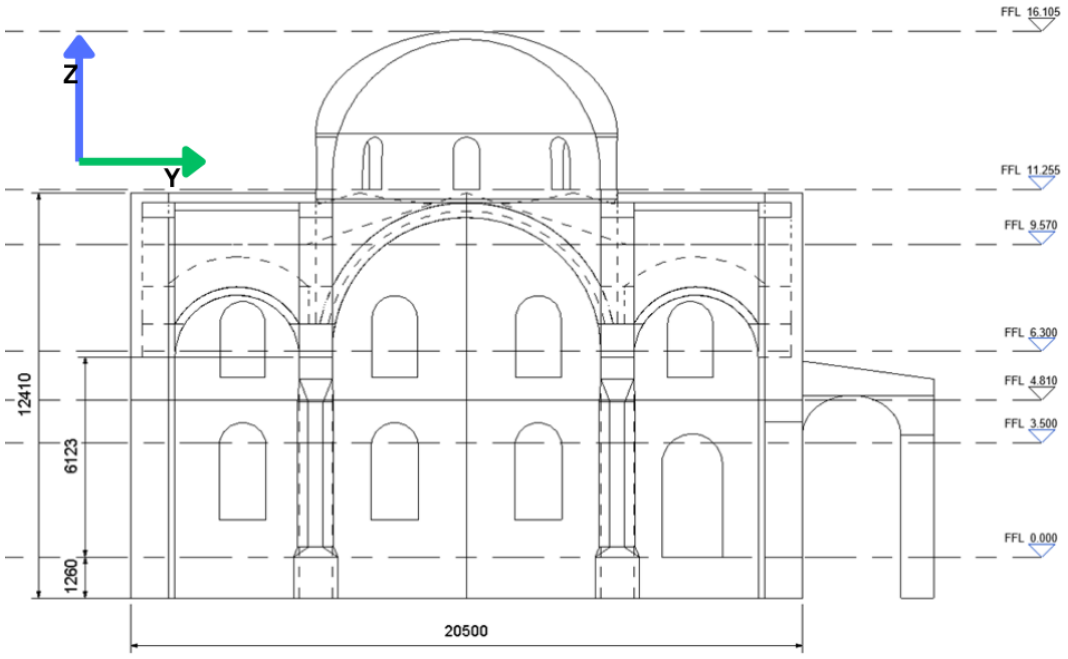

Figure 3-4 Interior view of the mosque (3D model)

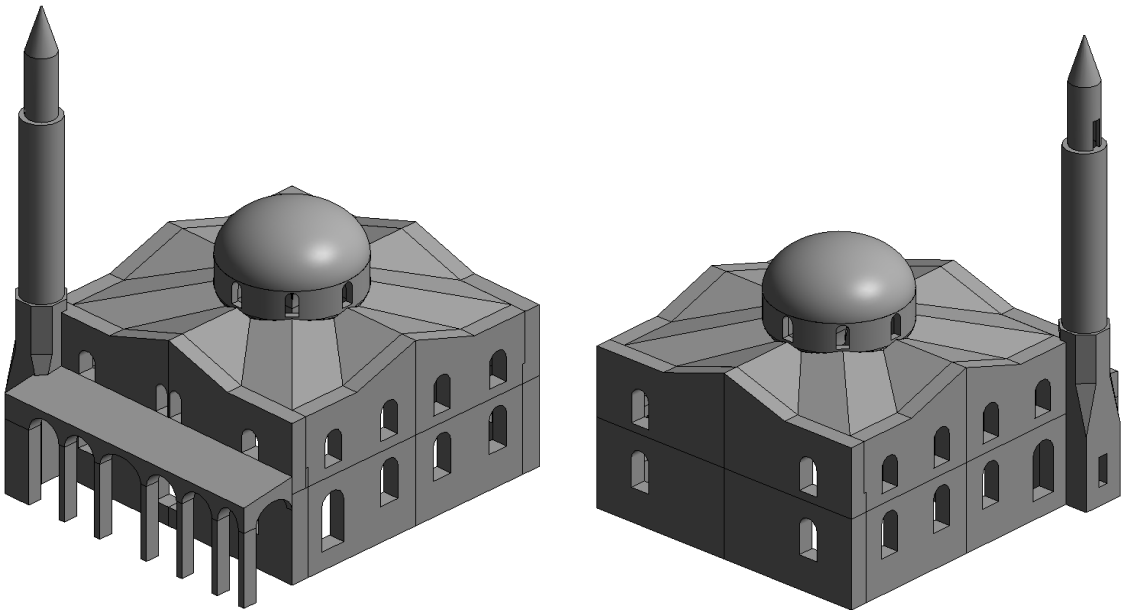

Figure 3-5 The 3D model of the mosque from the "rear" (left) and "front" (right)

3.2. Material Properties

This subsection defines the material sets adopted for the FE model, their mapping to the building parts, and the constitutive options used in DIANA. Values follow recommended ranges for historic masonry, as seen in Figure 3-6 (Lourenço & Gaetani, 2021) and are refined against gravity and modal checks, with the full numbers reported in Table 3-3 to Table 3-5.

Masonry typology	f_c [MPa] min–max	f_{v0} [MPa] min–max	E [MPa] min–max	G [MPa] min–max	ρ [kN/m^3] min–max
Irregular stone masonry (pebbles, erratic, irregular stones)	1.0–2.0	-	690–1,050	230–350	19
Uncut stone masonry with inhomogeneous thickness of leaves	2.0	-	1,020–1,440	340–480	20
Regular stone masonry with good bonding	2.6–3.8	-	1,500–1,980	500–660	21
Soft stone masonry (tuff, limestone, etc.)	1.4–2.2	-	900–1,260	300–420	13–16
Regular soft stone masonry (tuff, limestone, etc.)	2.0–3.2	0.10–0.19	1,200–1,620	400–500	
Dressed rectangular (ashlar) stone masonry	5.8–8.2	0.18–0.28	2,400–3,300	800–1,100	22
Solid brick masonry with lime mortar	2.6–4.3	0.13–0.27	1,200–1,800	400–600	18
Hollow bricks (voids < 40%) with cement mortar	5.0–8.0	0.20–0.36	3,500–5,600	875–1,400	15

Source: Circolare (2019).

Figure 3-6 General mechanical properties of masonry (Lourenço & Gaetani, 2021)

Dressed rectangular masonry and solid brick masonry with lime mortar are chosen as these two topologies are closely similar to ones present in the actual mosque structure. A larger value from the range is chosen for a more conservative approach. Details of material topology used for the modelling different parts of mosque are as shown in Table 3-2 below.

Table 3-2 Summary of Material used on the 3D model

No	Material Topology	Elements
1	Cut Stone (Dressed rectangular stone masonry)	a. Exterior walls b. Interior columns c. Minaret d. Rear canopy
2	Clay Brick (Solid brick masonry with lime mortar)	a. Interior arches b. Interior domes c. Exterior dome
3	Cast Iron	a. Lintels (walls) b. Ring bars (dome) c. Tying bars (arches)
4	Soil Infills	Roof infills

Where for cast iron and soil infills, linear isotropic approaches will be used as the two remaining materials are not integral for the analysis of masonry structures. Lourenço & Gaetani

(2021) also noted that for macro modelling analysis of masonry, where the material will be considered as isotropic, fracture energy variables will be calculated to represent material behaviour, especially to capture softening and crack propagation that will be important to analyse how damage may have formed in the structure.

Young's modulus	$E = 500\text{-}800\ f_c$	MPa	
Poisson's ratio	$\nu = 0.2$	-	
Compressive strength	$f_{c,M} = 0.54 f_{c,b}^{0.7} f_{c,m}^{0.3}$	MPa	See Eq. (4.10) and the following sections
Fracture energy in compression	$G_c = \frac{32 f_{c,M}}{10 + f_{c,M}}$	N/mm	Eq. (4.1)
Flexural to tensile strength	$f_t = \frac{0.06 h^{0.7}}{1 + 0.06 h^{0.7}} f_{fl}$ (h in mm)	MPa	Eq. (4.2)
Tensile strength	f_t	MPa	Equal to interface bond tensile strength of Table 4.25, if available
Fracture energy in tension	$G_f^I = 0.02$	N/mm	
Hardening–softening criteria for both compression and tension (σ–ε diagrams)	Parabolic for compression and exponential for tension		

Note: h is the height of the specimen adopted in flexural testing; f_{fl} is the flexural strength; subscripts b, m and M indicate unit, mortar and masonry, respectively.

Note that the compressive strength f_c must be given in MPa and the height h must be given in mm.

Figure 3-7 Mechanical properties for macro-modelling approach of masonry as an isotropic material (Lourenço & Gaetani, 2021)

Masonry is modelled with the Total Strain Fixed Crack (TSFC) formulation. The adopted response is:

- Tension: exponential softening governed by the tensile fracture energy G_f to control post-peak dissipation.
- Compression: parabolic hardening up to f_c followed by softening to represent crushing.
- Shear: linear elastic with reduced tangent stiffness and shear-retention across cracked zones.

The softening branches are energy-regularised using the element crack bandwidth $h = \sqrt{A}$ (with A the in-plane element area), so that the area under the post-peak stress–strain curves correspond to the specified fracture energies. Following the recommendations for macro-modelling of masonry (Lourenço & Gaetani, 2021, Eq. 4.1 and Table 4.2), the values adopted are

$$G_f = 0.02\ N/mm, \qquad G_c = \frac{32 f_{c,M}}{10 + f_{c,M}} N/mm,$$

with $f_{c,M}$ in MPa. In DIANA these inputs are per unit thickness; the tension and compression softening curves in Figure 3-8 were calibrated so that, when converted with h, they dissipate G_f and G_c, respectively.

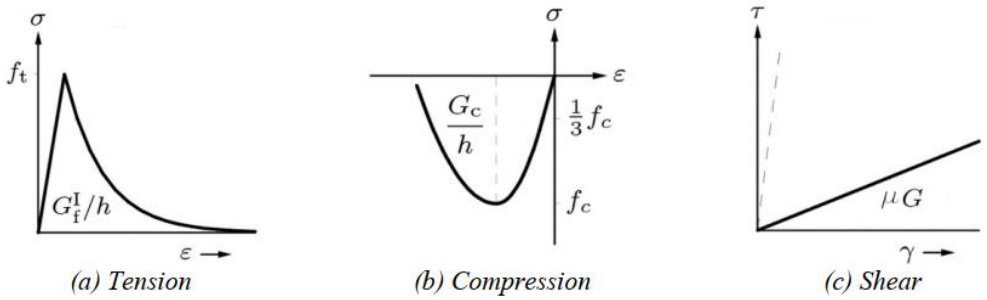

Figure 3-8 Adopted behaviour for masonry material (Aşıkoğlu, 2018)

A detailed summary of material properties for numerical modelling is evident from Table 3-3 through Table 3-5 below.

Table 3-3 Detailed overview of cut stone masonry

Cut Stone		
Parameters	**Value**	**Unit**
Young's Modulus (E)	3300	MPa
Poisson's Ratio (ν)	0.2	-
Mass Density (ρ)	22	kN/m^3
Compressive Strength (f_c)	8.2	MPa
Compressive Fracture Energy (G_c)	14.417	N/mm
Tensile Strength (f_t)	0.82	MPa
Tensile Fracture Energy (G_f^I)	0.02	N/mm

Table 3-4 Detailed overview of clay brick masonry

Clay Brick		
Parameters	**Value**	**Unit**
Young's Modulus (E)	1800	MPa
Poisson's Ratio (ν)	0.2	-
Mass Density (ρ)	18	kN/m^3
Compressive Strength (f_c)	4.3	MPa
Compressive Fracture Energy (G_c)	9.622	N/mm
Tensile Strength (f_t)	0.43	MPa
Tensile Fracture Energy (G_f^J)	0.02	N/mm

Table 3-5 Detailed overview of cast iron and roof infills.

Cast Iron		
Parameters	**Value**	**Unit**
Young's Modulus (E)	110,500	MPa
Poisson's Ratio (ν)	0.26	-
Mass Density (ρ)	70.6	kN/m^3
Roof Infills		
Parameters	**Value**	**Unit**
Young's Modulus (E)	1.9	MPa
Poisson's Ratio (ν)	0.33	--
Mass Density (ρ)	17.66	kN/m^3
Porosity	0.35	

3.3. Finite Element Model Setup

Once the 3D model from Revit is ready, and material properties have been decided, the CAD model is then transferred to DIANA. This process, on paper, is straightforward as DIANA can import generally used 3D geometry extensions (mainly .ifc, .step, and .iges). While exporting 3D model into intermediary extension (in this research, .step is used as it is the most consistent),

some geometry adjustments are still needed, as when the mesh is fully generated, some geometrical inconsistencies are shown.

One of the recurring issues found during initial model setup is mesh generation. Due to the complexity level of the building, generating a properly meshed model is proven to be tricky. One example of such an issue is how the contact area between elements, for example, between walls and arches, might influence how the mesh is generated. Without ensuring proper element alignment or by utilizing the imprint menu in DIANA, the meshed model might fail to generate.

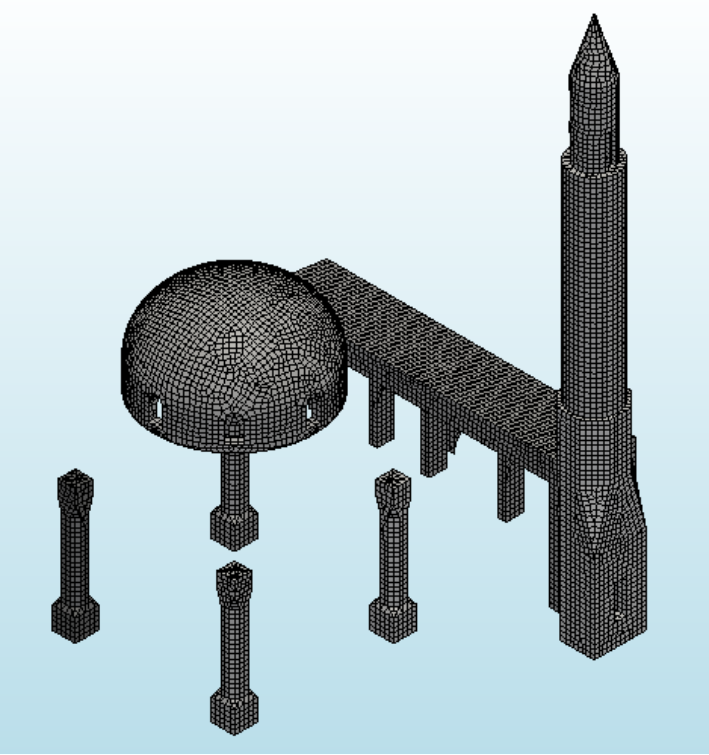

Figure 3-9 Initial mesh failure

Once the contact area and alignment between structural elements are adjusted, it was also found that using a spherical shape for interior domes also caused some issue where the geometry failed to convert into meshed elements.

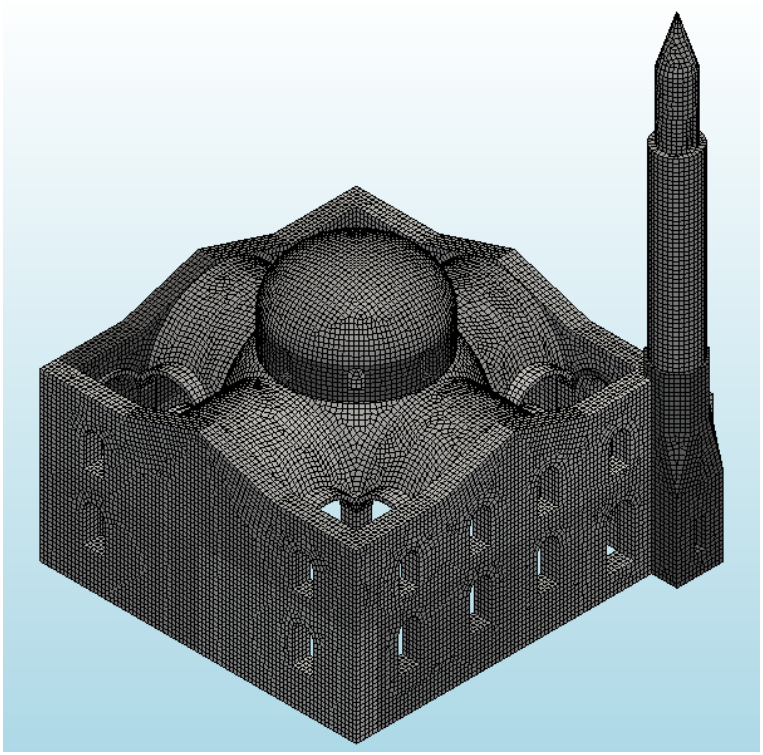

Figure 3-10 Every element except the interior domes has successfully meshed.

After changing the interior domes from elliptical to spherical, the full model meshed successfully, even without imprinting most interfaces. However, once initial runs were conducted, another geometrical inconsistency was found in this project in the form spiderweb mesh, mainly in the position where interior arches are *attached* to the walls.

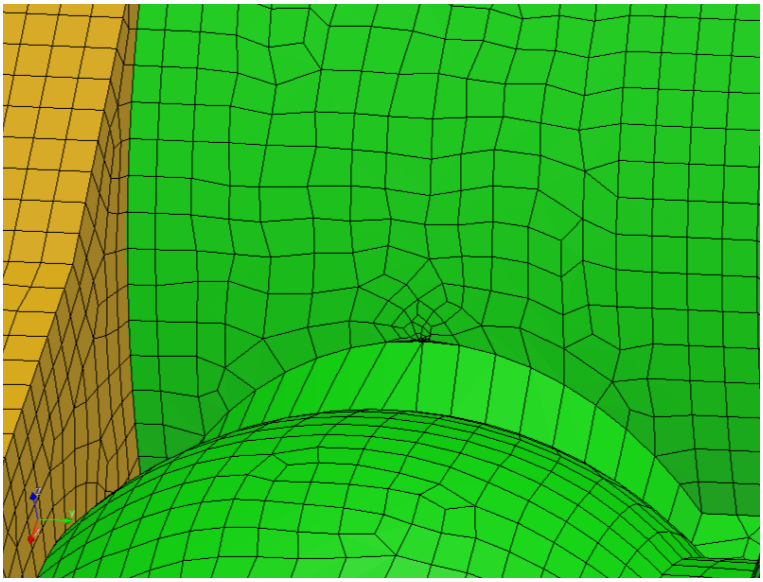

Figure 3-11 Example of spiderweb mesh between arches

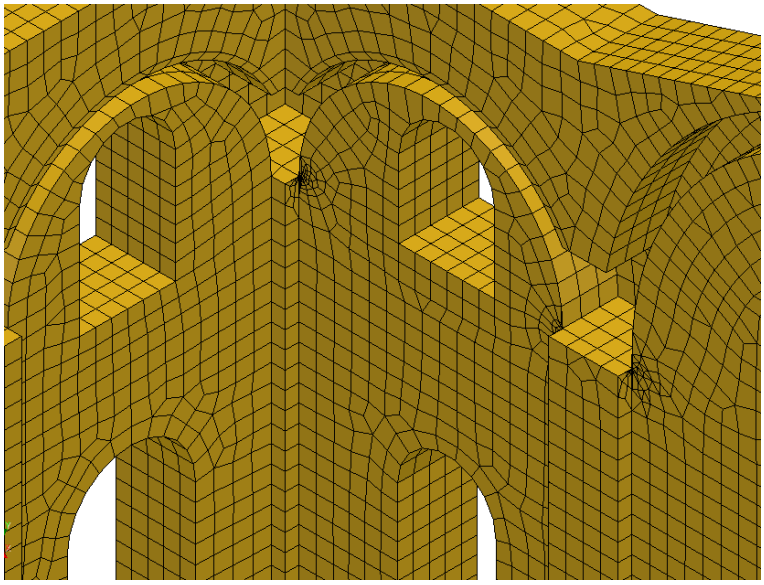

Figure 3-12 Example of spiderweb mesh on wall elements

This phenomenon is likely caused by modelling inaccuracies as Revit has limit for smaller element details where these details mattered more for numerical analysis in DIANA. Another issue found from imported model during eigenvalue analysis, one of the columns did not attach perfectly into the transition element, causing unusual mode shape and incorrect load transfer.

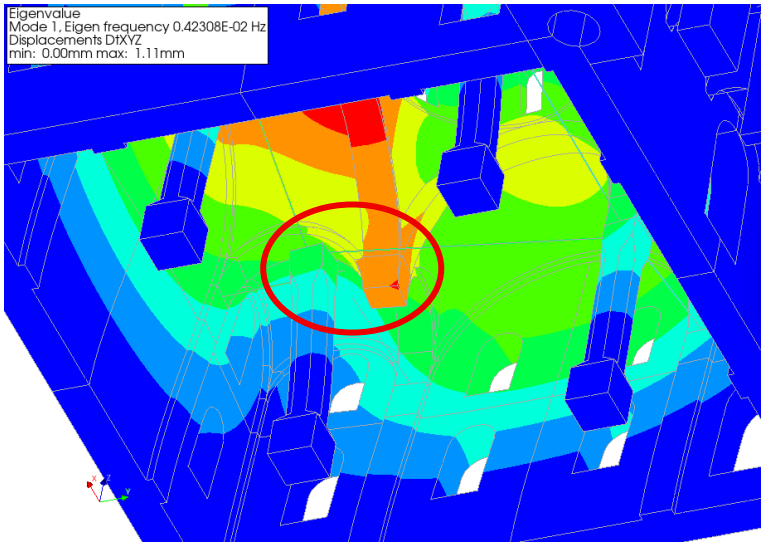

Figure 3-13 Example of column detached due to misalignment issue

To counter these issues, and ensuring that numerical model can run properly, larger elements, like exterior walls, are divided into several elements so that geometric issue can be isolated by either manual adjustment in DIANA or replacing problematic parts through mirroring.

Once imported model is cleaned up from geometric inconsistencies and errors, appropriate mesh size can be decided. Initial test shown that mesh target size larger than 450 mm failed to process on the tip of minaret section.

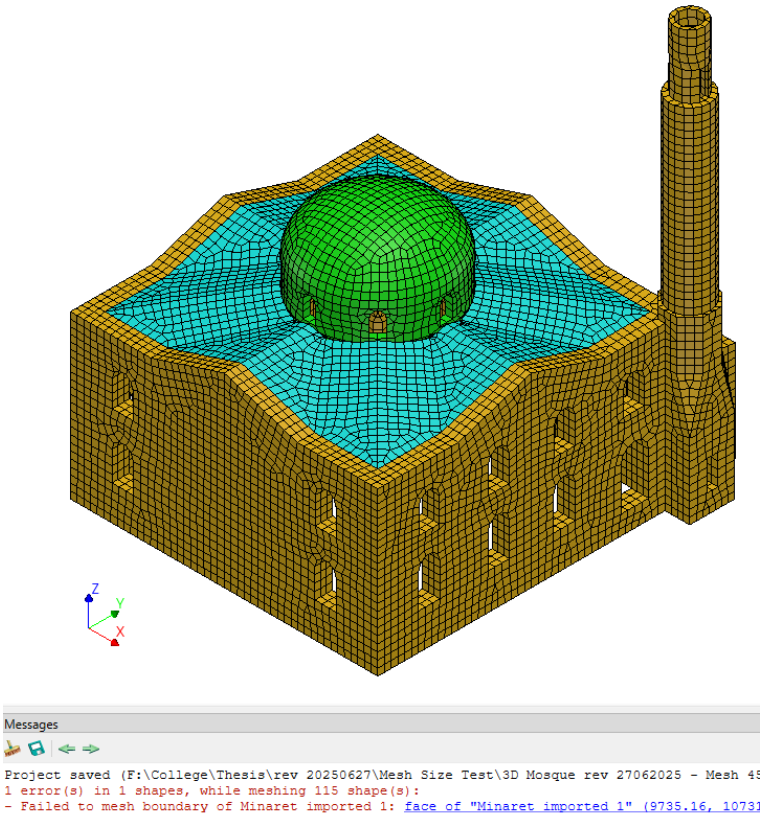

Figure 3-14 Failed meshed model at target mesh size 450 mm

Silva (2018) employs a mesh size of 150 mm for regular and mapped discretization seen on the model of Christchurch Catholic Basilica, New Zealand. However, it is also possible to employ a larger mesh, for example, of 250 mm, for large structural elements like walls and arches where finer details of material properties are not as critical but the overall response to seismic forces is a primary concern (Lourenco, 2002). For this reason, a target mesh size of 250 mm was selected as a compromise between accuracy and computational feasibility. A finer discretisation (e.g. 150 mm) would better resolve strain localisation but is computationally prohibitive for repeated nonlinear time-history analyses, while coarser meshes (>400 mm) produced instability and unrealistic local responses at curved regions such as arches and domes. The adopted size is consistent with recommendations in previous macro-modelling studies of large masonry structures (Lourenço, 2002; Silva, 2018), balancing global accuracy with practical runtime.

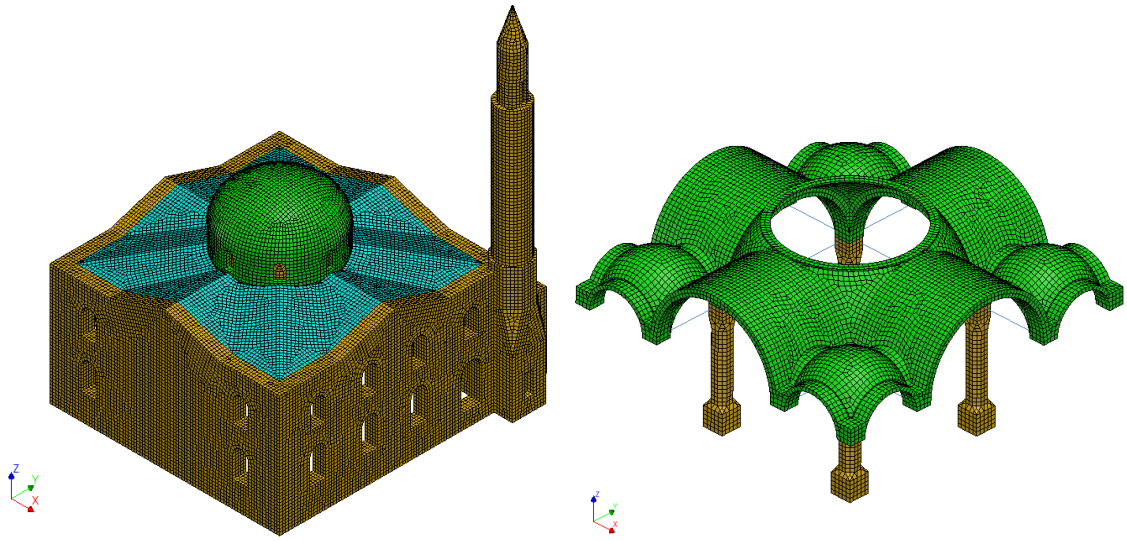

Figure 3-15 Fully meshed model

3.4. Analysis Setup

Analyses assume an isolated main body of the mosque; the minaret mass is excluded to avoid adding inertial demand not carried by the core walls. Initial assessment before interpreting any nonlinear results are: (i) gravity solution converges; (ii) base reactions match total weight within a small tolerance; (iii) first modes are global with plausible periods; (iv) cumulative horizontal mass participation is adequate by a fixed number of modes; and (v) mesh quality metrics and key responses are stable under a finer mesh. In summary, analysis scenarios for self-weight and eigenvalue analysis are evident in the table below.

Table 3-6 Analysis Scenario for Self-weight and Eigenvalues

Analysis Case	Analysis Mode	Mesh Size
Self-weight	Linear	250 mm
	Nonlinear	250 mm
Eigenvalue	Eigenvalue	250 mm
		150 mm

Unless noted otherwise, all analyses record (i) base reactions F_x,F_y,F_z, (ii) base accelerations (input vs. response), (iii) control-point displacements and normalised drifts u/H with H=11.15 m, and (iv) principal tensile strain E_1 and compression indicators for mechanism reading. Static steps use load or displacement control; dynamic runs use Δt=0.01 s. Convergence tolerances and line-search/iteration limits follow DIANA defaults unless stated; runs continue on non-convergence or when a control point exceeds 1.0% drift, while manual post-processing ignores data beyond that drift limit.

Acceptance criteria used later for checks.

- Self-weight: $|\sum R_z - W|/W \leq 1\%$, no unintended uplift, smooth vertical deformation.

- Modal: first modes global; cumulative horizontal effective mass reasonable by a fixed number of modes; small frequency shift and preserved character under mesh refinement.
- Pushover: initial stiffness compatible with first-mode period; mechanism reading from E_1 bands.
- Dynamic: input/response accelerations consistent; peaks/drifts consistent with pushover/N2 trends.
- Global axes: X east–west, Y north–south, Z vertical (Figure 3-21). "North/East/South/West wall" names follow the satellite orientation in Figure 3-21. Positive directions: X+ to east, Y+ to north.

3.4.1. Self-Weight Analysis

For this research, gravity acceleration is defined as 9.81 m/s^2 in negative Z direction (Figure 3-16).

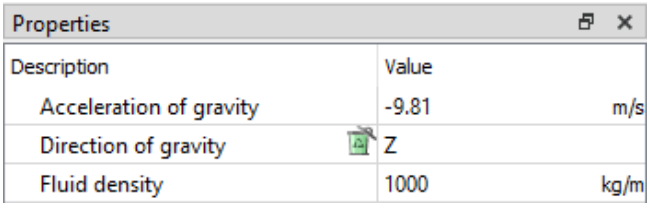

Figure 3-16 Gravity acceleration definition

This is assigned as a dead load under load case named "Self-Weight" (Figure 3-17). The model incorporates fully-resolved solid-element meshes, with material properties defined in Section 3.2 (Table 3-3 through Table 3-5) volume calculations were obtained from DIANA's analysis commands.

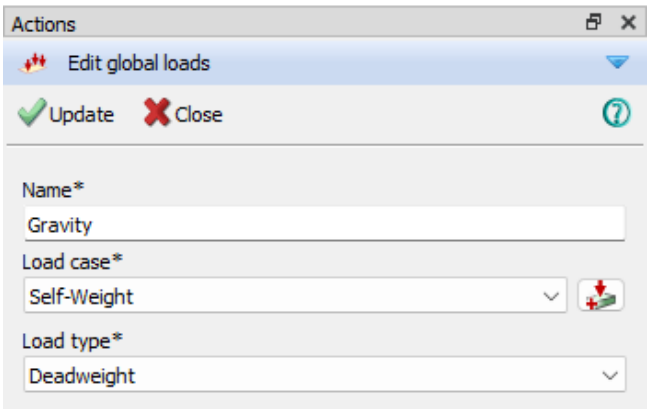

Figure 3-17 Self-weight defined as dead load

For self-weight analysis, both linear static and nonlinear analysis are conducted. This was done to observe the nonlinear effect under self-weight analysis due to both 3D model composed of structural solid elements, and due to material properties (total strain crack model) that incorporates nonlinearity as summarize in Section 3.2.

3.4.2. Eigenvalue Analysis

The eigenvalue analysis employed DIANA's Implicitly Restarted Arnoldi method paired with a parallel direct solver, with a target of 50 mode shapes from the 3D structural model. This method efficiently targets low-frequency modes critical for assessing resonance and stability. The consistent use of mesh sizes (250 mm and 150 mm, Table 3-6) enables convergence validation, literature shows that eigenfrequency estimates are sensitive to mesh resolution, and multiple mesh configurations enhance result robustness. This setup balances computational efficiency with comprehensive modal coverage.

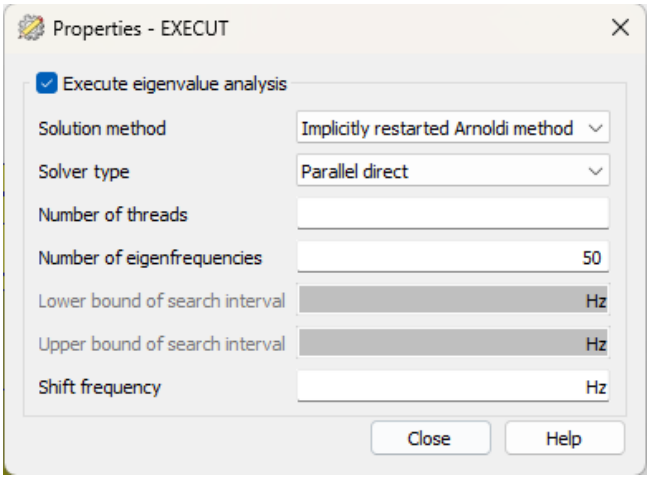

Figure 3-18 Eigenvalue Analysis Setup

3.4.3. Pushover Analysis

For this part of the analysis, the minaret will be considered as a dummy (weightless) structural component, since the focus is to find the seismic capacity of the main body of the mosque. Additionally, since it was also known that the minaret collapsed during the earthquake event, including its mass in pushover analysis would impose lateral loads not resisted by the mosque's core walls. Therefore, excluding its mass better reflects true capacity and failure mechanisms seen in the field.

A uniform horizontal body-force proportional to gravity was chosen instead of a first-mode pushover pattern because the eigenvalue analysis showed that the fundamental mode contributes less than 70% of the effective mass (Table 4-4). In such cases, a purely modal-based load may bias results towards first-mode behaviour and overlook higher-mode participation. The adopted equivalent body-force approach has been recommended in irregular heritage structures where multi-mode effects are significant (Aşıkoğlu, 2018). Its limitation is that it cannot reproduce cyclic degradation or pulse effects, which are instead addressed through complementary nonlinear dynamic analyses.

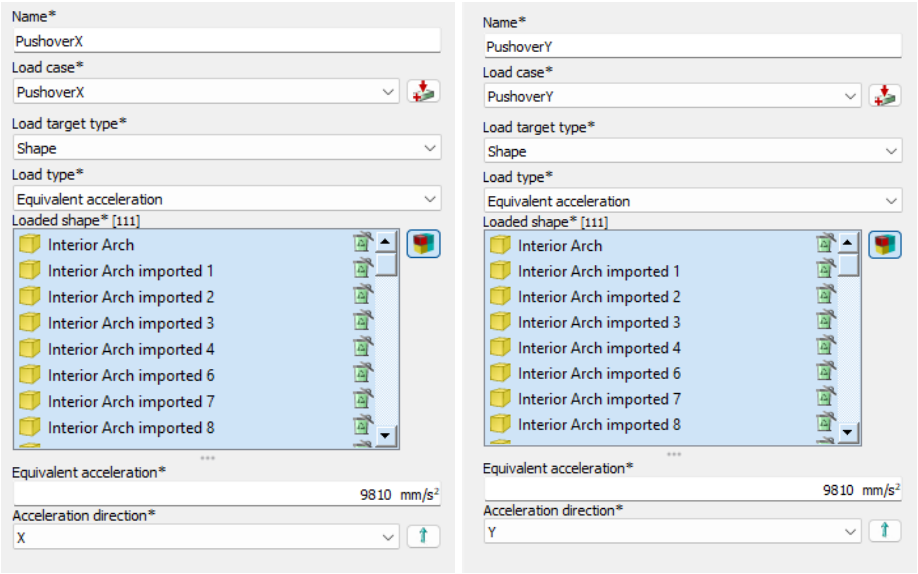

Figure 3-19 Pushover load application

These loads will be applied as an equivalent horizontal body-force proportional to the gravity load per lateral direction (Figure 3-19). The pushover loads were planned to be applied by a factor of 0.1 for as many as 80 load steps to provide a wide envelope. In practice, the analyses reach maximum loads at about 0.46 – 0.53 g.

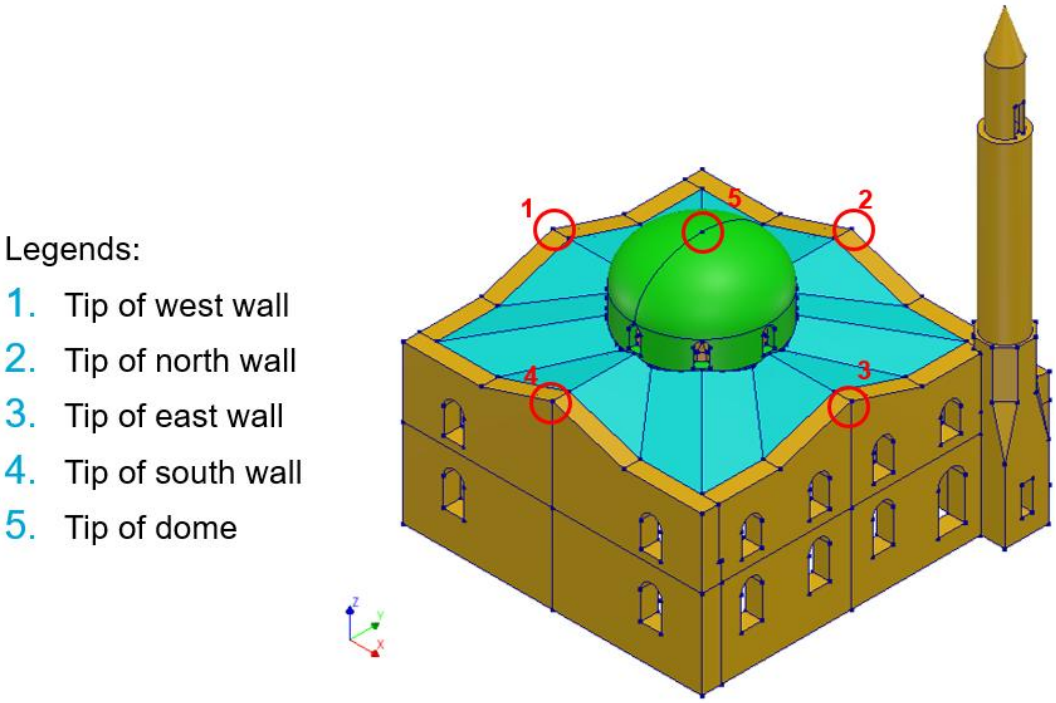

Figure 3-20 Control points definition

Control points are shown in Figure 3-20 above, where displacements are reported as absolute and as normalised drift u_i/H with H = 11.15 m. For consistency, records with drift larger than 1.0% are excluded from plots and statistics. The minaret mass is excluded so that capacities refer to the main body only; this matches the observed failure sequence and avoids assigning inertial demand to members that are not part of the resisting system.

Figure 3-21 Current satellite view of the mosque and the corresponding control points position (coordinates 37.759, 38.277)

Pushover is used to identify direction-dependent capacity, drifts, and mechanism sequence under monotonic lateral loading. Because the recorded shaking includes pulses and cyclic effects not represented by monotonic procedures, a complementary nonlinear time-history is performed to check peaks, timing, and cyclic degradation. Chapter 6 reports these results and reads them together with the pushover trends.

3.4.4. Dynamic Analysis

Pushover provides capacity and mechanism trends under monotonic lateral loading. Because observed damage involves cyclic effects and late-time pulses, a complementary nonlinear time-history analysis is used to capture rate, sequence, and cyclic degradation consistent with the recorded shaking. The two analyses are read together throughout the Chapter 6.

Two horizontal acceleration components from the nearest strong-motion station (station 0201) are used as base excitation, aligned to the model axes X (east–west) and Y (north–south). Each component from station 0201 was baseline-corrected to remove long-period drift and make velocity/displacement well-behaved under integration. Arias Intensity was computed cumulatively; only the portion of the records after Arias Intensity went higher than 2 % was used as input, to exclude low-energy pre-shaking and focus on the damaging phase. This process was done to avoid spending analysis time on micro-motion that does not influence the governing response while preserving the significant pulses seen in the station data.

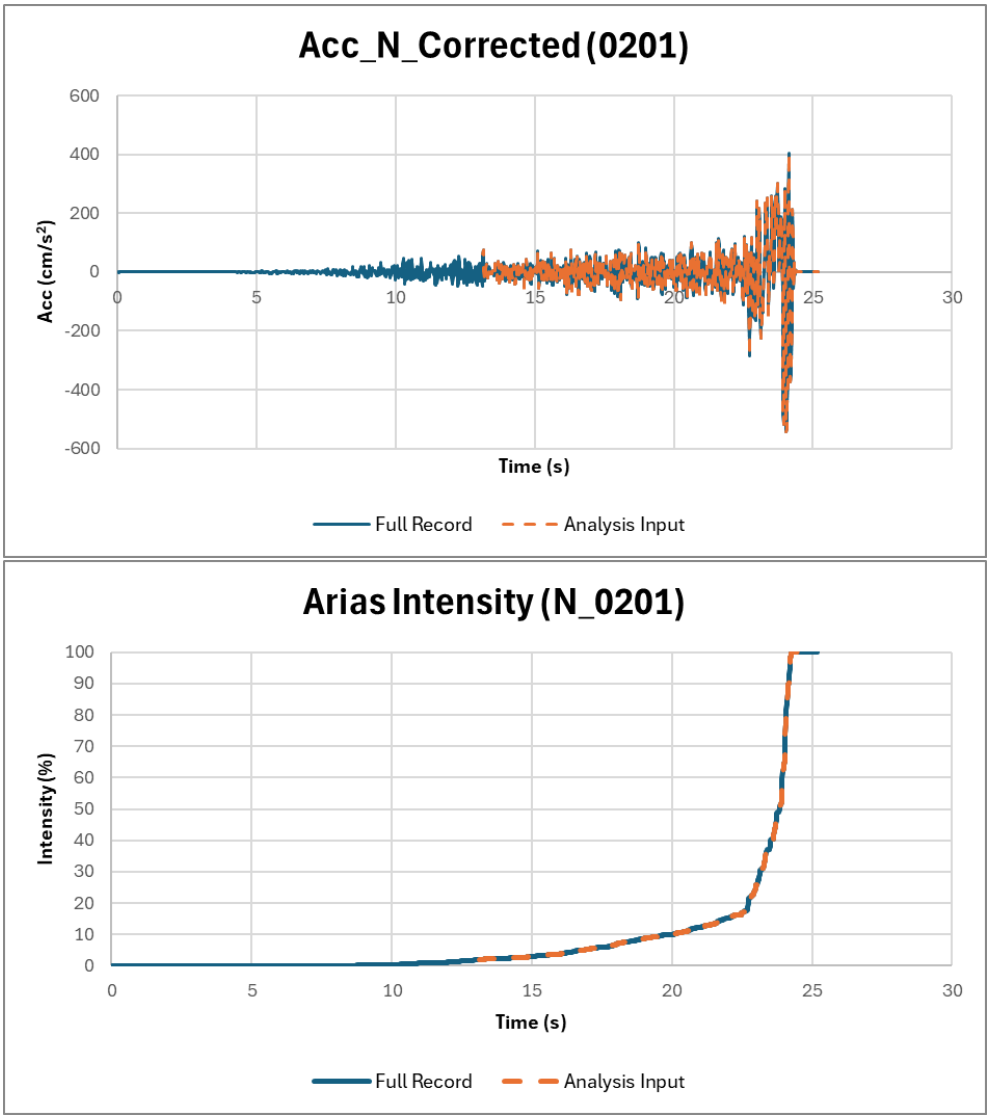

Figure 3-22 Ground motion record and Arias intensity (N direction, orange line denote analysis input)

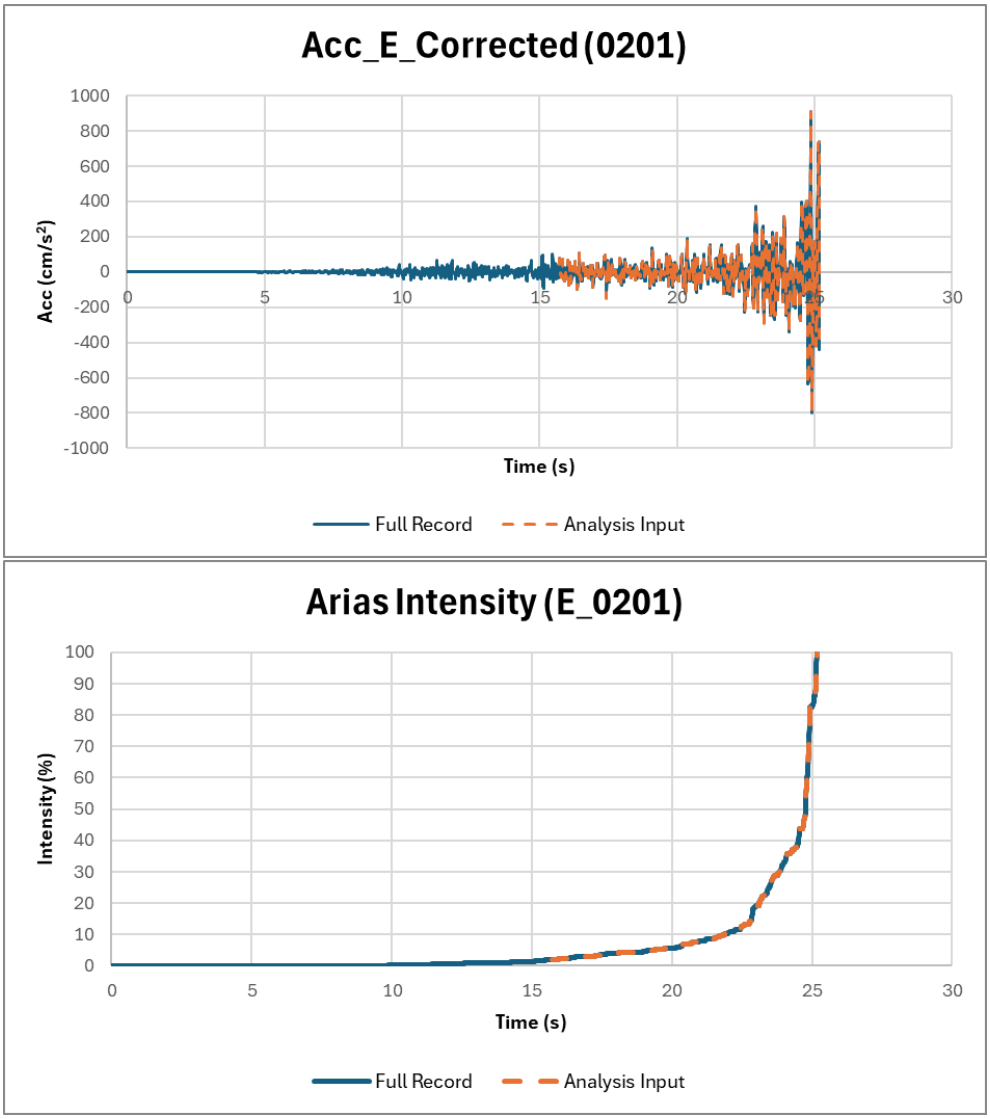

Figure 3-23 Ground motion record and Arias intensity (E direction, orange line denote analysis input)

Analyses used $\Delta t = 0.01$s (consistent with the record) and base excitations were applied as uniform translational accelerations in DIANA. Records were expressed as dimensionless g(t) and multiplied by $g_0 = 9810$ mm/s² inside DIANA to obtain the imposed base acceleration.

The FE model does not capture all energy-dissipation sources (micro-cracking before yield, friction at interfaces, diaphragm/foundation radiation, and small viscous effects). A small viscous damping ratio of about 3% is therefore introduced through Rayleigh damping as a practical proxy to control unreal high-frequency response and numerical chatter, without suppressing the nonlinear hysteretic dissipation captured by the masonry model.

The damping matrix is taken as a linear combination of mass and stiffness,

$$C = \alpha M + \beta K$$

so that the modal damping ratio varies with circular frequency ω_n as

$$\zeta_n = \frac{\alpha}{2\omega_n} + \frac{\beta\omega_n}{2}$$

To avoid over-damping long-period motion, the coefficients α,β are calibrated at two modal frequencies (ω_1, ω_2) that bracket the dominant participation band identified from the eigenvalue analysis (Appendix B, Table B-1). Using $\zeta = 3\%$ at ω_1 and ω_2 yields:

- Model w/o minaret (analysis model): $\omega 1 = 29.416$ rad/s (at 4.681 Hz) and $\omega 2 = 74.518$ rad/s (at 11.860 Hz), giving $\alpha = 1.265\ s^{-1}$ and $\beta = 5.773 \times 10{-}4$ s.
- A sensitivity check against the full model (with minaret) produces essentially the same coefficients (Appendix B).

Sensitivity of key peaks and drifts to ζ is verified in Chapter 6; results confirm that conclusions are not artefacts of the chosen values.

For dynamic analysis, several analysis cases will be employed:

- Full-time history using the intensity-trimmed records,
- A short verification window, at the last seconds of the motion record, used to cross-check peak response and efficient running time, and lastly
- Later chapters introduce an equivalent-force representation of neighbour interaction over a late-time window for comparison against the isolated-structure case.

Each analysis case will have base excitation applied to both x and y axes simultaneously, and a time step of 0.01 s.

4. Initial Analysis Results

This chapter reports the initial checks that establish the model's credibility before nonlinear lateral analysis. Two analyses are presented. First, the self-weight run confirms vertical equilibrium, load paths and support reactions. Second, the eigenvalue run identifies the main dynamic characteristics and mode shapes that will guide the reading of pushover results. The section closes with a short discussion that reflects on plausibility against the widely reported behaviour of historic masonry.

Gravity and modal analyses indicate credible behaviour. The results show plausible deformations and reactions, reasonable periods and mode shapes with adequate mass participation, and provide baselines for cross-checks in Chapter 5 pushover interpretation.

4.1. Self-Weight Analysis

Analysis result shows that summed vertical reactions match the independently estimated total weight within about 1%, no uplift occurs at supports, and the gravity-driven deformation field is smooth and physically plausible without unintended tensile cracking.

4.1.1. Global Deformations and Load Transfer

Figure 4-1 illustrates global vertical displacements under self-weight, in linear analysis mode, with maximum settlement of 5.19 mm at the tip of the dome element.

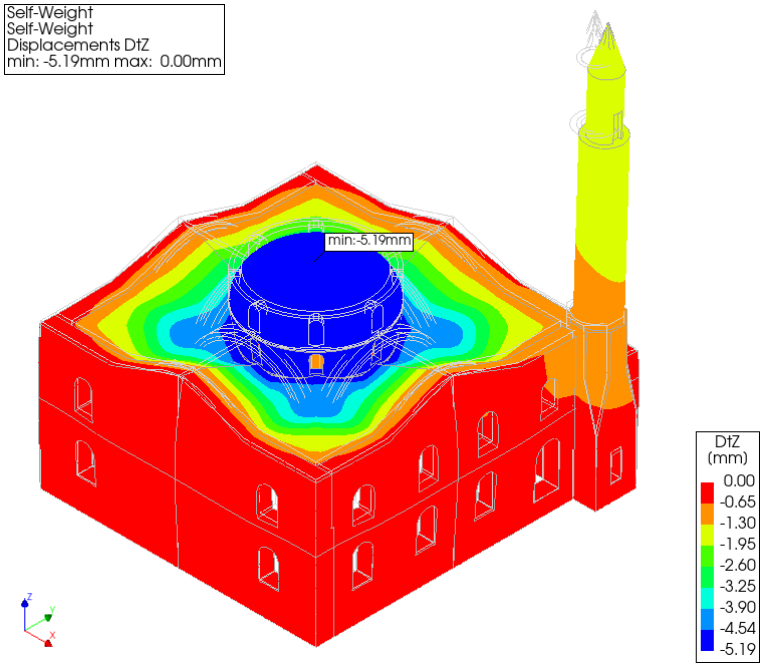

Figure 4-1 Global vertical deformation under self-weight (linear)

The effect of the domes on vertical deformation is also evident in the deformation contours in Figure 4-2 and Figure 4-3, which confirm that vertical loads flow into the interior columns through the arches. Notably, the columns exhibit out-of-plane deformation, with lateral

displacements up to 0.85 mm (Figure 4-4 and Figure 4-5). A modest lateral movement at column tips suggests possible tie or ring action influencing equilibrium. This is treated as an interpretation to be checked against mode shapes in Section 4.2 and revisited at small drift in Chapter 5, rather than a firm conclusion at this stage.

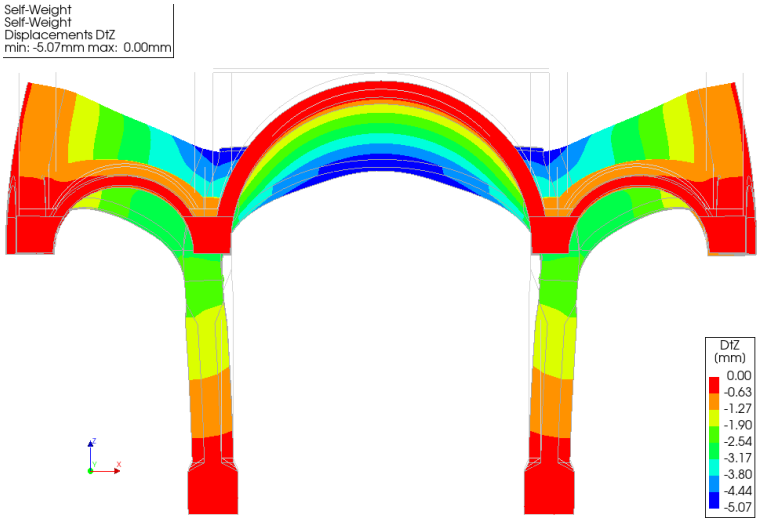

Figure 4-2 Interior vertical deformation (YZ axis, linear)

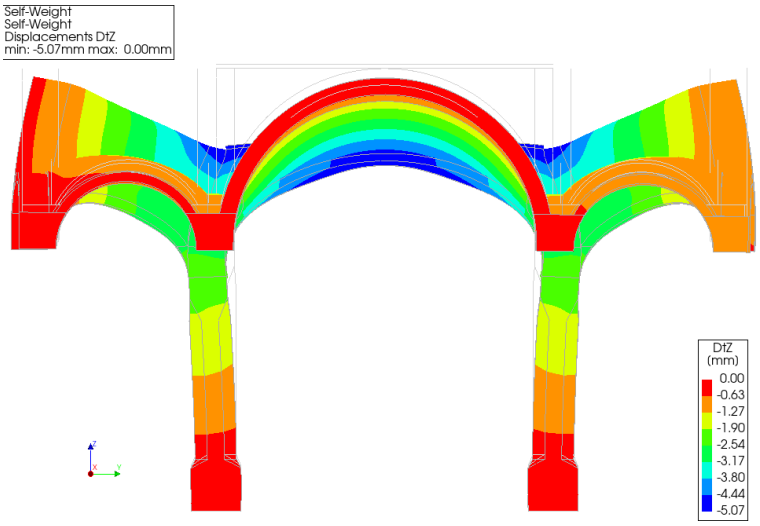

Figure 4-3 Interior vertical deformation (XZ axis, linear)

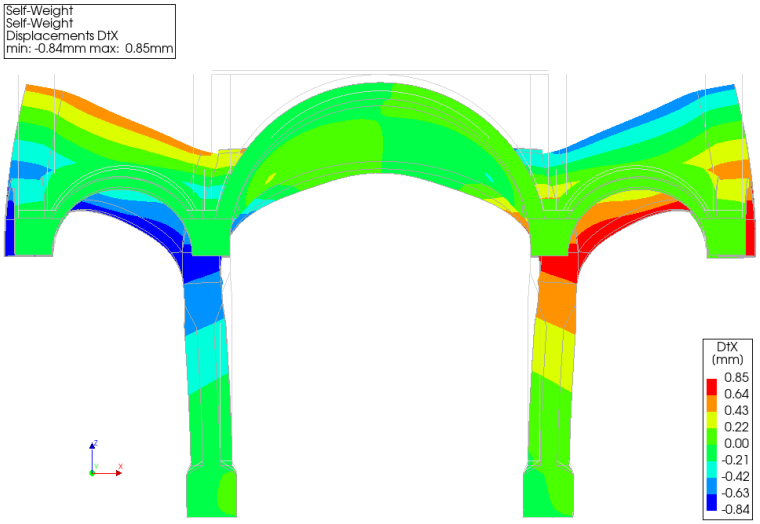

Figure 4-4 Columns tip lateral deformation in XZ axis

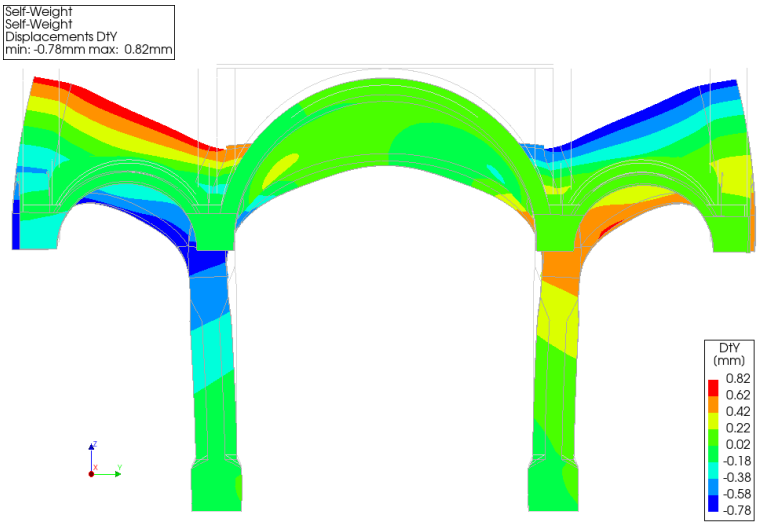

Figure 4-5 Columns tip lateral deformation in YZ axis

The observed lateral displacement suggests limited lateral restraint, such as inadequate tie ties (iron bars) between arches and pillars. In realistic masonry domes, ties or ring-beams are essential for reducing lateral thrust.

In terms of how the structural model deforms, similar results apply for the nonlinear analysis mode, which can be seen in Table 4-1 below.

Table 4-1 Summary of Deformations for Multiple Self-Weight Analysis

Analysis Output	Analysis Modes	
	Linear	**Nonlinear**
Vertical displacement (tip of dome)	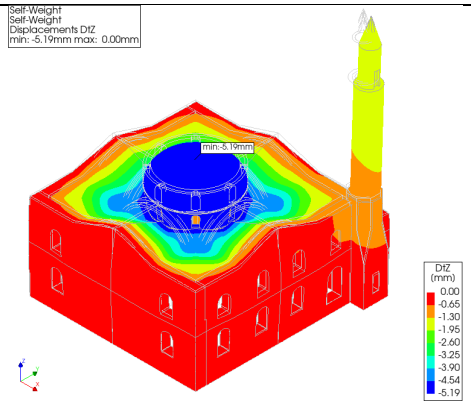 $d_{z,dome}$ = 5.19 mm	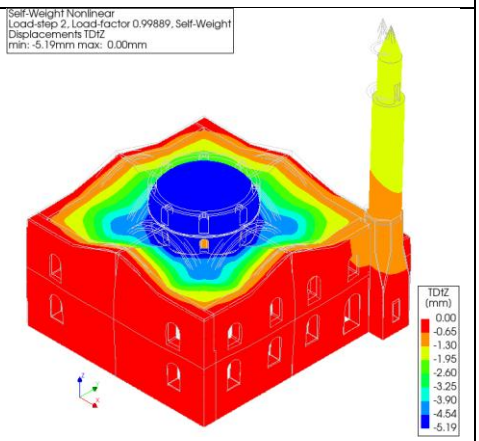 $d_{z,dome}$ = 5.19 mm
Lateral deformation (tip of columns, XZ)	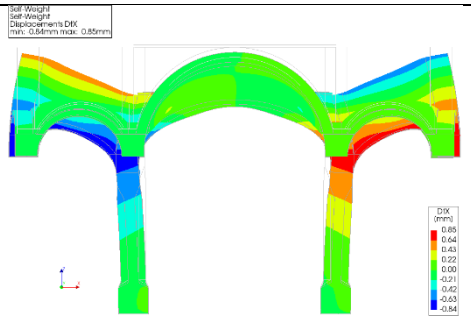 $d_{x,col}$ = 0.85 mm	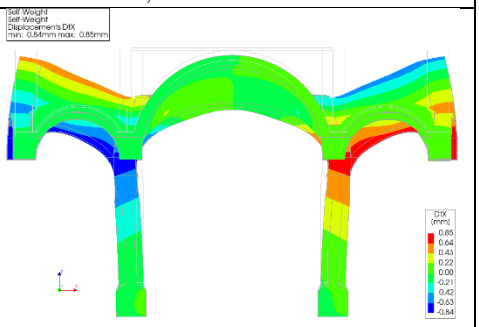 $d_{x,col}$ = 0.85 mm
Lateral deformation (tip of columns, YZ)	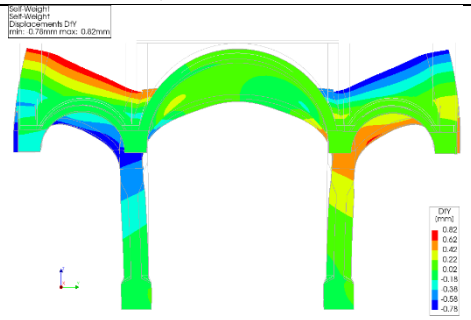 $d_{y,col}$ = 0.82 mm	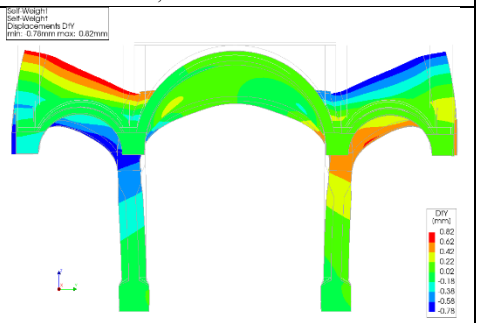 $d_{y,col}$ = 0.82 mm

4.1.2. Base Reaction

Summed vertical reactions match the independently estimated total weight within about one percent, with a reaction pattern that is consistent with gravity load paths and no uplift at supports. Figure 4-6 below shows the distribution of the vertical base reaction of the structural model. The reaction map shows gravity effects concentrated at the column bases, consistent with load transfer from domes and arches into the interior supports, confirming the load transfer mechanism of the structure discussed in Section 4.1.1 (Figure 4-1 to Figure 4-4).

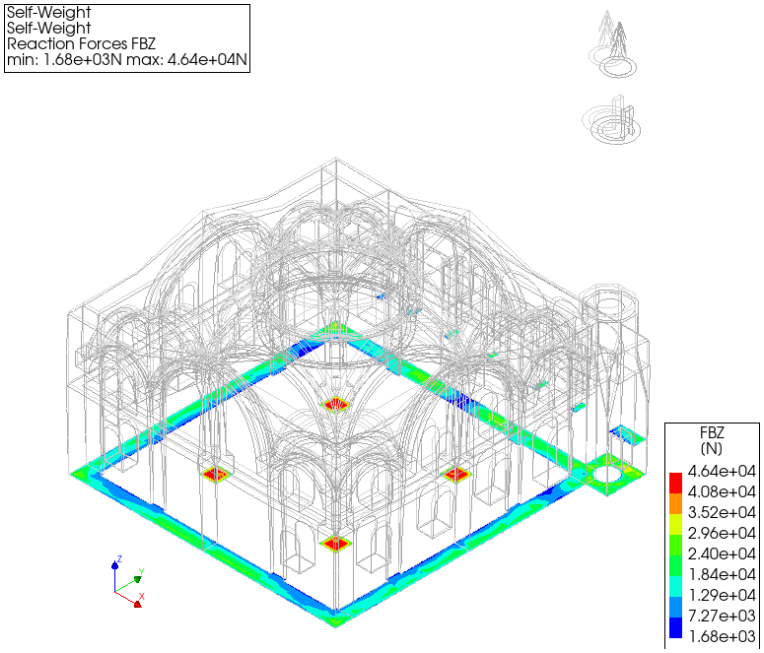

Figure 4-6 Vertical Force Reaction Contour

Summed vertical reactions give 32,907.08 kN for the linear self-weight run, against an independent weight estimate of 32,864.56 kN from the volume-density calculation (Table 4-2), a 0.13 percent difference. The nonlinear run gives 32,923.99 kN, a 0.12 percent difference from the manual estimate.

Table 4-2 Manual weight calculation

No	Elements	Vol	Mat	γ (kN/m^3)	W (kN)
1	Walls	859.13	Cut Stone	22.00	18,900.95
2	Columns	34.34	Cut Stone	22.00	755.46
3	Minaret	114.99	Cut Stone	22.00	2,529.87
4	Canopy	105.48	Cut Stone	22.00	2,320.63
5	Arches	119.10	Clay Brick	18.00	2,143.78
6	Int. Domes	27.65	Clay Brick	18.00	497.61
7	Ext. Domes	80.82	Clay Brick	18.00	1,454.81
8	Infills	239.41	Soil	17.66	4,227.43
9	Iron bars	0.48	Cast Iron	70.63	34.02
Total					**32,864.56**

With a nominal difference of around 0.13% between these two results, might be influenced by material property rounding, or meshing will naturally introduce minor differences. These minor differences between results are still within acceptable range, and it shows that the structural model behaves within expectation under self-weight loading scenarios.

Like the results of structural deformation, vertical force results are consistent across different analysis scenarios/mesh sizes, thus once again shown that the structural model can perform as expected.

Table 4-3 Summary of Base Reaction for Multiple Self-Weight Analysis

No	Analysis Mode	Base Reaction [kN]	Difference
1	Manual	32,864.56	Baseline
2	Linear	32,907.08	0.13%
3	Nonlinear	32,923.99	0.12%

The self-weight check indicates stable equilibrium and plausible load transfer. Summed base reactions equal 32,907.08 kN against an independent weight estimate of 32,864.56 kN, a 0.13 percent difference within the stated tolerance. The vertical deformation field is smooth, with maximum settlement about 5.19 mm at the dome tip, and column-tip lateral displacements remain below 1 mm, consistent with arch and dome thrust paths. Linear and nonlinear runs give essentially identical responses, indicating no gravity-induced cracking for the adopted material model. Check against Section 3.4 acceptance criteria: reaction-weight mismatch 0.13% (Table 4-2), no uplift; criterion satisfied.

4.2. Eigenvalue Analysis

Eigenvalue analysis assesses dominant mode shapes and natural frequencies of the mosque's numerical model. Fundamental modes are global and plausible, periods fall within a reasonable range for large masonry, the first modes carry substantial effective mass in each principal direction, and the results are stable under mesh refinement. These checks follow the entry criteria listed in the analysis setup.

Fifty modes were extracted using the Implicitly Restarted Arnoldi Method. Natural frequencies span about 1.79 to 16.32 Hz. The first three modes are global sway shapes of the main body. By ten modes the cumulative effective modal mass reaches 61.94 percent in X and 70.09 percent in Y, increasing to 79.79 percent and 80.05 percent respectively by fifty modes. Modes are ordered and discussed by effective mass because participation, not frequency ranking, governs influence (Table 4-4).

Table 4-4 Summary of first 10 modes based on mass participation

Mode	f (Hz)	T (s)	Cumulative Mass Participation (%)		
			X component	Y Component	Z Component
1	5.17	0.19	16.14	30.78	0.00
2	4.68	0.21	16.56	53.11	0.01
3	5.10	0.20	55.86	62.86	0.01
4	7.58	0.13	55.87	63.07	12.40
5	11.94	0.08	59.05	64.80	12.44
6	1.89	0.53	60.80	66.45	12.45
7	11.43	0.09	61.79	67.56	12.45
8	12.54	0.08	61.79	70.00	12.67
9	13.11	0.08	61.88	70.09	16.41
10	15.45	0.06	61.94	70.09	17.09
15	13.44	0.07	69.92	71.14	17.37
20	7.00	0.14	70.18	72.06	18.76
30	15.97	0.06	72.55	74.20	20.01
40	14.34	0.07	76.16	75.80	21.02
50	14.93	0.07	79.79	80.05	30.09

The mode with the largest effective mass in X or Y need not be the lowest-frequency mode. The slender minaret introduces low-frequency, localised shapes that mobilise little horizontal mass of the main body, so a slightly higher-frequency global sway mode can dominate participation (see Figure 4-7). This behaviour is consistent with reported cases for historic churches and mosques, and aligns with practice that prioritises participation factors when linking MDOF to SDOF response.

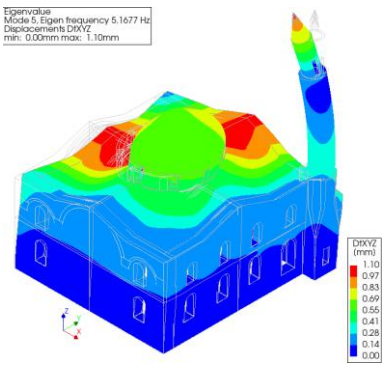

Mode 1 (5.17 Hz)

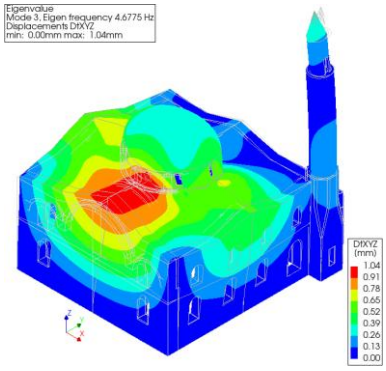

Mode 2 (4.67 Hz)

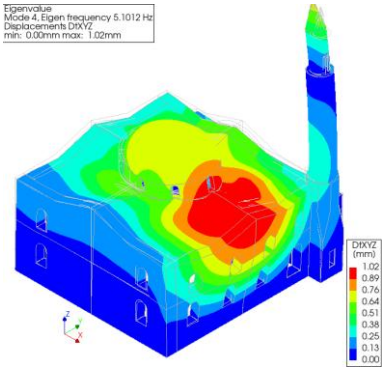

Mode 3 (5.10 Hz)

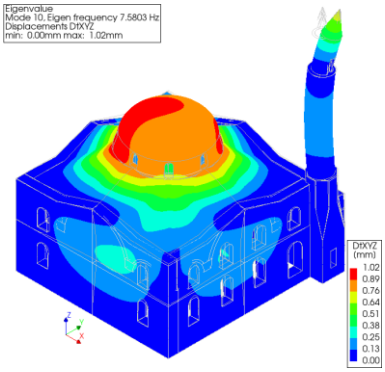

Mode 4 (7.58 Hz)

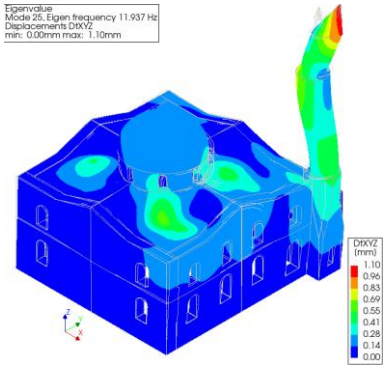

Mode 5 (11.94 Hz)

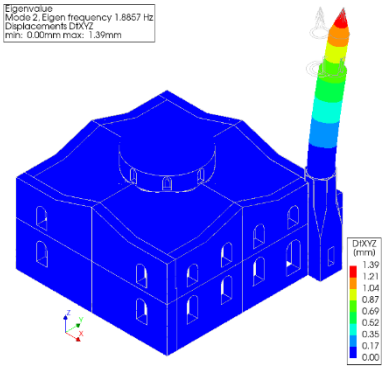

Mode 6 (1.89 Hz)

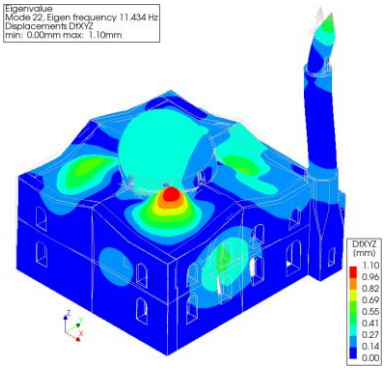

Mode 7 (11.43 Hz)

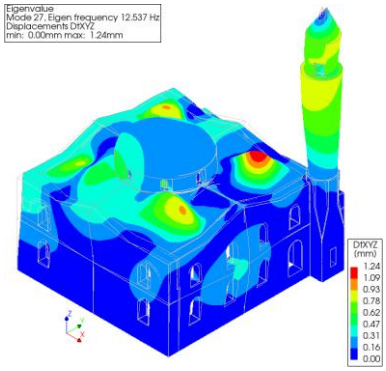

Mode 8 (12.54 Hz)

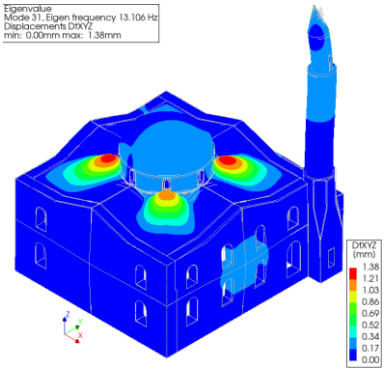

Mode 9 (13.11 Hz)

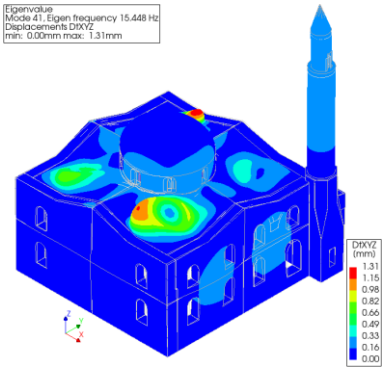

Mode 10 (15.45 Hz)

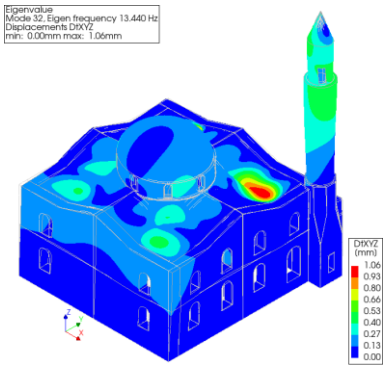

Mode 15 (13.44 Hz)

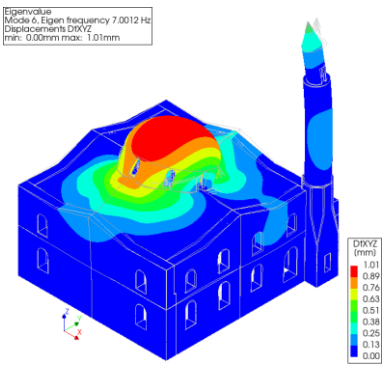

Mode 20 (7.00 Hz)

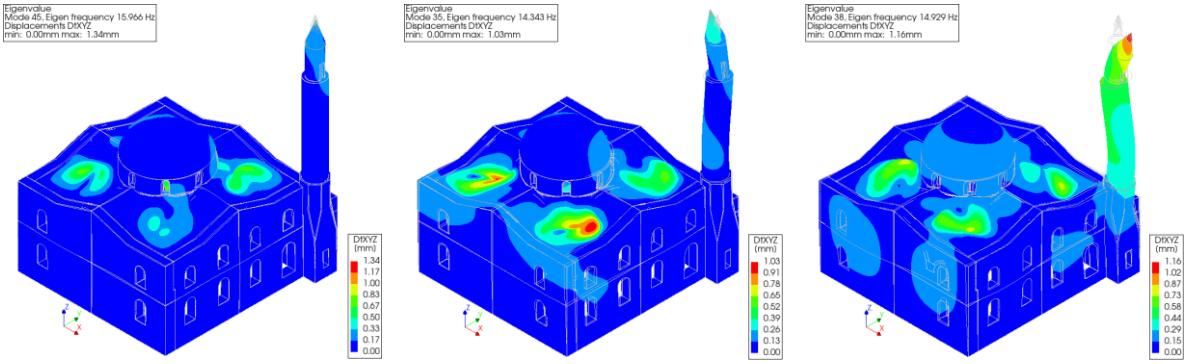

Mode 30 (15.97 Hz) Mode 40 (14.34 Hz) Mode 50 (14.93 Hz)

Figure 4-7 Mode Shape

Re-running with a 150 mm mesh leaves the first global sway modes essentially unchanged in character, with small frequency shifts of only a few percent. Ordering differences appear for higher and localised shapes, particularly those dominated by the minaret, which is expected. The cumulative mass trends remain comparable, indicating that the modal results are not unduly sensitive to the discretisation adopted.

Table 4-5 Comparison between the Eigenvalue Analysis Result

Mesh Size 250 mm					
Mode	**f (Hz)**	**T (s)**	**Cumulative Mass Participation (%)**		
			X component	**Y Component**	**Z Component**
1	5.17	0.19	16.14	30.78	0.00
2	4.68	0.21	16.56	53.11	0.01
3	5.10	0.20	55.86	62.86	0.01
4	7.58	0.13	55.87	63.07	12.40
5	11.94	0.08	59.05	64.80	12.44
Mesh Size 150 mm					
Mode	**f (Hz)**	**T (s)**	**Cumulative Mass Participation (%)**		
			X component	**Y Component**	**Z Component**
1	5.11	0.20	24.89	25.47	0.00
2	4.61	0.22	25.23	45.29	0.01
3	7.47	0.13	25.24	45.50	11.96
4	11.81	0.08	28.05	47.35	11.98
5	1.88	0.53	29.79	49.03	11.98

The modal results are plausible for a large masonry structure and satisfy the acceptance criterion. Global sway modes lead the response and carry the majority of effective mass, while local minaret or roof modes appear at various frequencies with limited participation. The small frequency changes under mesh refinement and the preserved modal character indicate stable results. These outcomes provide baselines for the Chapter 5 cross-checks, namely initial pushover stiffness versus first-mode period, early displacement shape versus the first lateral mode, the X:Y stiffness trend, and the plausibility of early cracking locations. Mesh-refinement sensitivity and preserved modal character satisfy Section 3.4 acceptance criteria for modal plausibility.

4.3. Discussion

The gravity runs show a smooth vertical deformation field, reactions that match the independent weight estimate within a tight tolerance, and no unintended uplift. This agrees with thrust-line expectations for domes and arches and with practice in macro FE studies on historic masonry, where a credible gravity state is a prerequisite for lateral interpretation (Lourenço, 2002; Betti & Vignoli, 2011; Lourenço et al., 2007; Silva et al., 2018).

The first modes are global sway shapes that carry most of the effective horizontal mass, while several low-frequency shapes are localised in the minaret and roof. The mode with the largest participation in X or Y is therefore not always the lowest-frequency mode, since slender appendages can introduce low-frequency shapes that mobilise little mass of the main body (D'Altri et al., 2020; Işık et al., 2023; Kocaman, 2024; Kiral et al., 2024). This pattern for churches and mosques is widely reported, with global sway governing participation and local tower or minaret modes appearing at a range of frequencies (Işık et al., 2023; Kocaman, 2024).

Small frequency shifts and preserved modal character under mesh refinement are consistent with recommendations to show that key outcomes are not artefacts of discretisation. Similar stability expectations and mesh-sensitivity checks appear in macro modelling guidance and case studies (D'Altri et al., 2020; Silva et al., 2018; Lourenço, 2002).

Participation, not frequency ranking, governs influence. The initial pushover stiffness and early displacement shapes will therefore be cross-checked against the first global modes and their effective masses. The mechanism-focused reading used here follows guidance for macro models of historic masonry and recognises the potential for limited diaphragm restraint (Aşıkoğlu et al., 2020; Lourenço et al., 2011; D'Altri et al., 2020).

Principal-strain plots from smeared-crack models are treated as indicators of likely cracking zones rather than literal crack maps. Interpretation is kept at the level of mechanisms and capacity trends, which is standard in building-scale assessments (D'Altri et al., 2020; Betti & Vignoli, 2011).

5. Pushover Analysis

This chapter presents the pushover analysis of the numerical model of the Adıyaman Grand Mosque to highlight and analyse failure progression and to measure the expected seismic capacity of the historic masonry structure. In brief, the capacity curves show an initial elastic branch followed by a broad post-yield plateau, consistent with tensile cracking and local compression damage that reduce tangent stiffness. Small slope changes ("ridges") mark sequential localisation: horizontal cracking above openings, diagonal bands between openings, and the development of local rotation lines along window and arch–wall zones that progressively diminish box behaviour. Occasional snap-backs arise when a concentrated band forms and resistance at the control degree of freedom drops. Strength is read from the envelope up to the plateau; the N2 bilinear idealisation is derived from this envelope and the maximum attained base reaction.

5.1. Analysis Result

Plateaus, small ridges and occasional snap-backs in the pushover curves are interpreted as described in Section 5.3. Strength is read from the envelope up to the post-yield plateau; the tail is not used for capacity. The N2 bilinear idealisation is derived from this read (Section 5.2).

5.1.1. Pushover X+

The first nonlinear pushover analysis was performed in the positive x direction (X+). Full capacity curve from the analysis shows excessive deformations from load steps 61 onwards (Figure 5-1), which, as mentioned in the previous section, will be removed.

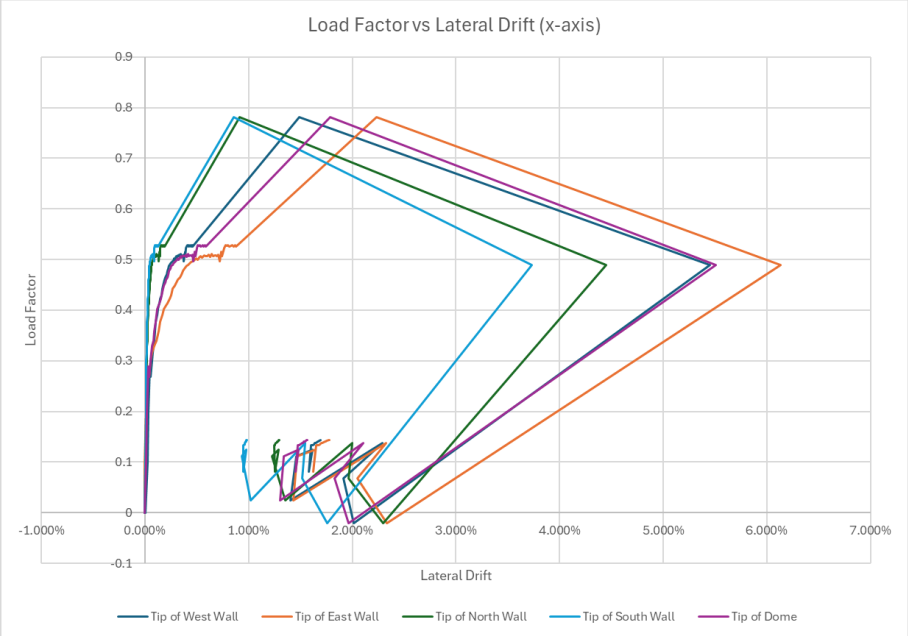

Figure 5-1 Full capacity curve of Pushover X+ analysis

After the initial elastic branch, the capacity curves flatten into a broad plateau. This reflects progressive stiffness and strength degradation as tensile cracking and local crushing spread, so the base reaction stabilises while lateral displacement continues to grow. The gentle "ridges" (small slope changes) mark sequential localisation: different wall panels and arch regions begin to engage and soften at slightly different drifts, changing the tangent stiffness. Short snap-backs can appear when a concentrated band forms and the resistance at the control DOF drops; in displacement-control, the solver continues to increase displacement while force falls, and step size/convergence tolerances can accentuate the effect.

Beyond about 1% drift, the response is governed by panel rocking and sliding, so the strength read is taken from the envelope up to the post-yield plateau rather than from the noisy tail. For interpretation (and for the N2 idealisation in Section 5.2) the curve is idealised as bilinear using an effective yield point and the maximum attained base reaction, with strain maps and control-point drifts used to verify that behaviour remains global up to the selected performance point.

Up to about 0.29 g the five control points track closely (global behaviour); beyond that they diverge, indicating limited box behaviour as panels start to act more independently. The out-of-plane wall tips attract larger drifts, while in-plane tips remain comparatively small, as evident in Figure 5-2 below.

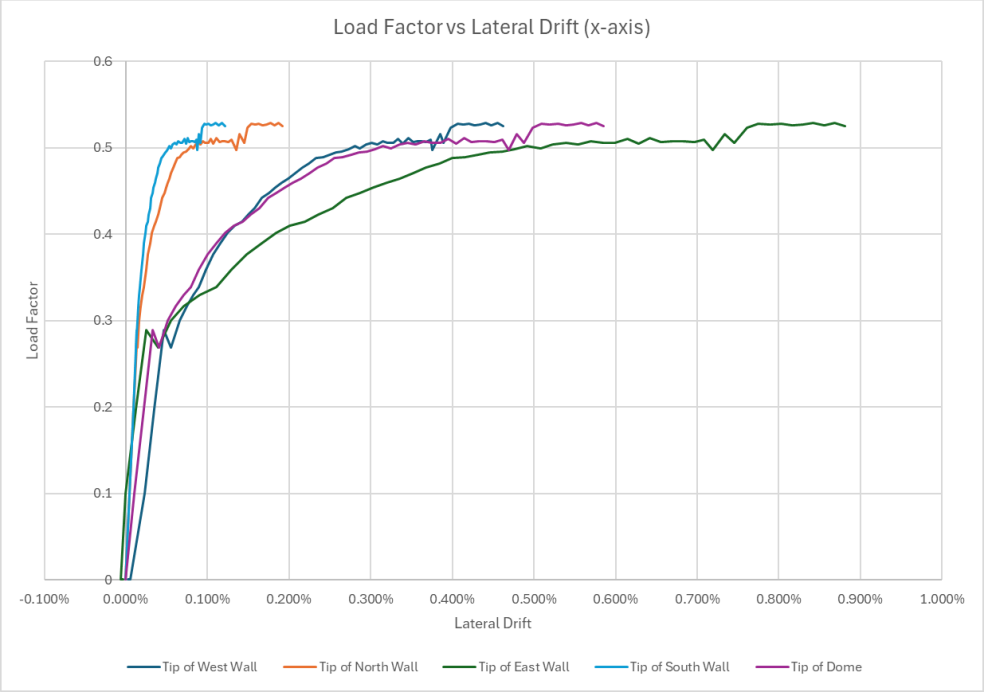

Figure 5-2 Sorted capacity curve of Pushover X+ analysis

It can also be observed that tip of North and South Walls, which are positioned in-plane with respect to load direction (Figure 5-2), exhibit smaller lateral drift relative to other control points, while Tip of East Wall, which is loaded out-of-plane, experiences the largest lateral drift. This phenomenon will be a recurring theme in pushover analysis, which is evident on the following sections.

In terms of principal strain progression, the results show that the crack progression from pushover analysis in X+ direction (at load factor 0.49g) on North Wall section seems to be in

line with the actual damage on-site (Figure 5-3), where several cracks were formed near the window opening on the wall.

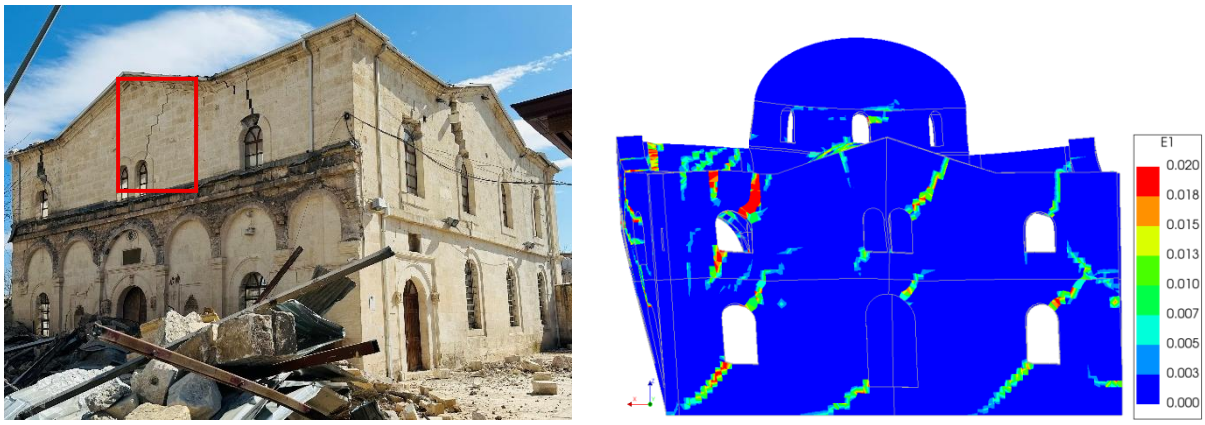

Figure 5-3 Comparison of actual (left) and numerical (right) damage on North Wall (0.49g)

This strong correlation between actual damage and simulated strain accumulation highlights the model's capability to predict and capture realistic damage progression. While the real structure exhibited full joint separation and partial collapse manifested as rubble, the numerical model indicates early-stage cracking in the same critical areas, validating both the pushover methodology and the modelling assumption.

Table 5-1 Principal Strain Progression of North Wall Section (Pushover X+)

Pushover X+, North Wall (In-Plane Loading)	
Load Step	**Principal Strain Distribution**
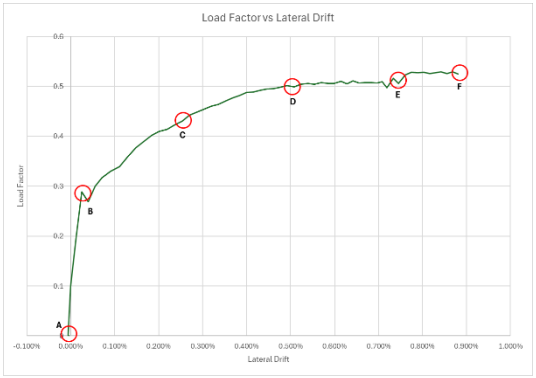 A to B, elastic limit, no visible E1 band	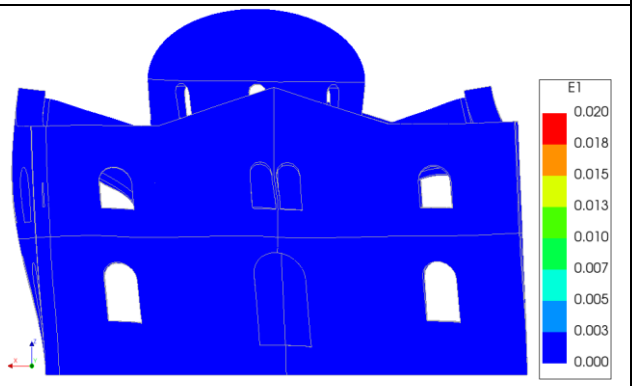 Load factor 0.29g Wall remains essentially uncracked; no shear band or flexural hinge indications.

Pushover X+, North Wall (In-Plane Loading)	
Load Step	**Principal Strain Distribution**
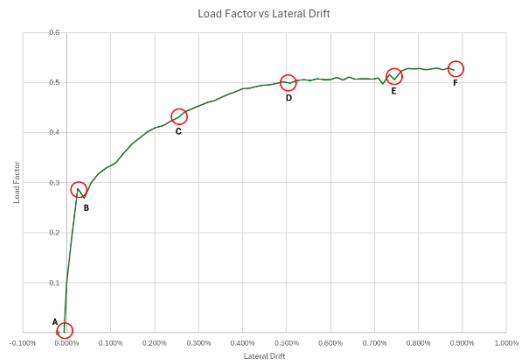 B to C, first cracking window, and arches	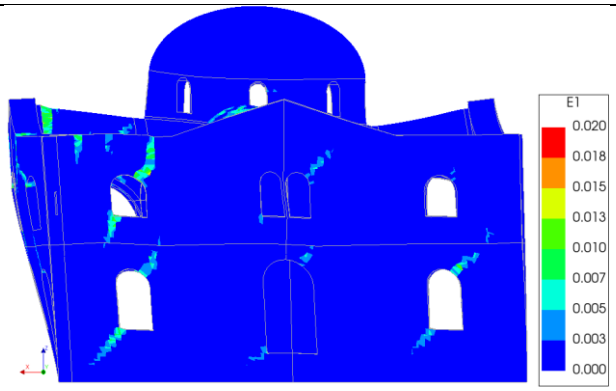 Load factor 0.38g Initial diagonal tension cracks at window openings and near the wall-roof joint; compression struts intact.
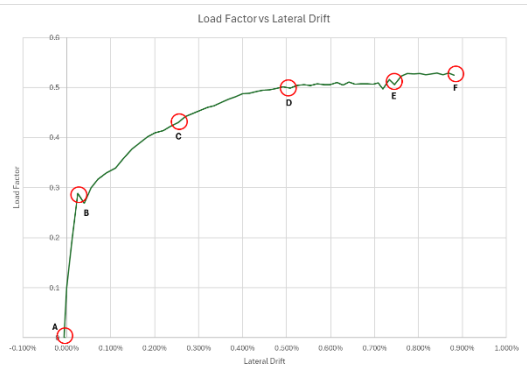 C to D, distributed diagonal tension; no continuous shear band	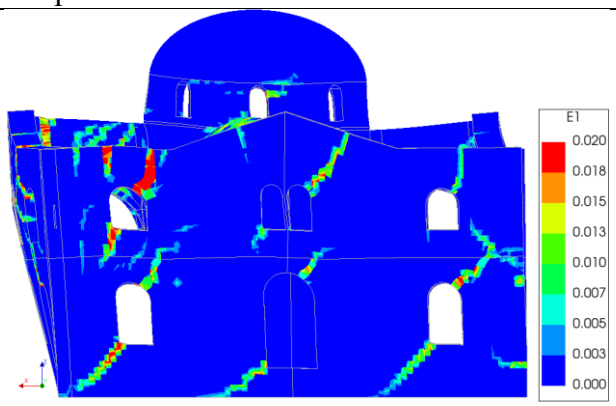 Load factor 0.49g Crack bands extend along window opening and into vertical wall strips between openings; bands are discontinuous and do not span the façade.
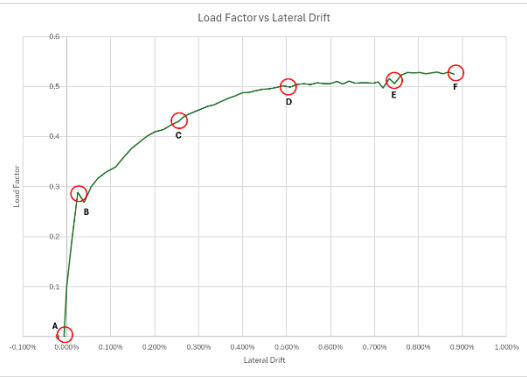 D to E, load factor intensification	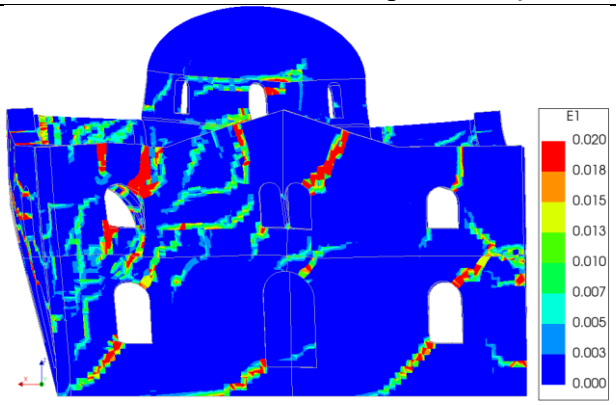 Load factor 0.51g Higher E1 strain localises around openings; no continuous shear-sliding line across the façade and no evidence of flexural response.

Pushover X+, North Wall (In-Plane Loading)	
Load Step	**Principal Strain Distribution**
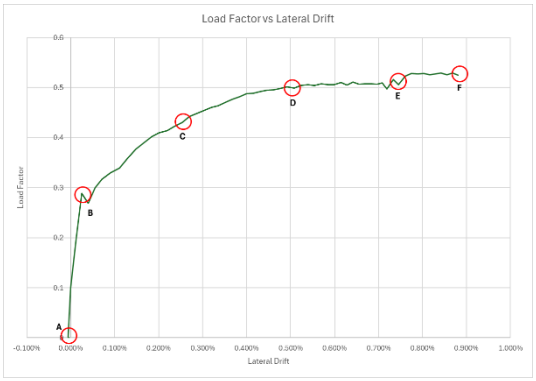 E to F, maximum load factor	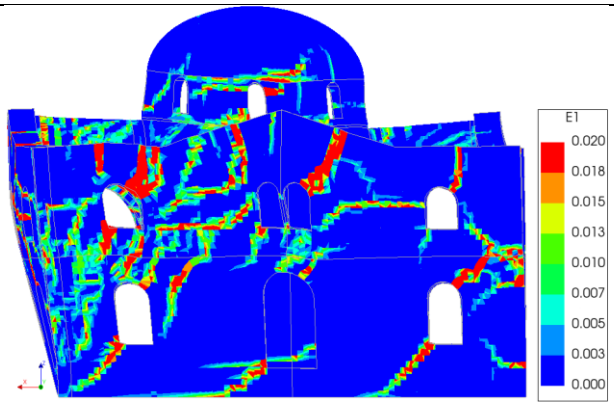 Load factor 0.52g Widespread diagonal tension around openings; window openings more active, but a through-façade shear plane still does not form. Façade retains in-plane load path, consistent with a surviving wall on site.

While North Wall section remained standing the earthquake, East Wall section, which suffers the largest lateral deformation (Figure 5-2) did not. Table 5-2 below shows the strain progression on East Wall section due to out-of-plane loading to assess whether it may contribute to the cause of the collapse.

Table 5-2 Principal Strain Progression of East Wall Section (Pushover X+)

Pushover X+, East Wall (Out-of-Plane Loading)	
Load Step	**Principal Strain Distribution**
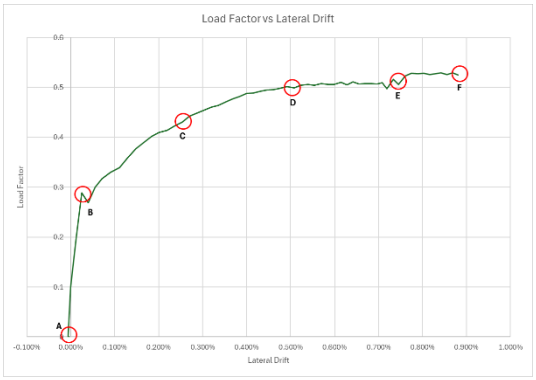 A to B, elastic limit	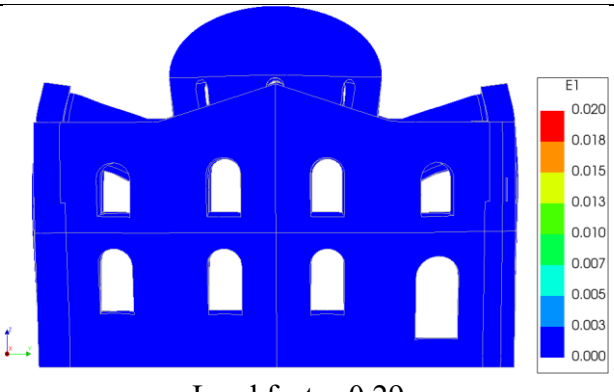 Load factor 0.29g Wall uncracked; no E1 bands visible.

Pushover X+, East Wall (Out-of-Plane Loading)	
Load Step	**Principal Strain Distribution**
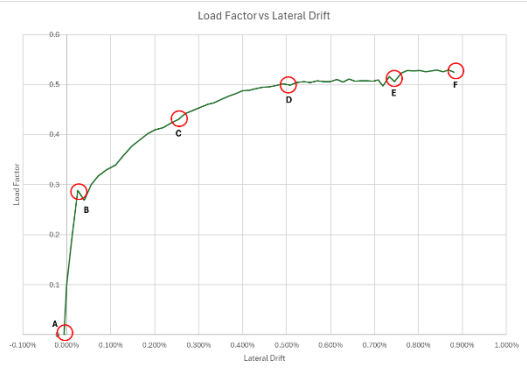 B to C, first cracking around opening and interior arches	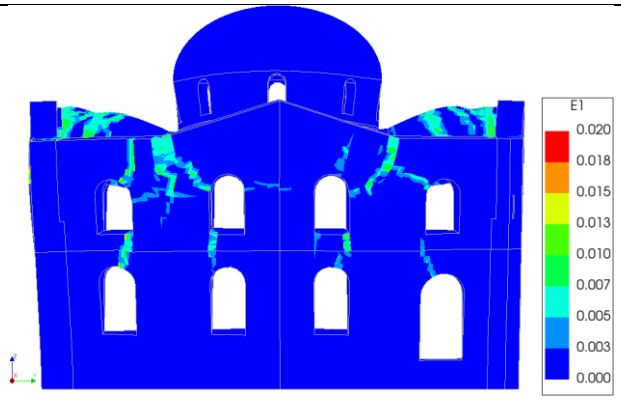 Load factor 0.38g Short diagonal E1 bands appear around window openings and interior arches. Pattern is local and discontinuous.
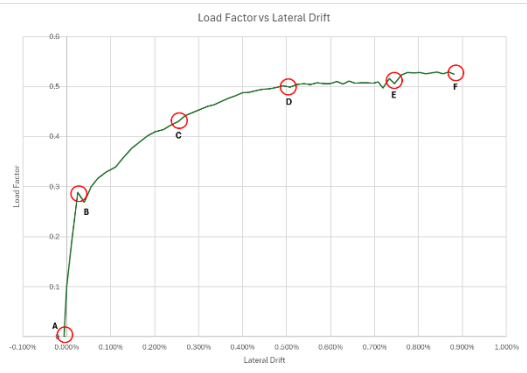 C to D, strain band extend	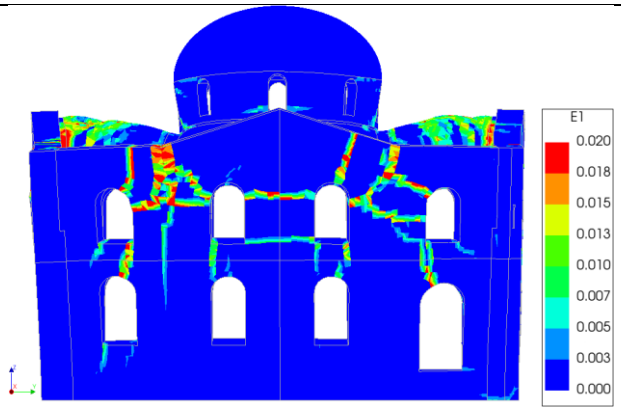 Load factor 0.49g E1 bands extend along window openings and become more distinct across higher elevation level; a vertical strip of E1 also developed along the wall. The combination of horizontal bands with a vertical edge band is consistent with the onset of an out-of-plane flexural rotation mechanism.
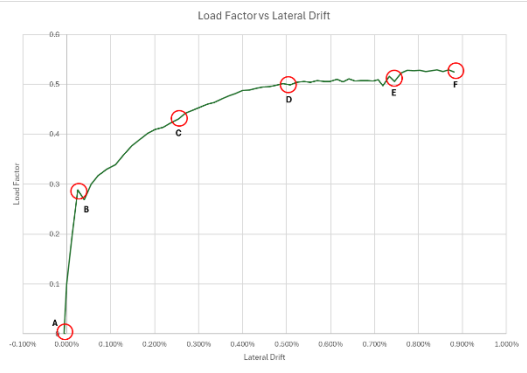	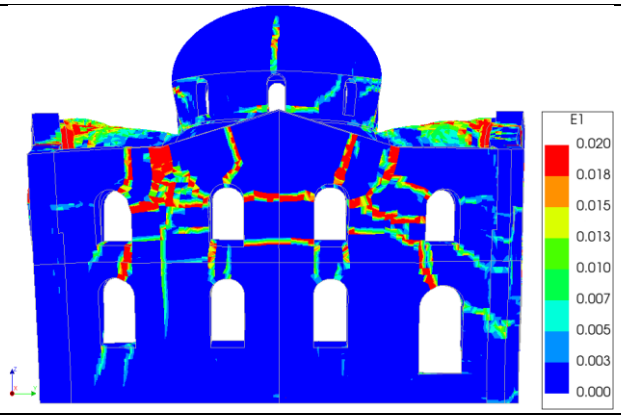

Pushover X+, East Wall (Out-of-Plane Loading)	
Load Step	**Principal Strain Distribution**
D to E, Hinge lines approaching continuity	Load factor 0.51g Horizontal E1 bands along the window opening bands connect bay-to-bay; the right vertical edge shows near-continuous E1, and diagonal bands rise towards the gable. The wall now has multiple out-of-plane hinges mechanism in the upper panels.
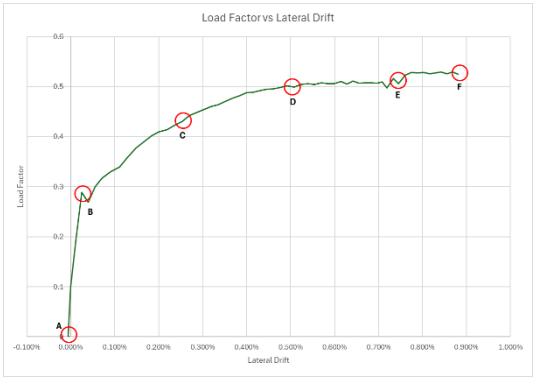 E to F, approaching maximum load	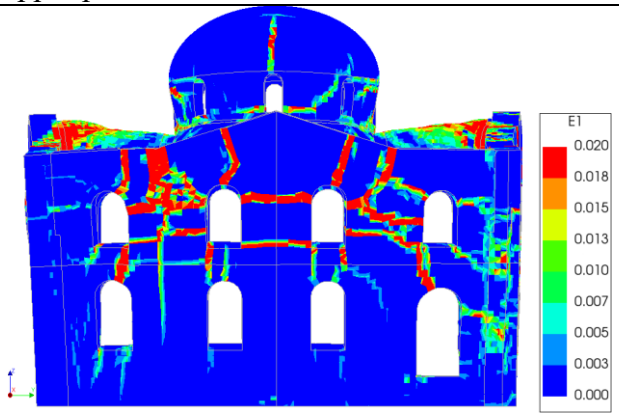 Load factor 0.52g Several horizontal cracking lines become continuous; pronounced vertical cracking appears beside the openings and along the right free edge, with additional strain concentration near the base. The pattern indicates a general out-of-plane flexural response across the upper part of the wall, especially near the interface with the minaret.

From the strain progression above, the East wall develops a pattern characteristic of a local out-of-plane flexural response. After the elastic stage, short diagonal cracks emerge at window corners and at the roof arch connections. These quickly link along the level of the window tops and, critically, are accompanied by a pronounced vertical crack at the right-hand opening side and free edge.

As loading progresses the horizontal cracking near opening levels become largely continuous across adjacent bays while the right edge band intensifies, indicating formation of the four-hinge lines that permit panel rotation out of the wall plane. The asymmetry at the right edge (adjacent to the minaret) suggests torsional amplification or reduced restraint, concentrating curvature and rotation there.

The early activity along the arch-roof line points to limited diaphragm/box behaviour, allowing the upper panels to act more independently. The aligned openings provide long bands which, once cracked, offer ready hinge paths and lower out-of-plane stability. Prior in-plane cracking

around openings (observed in other directions) would further diminish out-of-plane stiffness and hasten hinge formation.

Finally, the localised strain at the base in the last frame is consistent with gravity P-Δ effects helping to sustain rotations once hinges have formed. Taken together, the sequence highlights several contributory factors, namely out-of-plane flexural rotation of the upper panels, edge asymmetry, limited diaphragm restraint and opening-driven hinge continuity that may have predisposed the East wall to failure under X+ loading.

5.1.2. Pushover Y+

For the second pushover analysis, equivalent acceleration was applied in positive y direction. Similar to previous X+ analysis, original output data was cleaned for data points with lateral drift higher than 1.00% to obtain capacity curve.

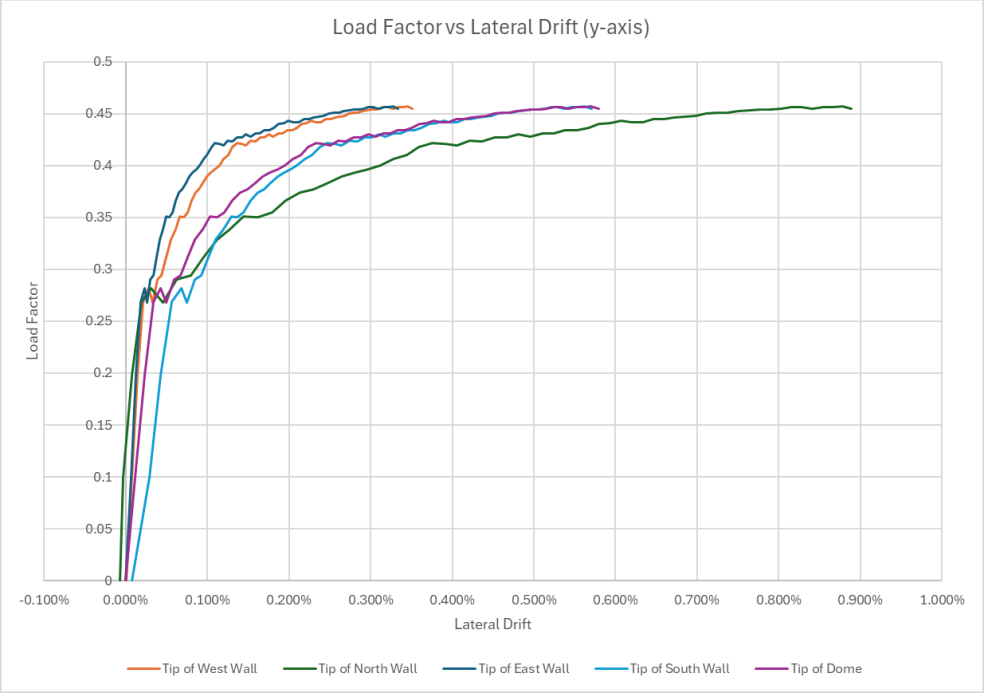

Figure 5-4 Sorted capacity curve of Pushover Y+ analysis

From capacity curve in Figure 5-4 above, the results show that while each control point exhibit consistent behaviour up until elastic limit of around 0.282g, each control point behave individually beyond that point. This phenomenon, combined with different ductility level beyond elastic limit, might indicate the absence of box behaviour. Meaning that once the structure goes beyond its elastic limit, each walls deforms independently up until maximum load of 0.457g.

The major difference between Pushover X+ and Y+ is evident on which control points drift further. Previously, Tip of East Wall experiences the furthest lateral drift due to out-of-plane loading (Figure 5-2), while for the current same (along with Tip of West Wall) exhibit smaller drift compared to control points that are loaded out-of-plane (Tip of North and South Walls).

While North Wall section remained standing the earthquake, pushover analysis on positive y direction indicates that the wall section suffers a large lateral deflection, as seen in Figure 5-2 above. Table 5-3 below shows the strain progression on North Wall section due to out-of-plane loading to assess whether it may contribute to the damage as seen in Figure 5-3.

Table 5-3 Principal Strain Progression of North Wall Section (Pushover Y+)

Pushover Y+, North Wall (Out-of-Plane Loading)	
Load Step	**Principal Strain Distribution**
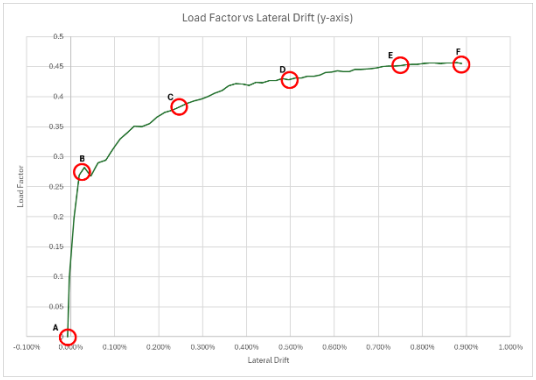 A to B, elastic limit.	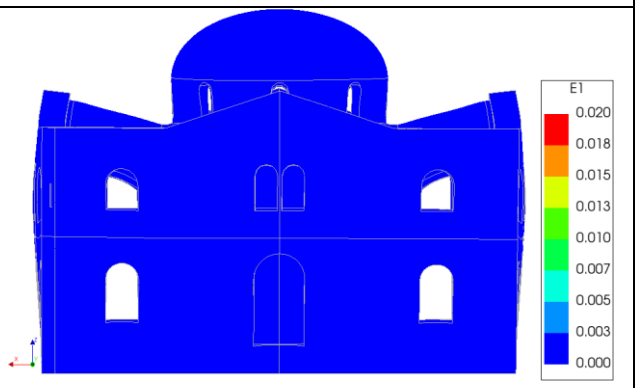 Load factor 0.27g Wall largely uncracked.
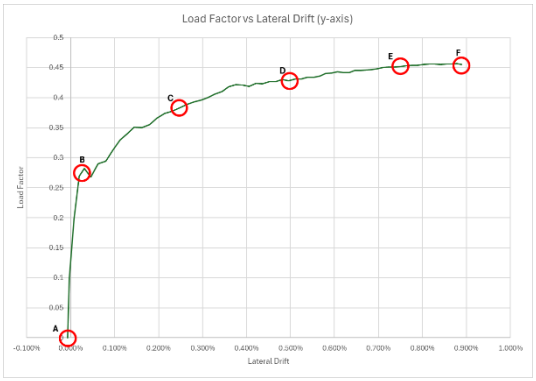 B to C, first cracking window, and arches	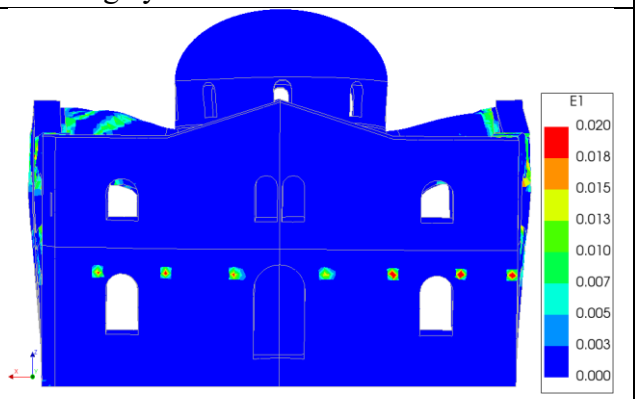 Load factor 0.34g Discrete E1 strains develop at the crowns and upper corners of the window/arch openings, and light bands appear along the gable seats. These mark the initiation of cracking near window openings that often precedes an out-of-plane panel mechanism.

Pushover Y+, North Wall (Out-of-Plane Loading)	
Load Step	**Principal Strain Distribution**
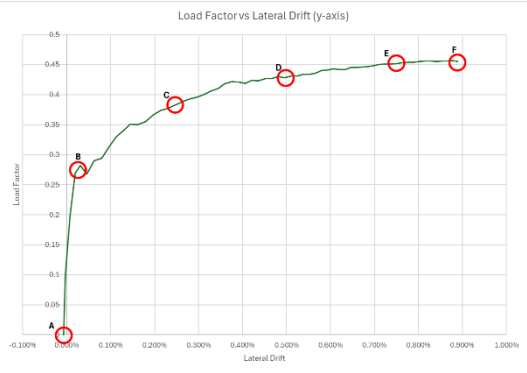 C to D, E1 band formation	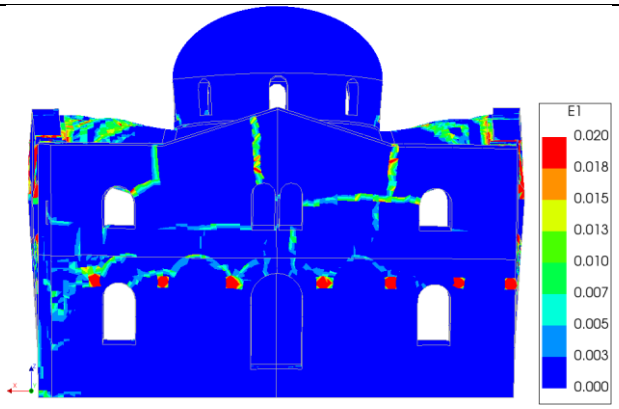 Load factor 0.42g Short E1 bands forming above wall openings and start to link between window bays; vertical strips emerge near the wall ends and under the central gable. The pattern indicates increasing curvature across the wall height and partial loss of box behaviour.
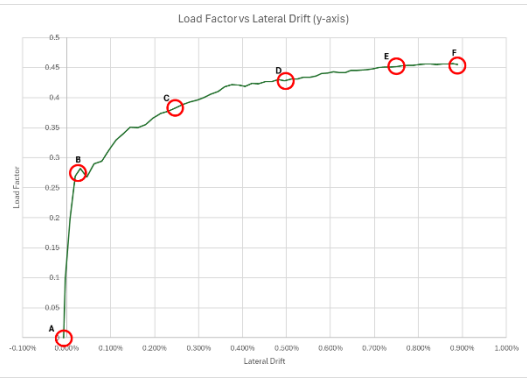 D to E, hinge lines organizing	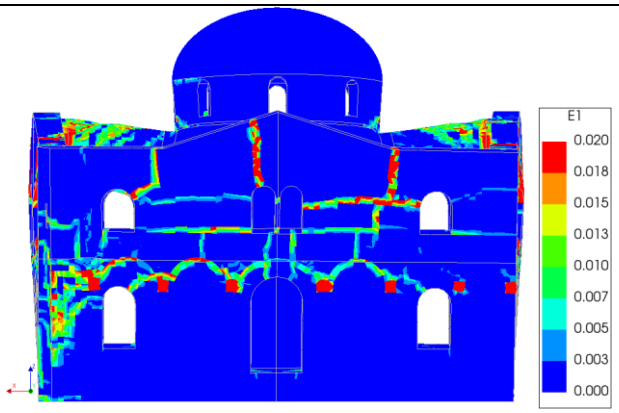 Load factor 0.44g Horizontal bands at both storeys strengthen and extend, with persistent vertical E1 at the gable web and near the left wall edge. This combination points to developing four-hinge action of the upper façade panel with local rotations about the opening levels.

Pushover Y+, North Wall (Out-of-Plane Loading)	
Load Step	**Principal Strain Distribution**
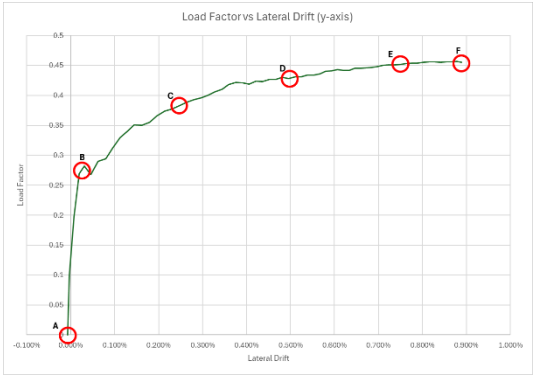 E to F, maximum load factor	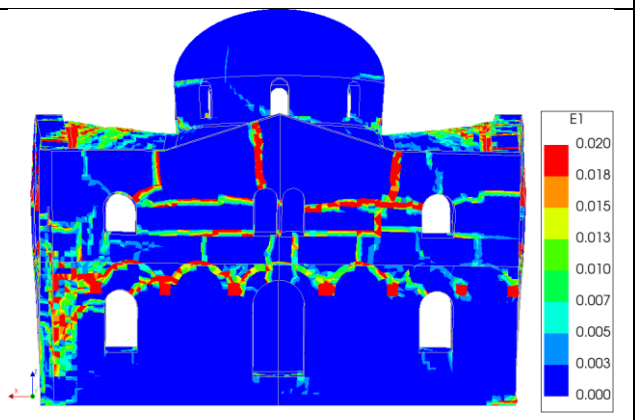 Load factor 0.45g Horizontal cracking along opening levels become largely continuous across the elevation and intensify around opening crowns; vertical strips at the ends and beneath the gable remain active. The wall exhibits out-of-plane flexural mechanism governed by hinge continuity above wall openings and concentrated rotations near the supports/edges.

The sequence shows out-of-plane flexural response of the North Wall under pushover Y+ loading. Crack initiation at opening crowns evolves into continuous horizontal bands above the wall openings, while vertical bands at the wall ends and beneath the central gable provide the complementary hinge lines.

Early activity at the arches-roof seats suggests limited diaphragm restraint, allowing the upper panels to rotate more freely, thus leading to higher lateral deflection. The alignment of openings facilitates the horizontal cracking paths, and the persistent edge bands imply stress concentration and possible torsional amplification at the supports. Taken together, these features are consistent with a developing four-hinge out-of-plane mechanism that can drive significant damage in the upper façade panels under sustained lateral demand.

Up to 0.28–0.29 g the five control points follow a common envelope, indicating global behaviour. Beyond that level the north wall (out-of-plane in Y+) draws the larger drifts, whereas the east/west tips (in-plane) stay lower. Two horizontal bands emerge, near the roof line and at upper window level, connected by vertical splitting at opening sides and local diagonals. The gentle ridges on the plateau again indicate sequential engagement/softening of wall regions. Reads for strength are taken from the envelope; the noisy tail is not used.

5.1.3. Pushover X-

From capacity curve in Figure 5-5 below, it is evident that for pushover in negative x direction, each control point display the opposite of result seen in positive x direction (Figure 5-2) in terms of how they behave. In terms of loading limit, loading in negative x direction shows elastic limit at 0.289g (same with positive x direction), with slightly smaller maximum load at 0.516g in comparison to pushover in positive x direction.

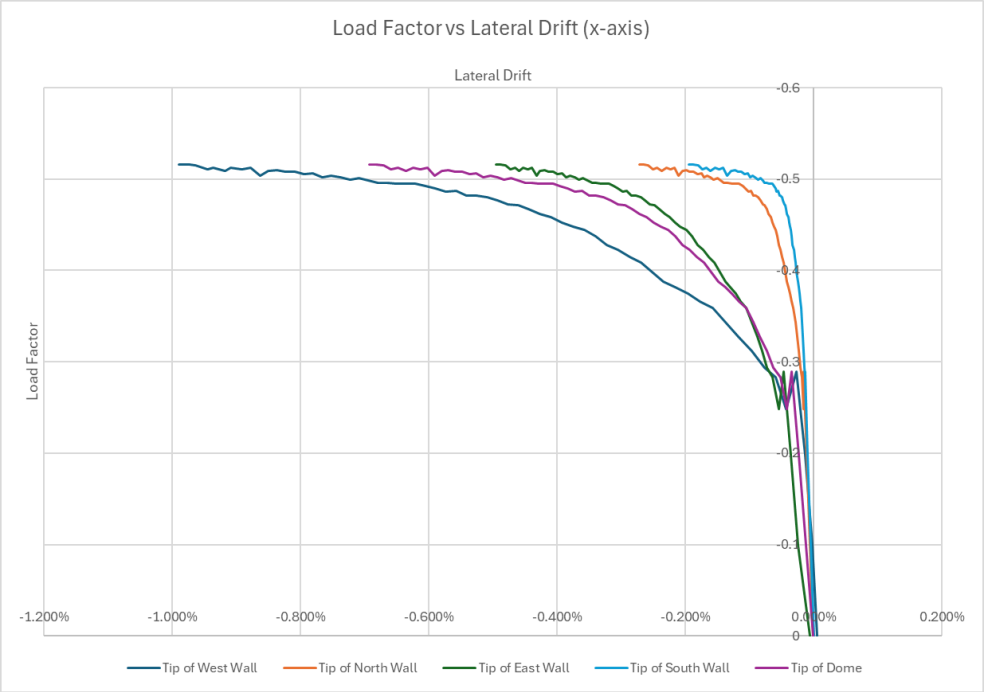

Figure 5-5 Sorted capacity curve of Pushover X- analysis

In terms of behaviour as load progresses, it is evident that up to the elastic limit, each control point shows consistent behaviour, followed by individual ductility behaviour past elastic limit. Once again showing lack of box behaviour once elastic limit is reached. In addition, Tip of East Wall displays smaller drift compared to West Wall (loaded out-of-plane), while Tip of North and South Walls shows even smaller drift. This result is consistent with pushover case shown in previous two scenarios where walls that are loaded in-plane (in this case North and South) showing smaller lateral drift, while control points where their respective walls were loaded out-of-plane (West and East) show larger drift, and especially for node directly coincides with loading direction (West, negative x direction).

Table 5-4 Principal Strain Progression of West Wall Section (Pushover X-)

Pushover X-, West Wall (Out-of-Plane Loading)	
Load Step	**Principal Strain Distribution**
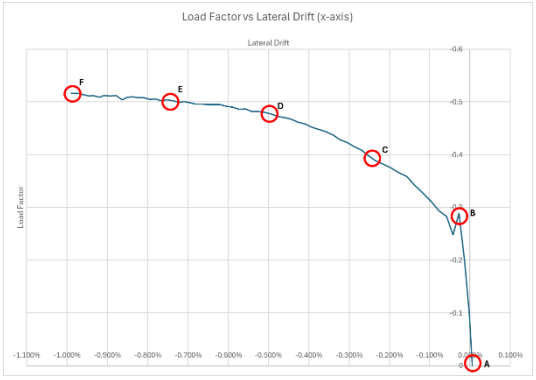 A to B, elastic limit	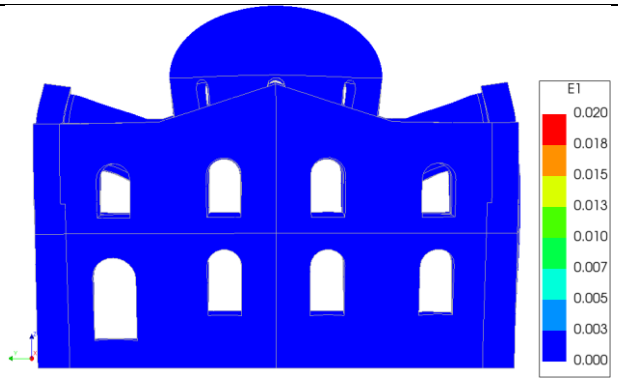 Load factor 0.29g Wall uncracked; no E1 bands visible.
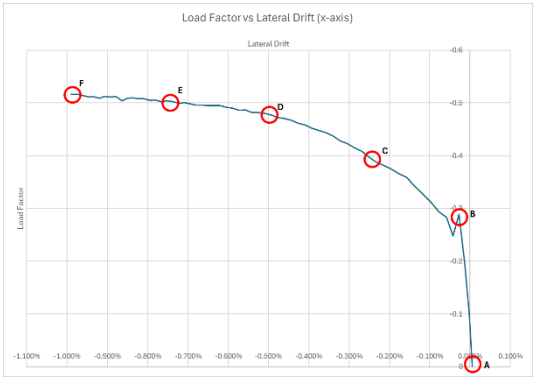 B to C, first cracking around opening and interior arches	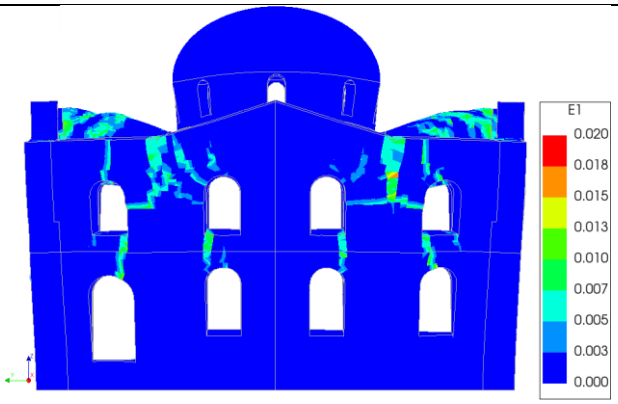 Load factor 0.36g Cracks localize at arch shoulders and propagate diagonally toward the mid-height course. Isolated flexural cracks appear around window openings.
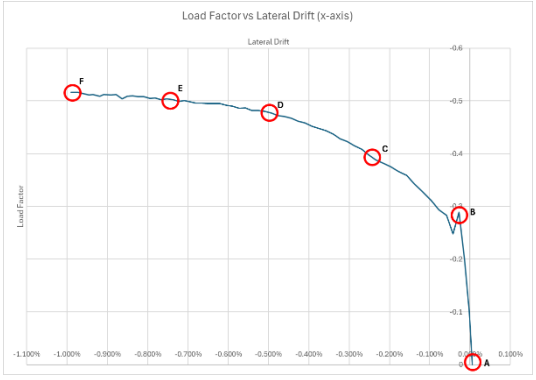 C to D, strain band extend	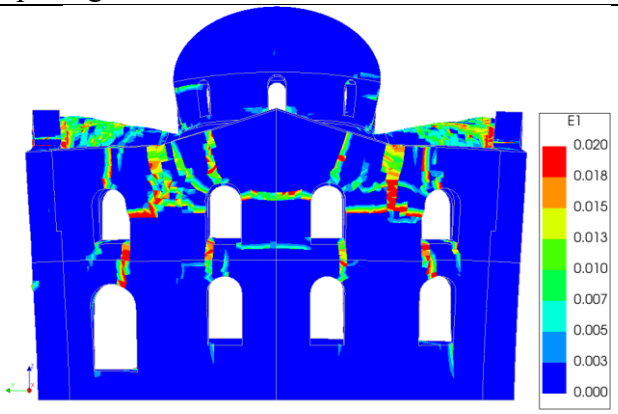 Load factor 0.46g Clear two-way diagonal fields around window bays and a developing horizontal band along the mid-wall line between lower and upper

Pushover X-, West Wall (Out-of-Plane Loading)	
Load Step	**Principal Strain Distribution**
	windows, indicating out-of-plane bending combined with in-plane shear.
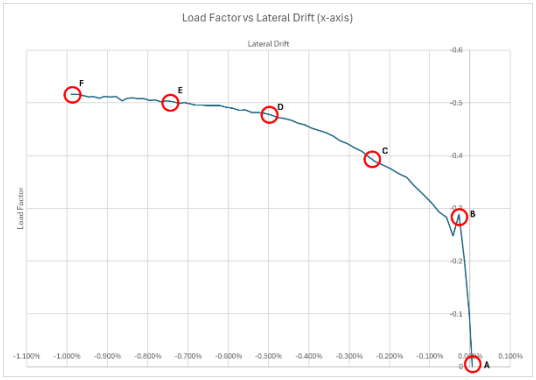 D to E, Hinge lines approaching continuity	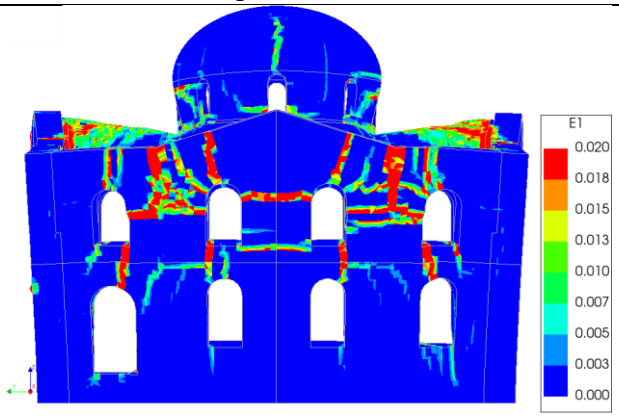 Load factor 0.50g Strain band intensifies (nearing maximum value), forming continuous strips along the mid-wall zone and around window openings, suggesting development of flexural hinges; arch crowns and shoulders show strong opening, with cracks extending toward the corner.
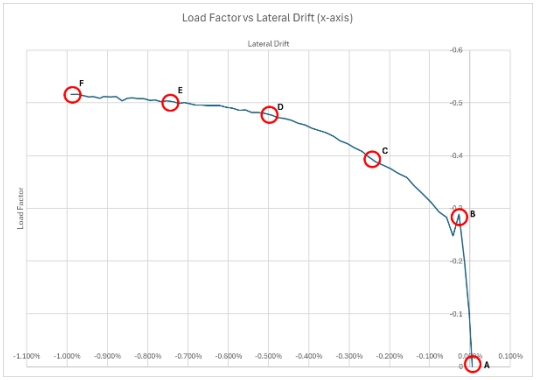 E to F, approaching maximum load	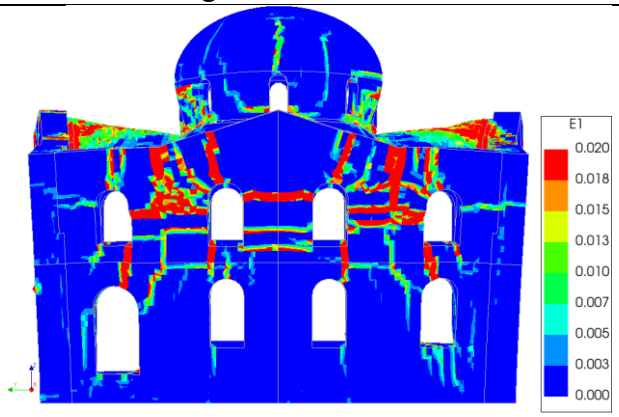 Load factor 0.52g The crack network coalesces into storey-height mechanisms: (i) a near-continuous horizontal cracking line along the level of the window tops, (ii) an additional horizontal cracking line across the wall opening, and (iii) diagonal links between corners and openings. Local separation is pronounced beside the openings and at the roof–wall interface.

Under pushover X- analysis, the West Wall section (loaded out-of-plane) progresses from first cracking at the top of the wall and beside the openings to a coupled flexure and shear pattern.

A horizontal cracking line forms above the openings, another develops near the top edge, and diagonal cracks traverse the window bays.

These features indicate a tendency toward out-of-plane flexural response about levels above the openings with localised shear sliding. However, the crack fields remain discontinuous, and no persistent cracking at the base is visible. Rotations concentrate above the openings while the areas between openings remain engaged. This, together with restraint from the orthogonal return walls and diaphragm (evident from limited separation near the top edge rather than full length detachment), suggests the mechanism stabilised without losing support, that is, significant damage but no instability trigger.

In short, the wall developed a damage-controlling out-of-plane flexural and shear mechanism that is consistent with the section not collapsing, while still highlighting vulnerabilities around the openings that could lead to major damage if demands were higher or ties weaker.

The response up to 0.29 g mirrors X+, with all control points tracking the same envelope. Beyond that, divergence grows as panels begin to act more independently. The west façade, loaded out-of-plane in this case, attracts the larger drifts while the north/south tips (in-plane) remain comparatively small. Bands form near the roof line and the level of the upper openings, with stepped diagonals linking corners and window sides. The plateau and minor snap-backs reflect progressive panel rocking/sliding; strength is taken from the envelope up to the post-yield plateau for interpretation and for the N2 bilinearisation.

5.1.4. Pushover Y-

From capacity curve in Figure 5-6 below, it is evident that for pushover in negative y direction, each control point display the opposite of result seen in positive y direction (Figure 5-4) in terms of how they behave. In terms of loading limit, loading in negative y direction shows elastic limit at 0.277g (slightly smaller than positive y direction), with slightly larger maximum load at 0.492g in comparison to pushover in positive y direction.

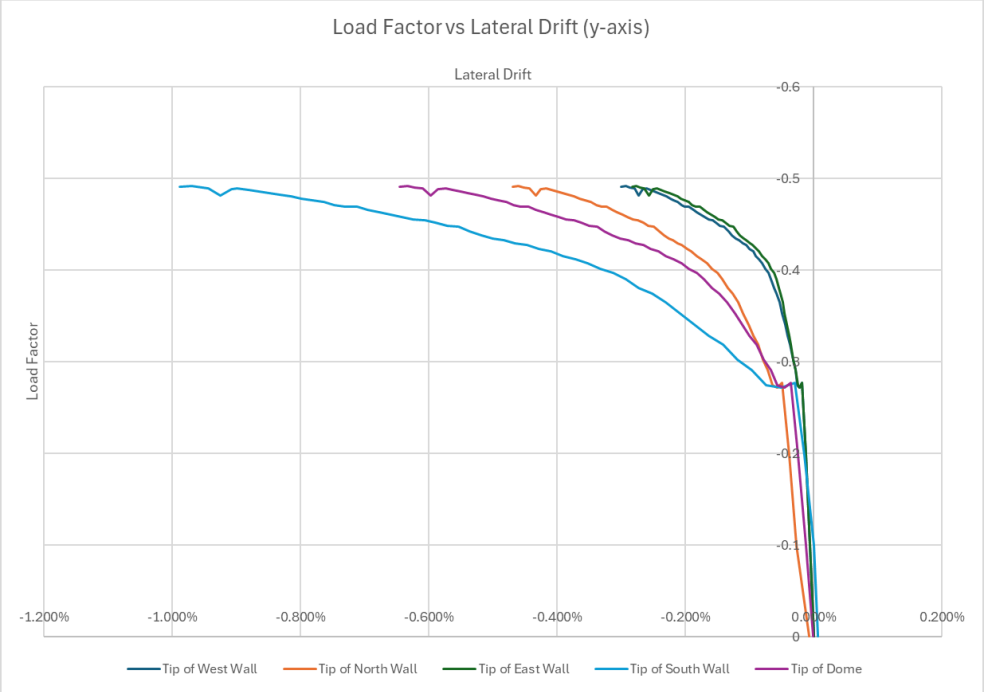

Figure 5-6 Sorted capacity curve of Pushover Y- analysis

In terms of behaviour as load progresses, pushover Y- once again shows that up to the elastic limit, each control point shows consistent behaviour, followed by individual ductility behaviour past elastic limit. Once again showing lack of box behaviour once elastic limit is reached. In addition, Tip of North Wall displays smaller drift compared to Tip of South Wall (loaded out-of-plane), while the Tip of East and West walls show even smaller drift. This result confirms what's been explain in previous pushover cases where walls that are loaded in-plane (in this case East and West) showing smaller lateral drift, while control points where their respective walls were loaded out-of-plane (North and South) show larger drift, and especially for node directly coincides with loading direction (South, negative y direction).

When observing principal strain progression, strain progression from pushover analysis in Y-direction (at load factor 0.43g) on West Wall section seems to be in line with the actual damage on-site (Figure 5-7), where several diagonal cracks, similar to previous result in Pushover X+, were formed near the window openings on the wall.

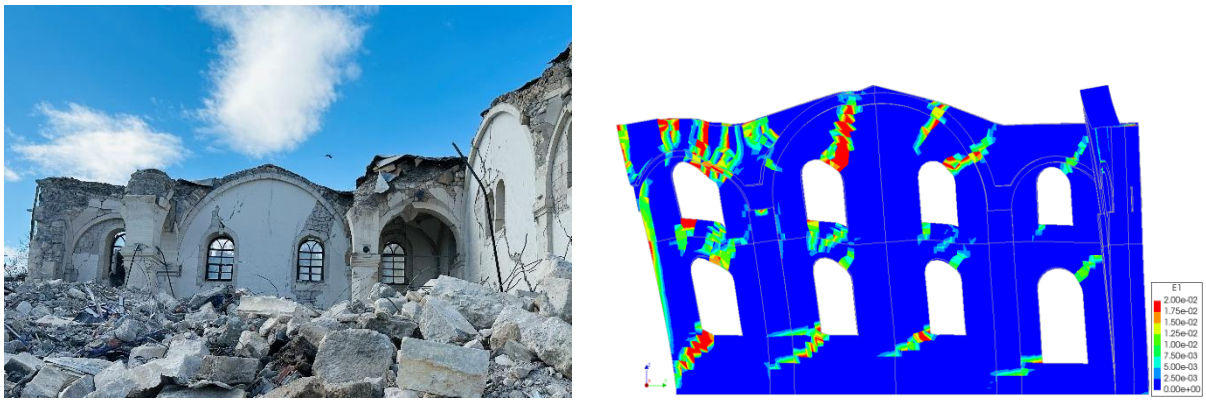

Figure 5-7 Comparison of actual (left) and numerical (right) damage on West Wall (0.43g)

This correlation between actual damage and simulated strain accumulation once again highlights the model's capability to predict and capture realistic damage progression, despite some damage that comes from the result did not appear on the actual one.

Table 5-5 Principal Strain Progression of West Wall Section (Pushover Y-)

Pushover Y-, West Wall (In-Plane Loading)	
Load Step	**Principal Strain Distribution**
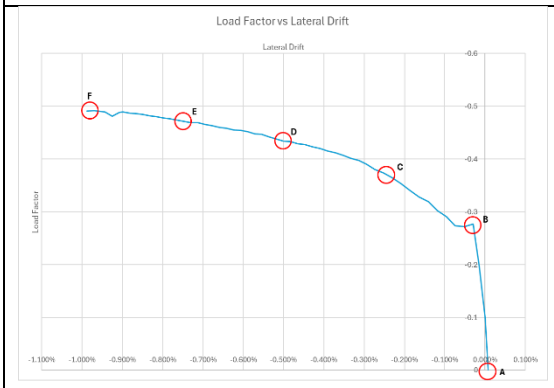 A to B, elastic limit	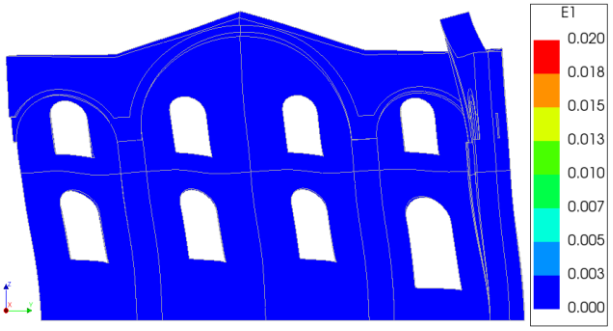 Load factor 0.28g The wall remains largely uncracked
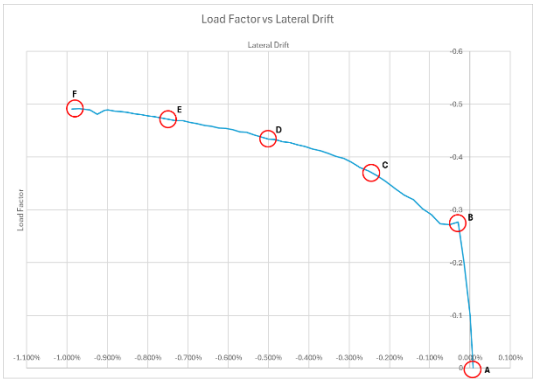 B to C, initial crack	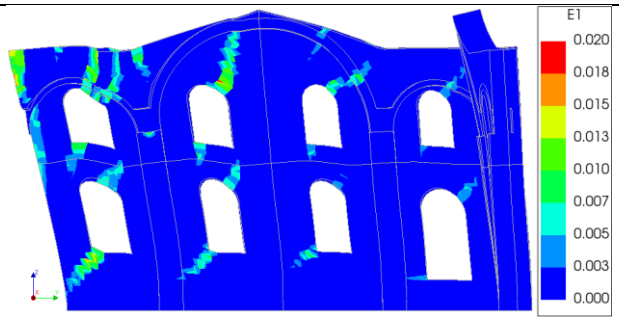 Load factor 0.34g Fine diagonal cracks appear at the upper corners of the window openings and along the short wall segments between openings; light horizontal cracking develops at the level of the upper-storey opening tops.
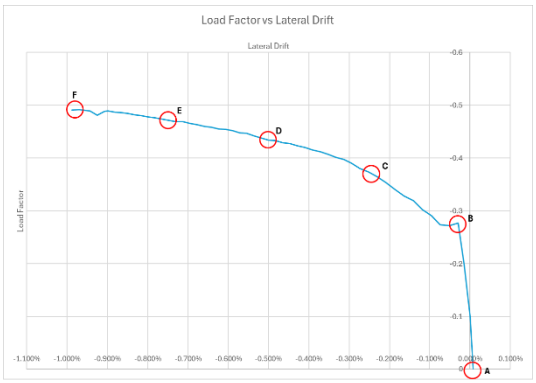 C to D, shear pattern forming	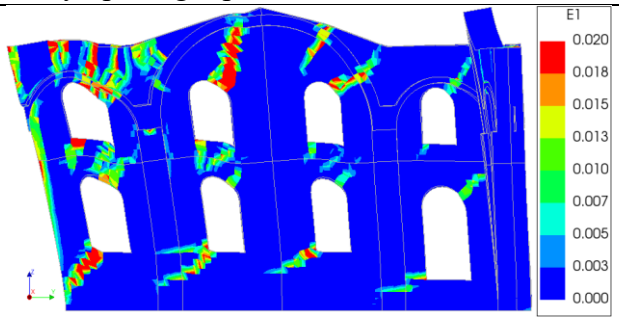 Load factor 0.43g Diagonal cracking intensifies in the wall zones between openings; vertical cracks initiate beside several openings, linking into stepped paths down toward the base of the openings.

Pushover Y-, West Wall (In-Plane Loading)	
Load Step	**Principal Strain Distribution**
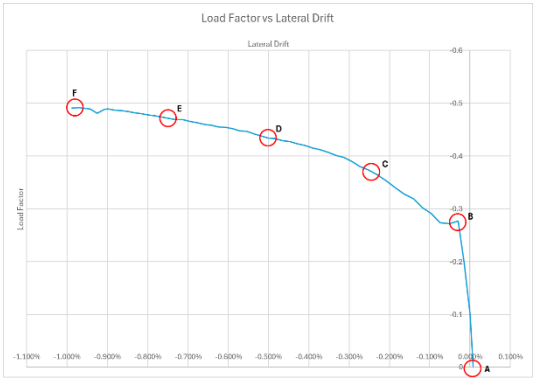 D to E	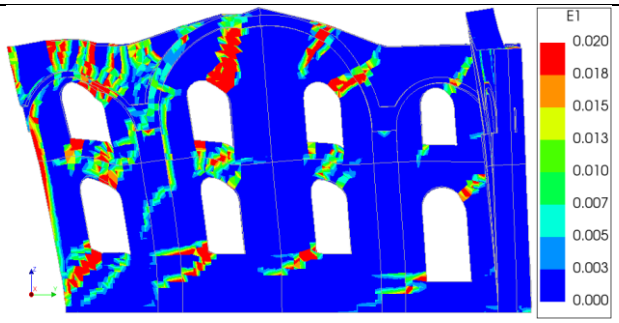 Load factor 0.47g A more continuous horizontal band develops along the upper-storey alignment between windows, with stronger diagonal cracks rising toward the gable apex; local crushing/tension occurs.
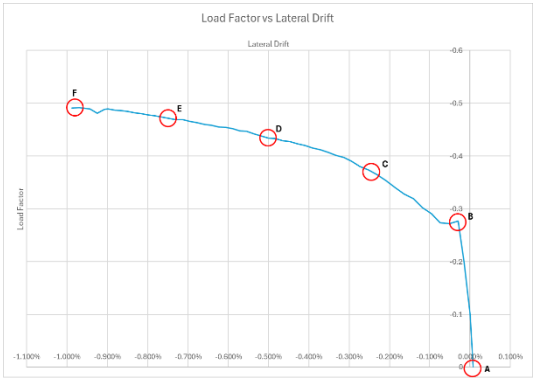 E to F, approaching max load	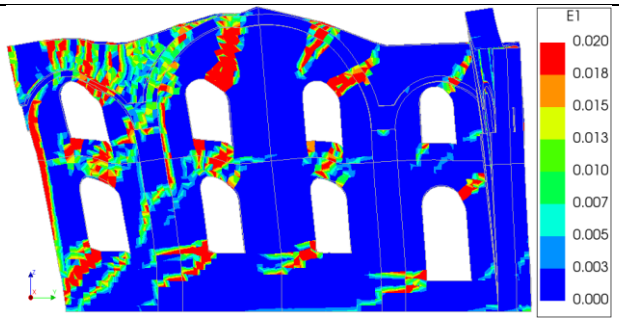 Load factor 0.49g The horizontal band across the upper-storey is continuous, with pronounced diagonal cracks connecting adjacent openings; additional diagonal cracks form below, but the wall retains overall alignment with no clear out-of-plane separation.

While West Wall section is seen to survive the earthquake, South Wall section, which suffers the largest lateral deformation from Pushover Y- loading (Figure 5-6) did not. Table 5-6 below shows the strain progression on South Wall section due to out-of-plane loading to assess whether it may contribute to the cause of the collapse.

Table 5-6 Principal Strain Progression of South Wall Section (Pushover Y-)

Pushover Y-, South Wall (Out-of-Plane Loading)	
Load Step	**Principal Strain Distribution**
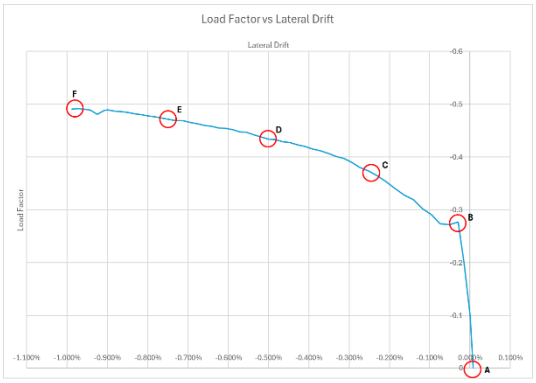 A to B, elastic limit.	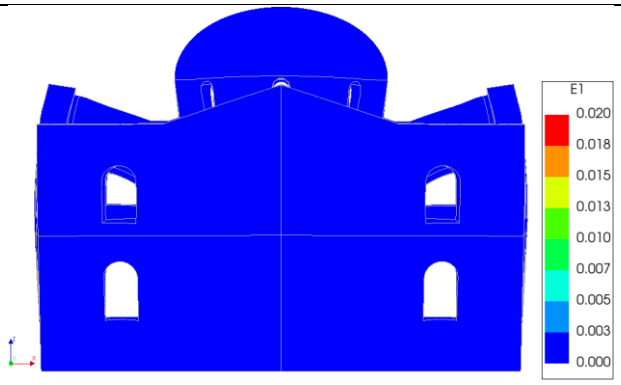 Load factor 0.28g Wall section are largely uncracked
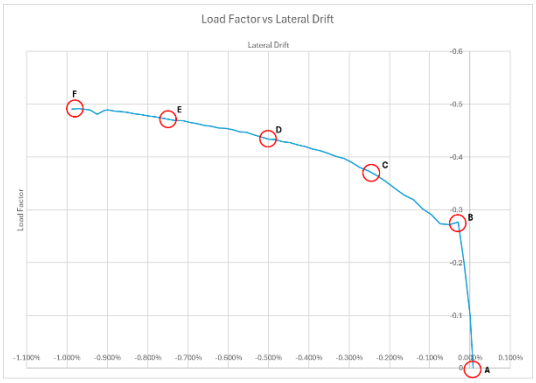 B to C, crack onset	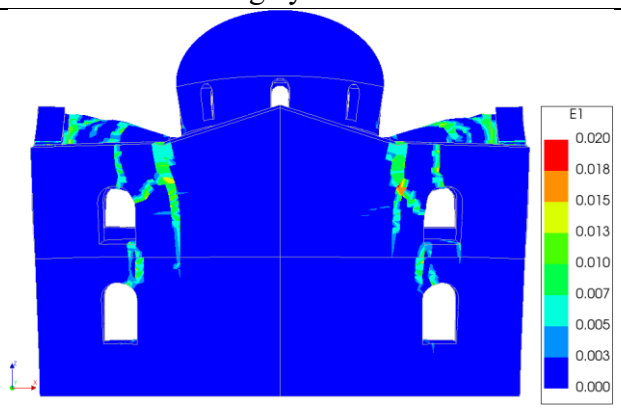 Load factor 0.34g Initial cracking forms above the openings (near the tops of the windows) and just below the roof level. Short vertical cracks develop beside the openings. Local diagonal tension initiates near the roof-wall junctions.
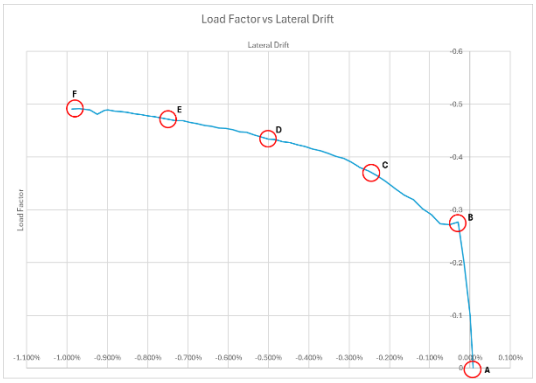 C to D, crack starts spreading	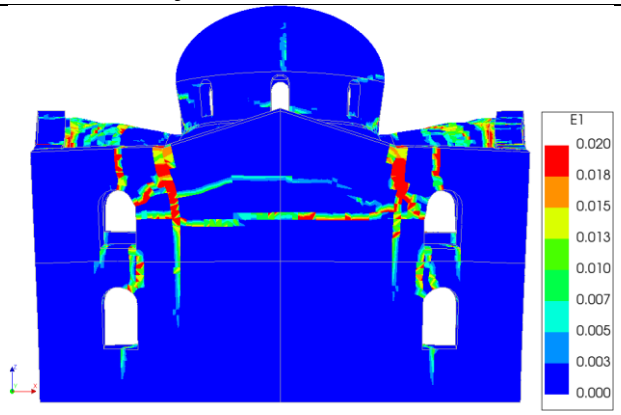 Load factor 0.43g Cracks widen and begin to link horizontally near the top zone. Stepped diagonal cracks connect

Pushover Y-, South Wall (Out-of-Plane Loading)	
Load Step	**Principal Strain Distribution**
	the top zone to the sides of openings and down toward the next horizontal course. Initial tension/sliding is visible at base corners.
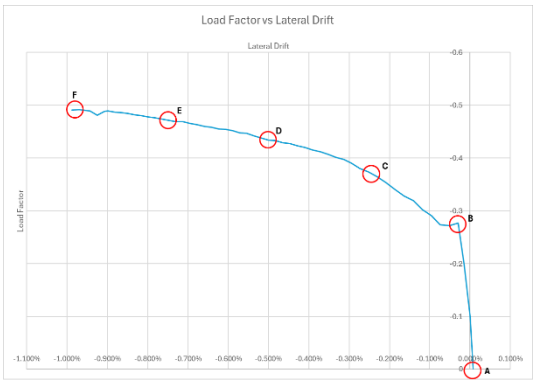 D to E, localization	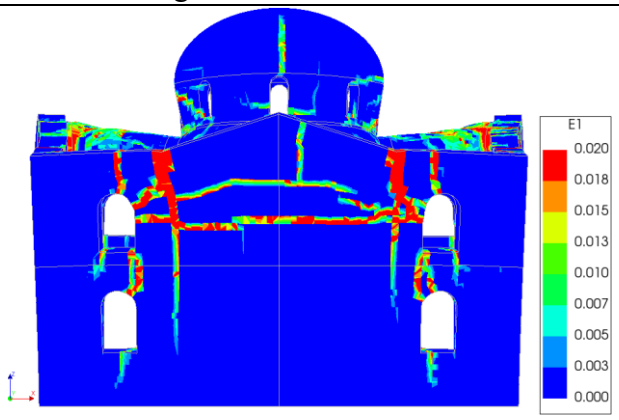 Load factor 0.47g Two principal horizontal cracking lines are evident: one near the roof level and another at the level of the window tops. Cracking concentrates near wall edges; vertical cracks beside openings lengthen. An out-of-plane flexural response of wall segments about the base becomes apparent.
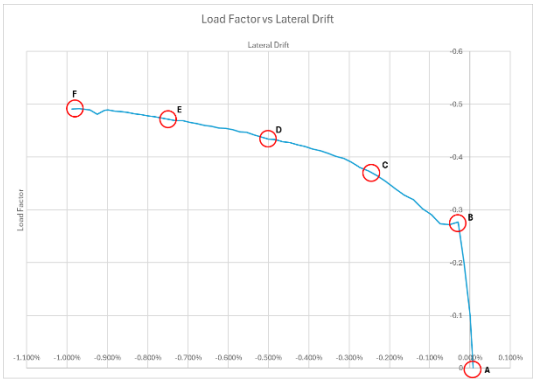 E to F, max load	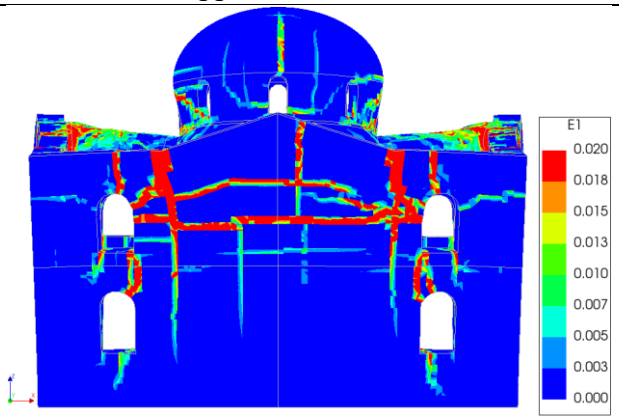 Load factor 0.49g The two horizontal bands are nearly continuous across the façade; vertical splitting beside openings links them. Local sliding bands develop along parts of the base, indicating a low margin against out-of-plane instability.

Under pushover Y- loading, the south wall evolves toward a two-level bending pattern: one horizontal cracking level near the top of the wall and a second at the level of the window tops, linked by vertical cracking beside openings and stepped diagonals. This sequence implies

progressive out-of-plane flexural rotation of wall segments and local sliding at the base, which substantially reduces out-of-plane capacity. While this wall did collapse in the real event, the pushover results here are presented to highlight damage patterns and mechanisms that could contribute to major deterioration, not to assert the exact collapse sequence.

The pre-yield branch is consistent with the other directions. After 0.29 g, the south façade, now out-of-plane, goes to higher drifts, with a clear two-band pattern and short diagonals around openings. The post-yield plateau shows modest undulations, consistent with panel-by-panel localisation and displacement control. For later checks and for N2, the capacity curve is idealised by a bilinear passing through an effective yield point and the maximum base reaction.

Table 5-7 Summary of Pushover Analyses Result

No	Analysis	Elastic Limit (g)	Max Load (g)	Note
1	Pushover X+	0.289	0.525	East Wall Largest Out-of-Plane Drift
2	Pushover Y+	0.282	0.457	North Wall Largest Out-of-Plane Drift
3	Pushover X-	0.289	0.516	West Wall Largest Out-of-Plane Drift
4	Pushover Y-	0.277	0.492	South Wall Largest Out-of-Plane Drift

5.1.5. Single Wall Comparison (North and East)

As an early consistency check, isolated wall models were analysed in pushover and compared with the full building. The intent was not to derive capacities from wall-only models, but to verify that the fixed/rotating total-strain crack (TSC) options produced plausible mechanism trends.

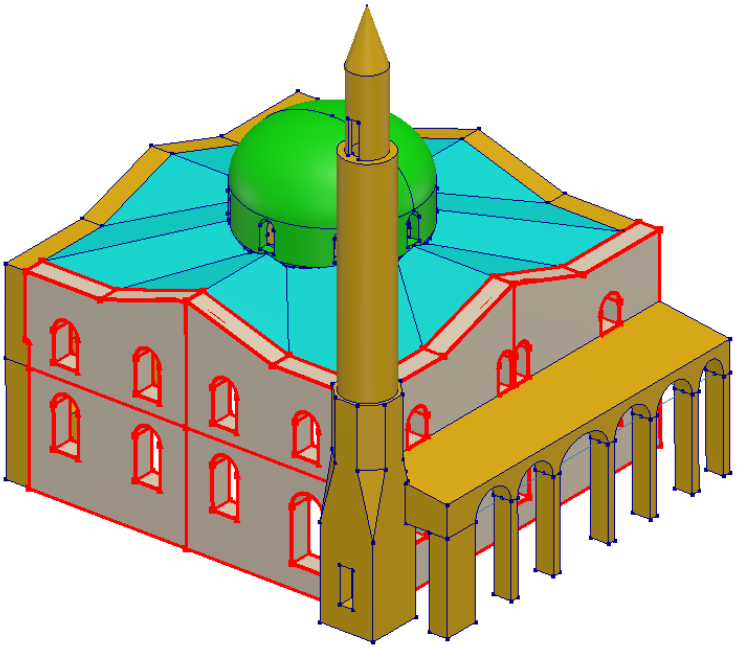

Figure 5-8 Overview of Full Model with North and East Walls Highlighted for Single Wall Analysis

The East and North façades were extracted from the full model and analysed as individual walls. Their vertical edges were restrained in the in-plane direction, the top edges were free, and the bases were fixed. Material parameters were kept identical to the building model; only the TSC option was varied between fixed and rotating. Loading directions mirrored the full-model cases, with the East wall loaded in the X (out-of-plane) direction and the North wall in the Y (out-of-plane) direction. Crown displacement at each wall served as the control degree of freedom.

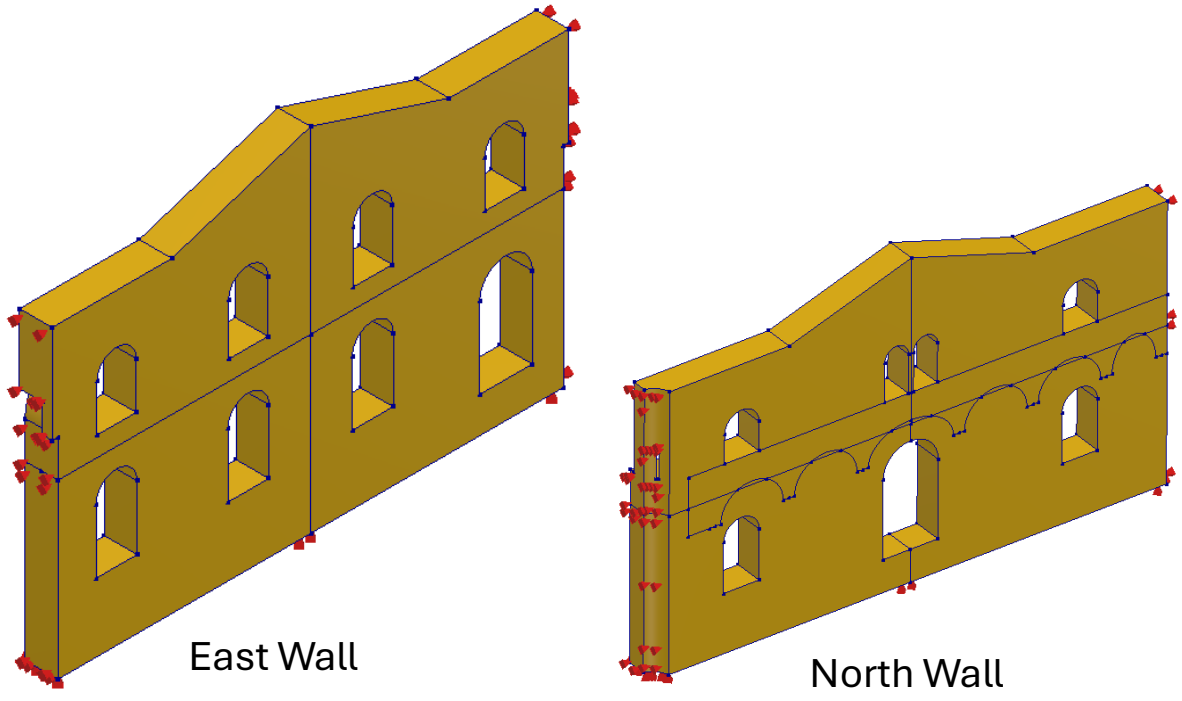

Figure 5-9 Extracted Wall Models for Separate Analysis

For the North wall in the Y direction, the fixed and rotating TSC options produced very similar load–drift curves and strengths, both much lower than the corresponding full-building response.

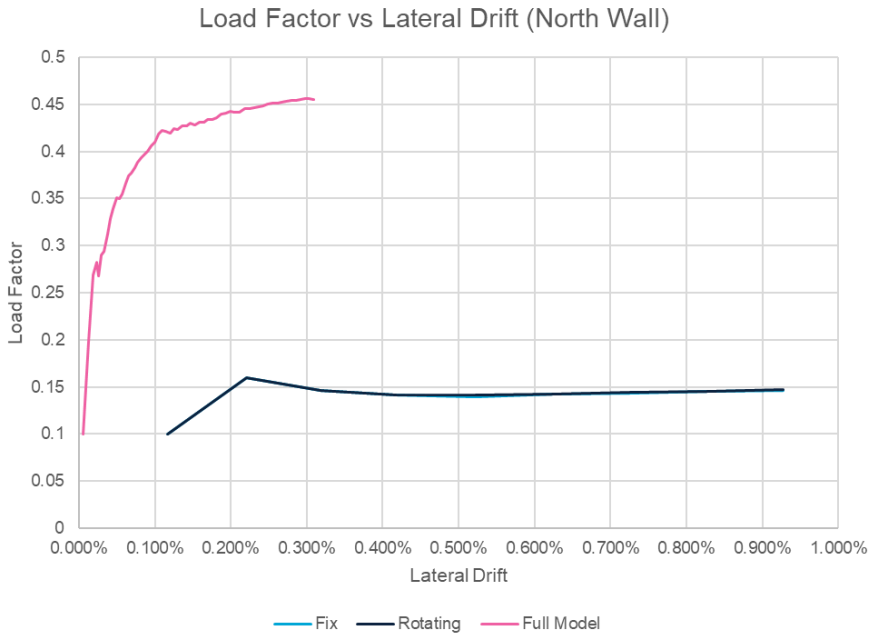

Figure 5-10 Analysis Comparison of North Wall Under Different Pushover Y+ Setups

For the East wall in the X direction, the rotating option showed higher initial stiffness and better ductility than the fixed option, yet both wall-only curves still lay well below the full-building curve.

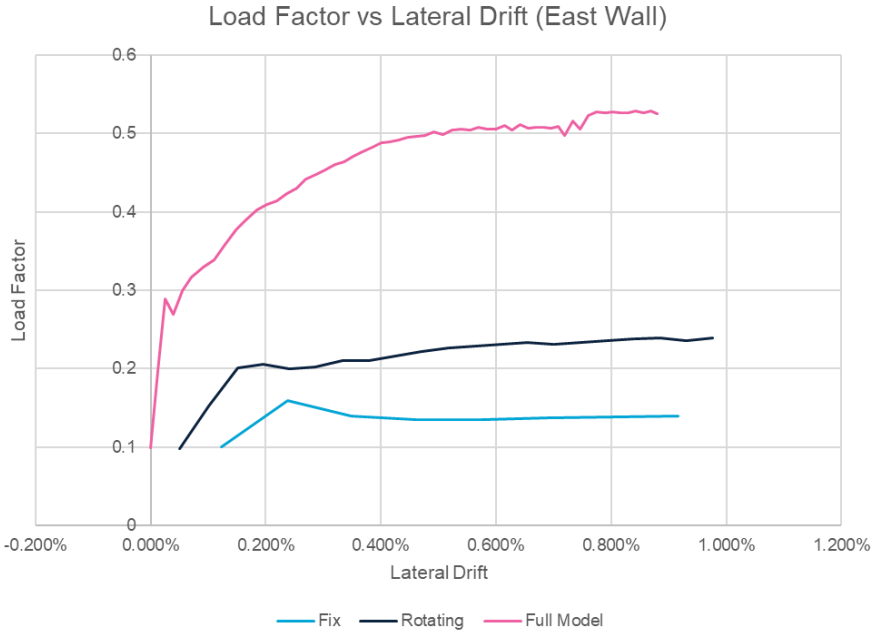

Figure 5-11 Analysis Comparison of East Wall Under Different Pushover X+ Setups

The full model was consistently stiffer and stronger because it mobilised three-dimensional restraint from transverse walls, vaults and arches, diaphragm participation, and some torsional

or minaret interactions that isolated walls cannot capture. Mechanism trends were consistent across models: out-of-plane vulnerability concentrated at upper panels and around openings, and the rotating option tended to delay localisation slightly relative to the fixed option.

These wall checks are conservative and mechanism-oriented; they do not replace the full-building pushover for capacity reads and they do not alter the interpretations in Sections 5.1.1 to 5.1.4 or the N2 assessment. They are included for transparency and to document that the building-scale model is the appropriate basis for capacity evaluation.

Table 5-8 Summary of Single Single Wall Analysis Comparison

Wall/Analysis	Elastic Limit (g)	Max Load (g)	Notes
North Wall			
North wall - Full model (Y+)	0.282	0.457	Higher due to 3D restraint
North wall - Single wall – Fixed crack (Y+)	0.160	0.147	Fixed and rotating crack model are nearly identical
North wall - Single wall – Rotating crack (Y+)	0.160	0.146	
East Wall			
East wall - Full model (X+)	0.289	0.525	Higher due to 3D restraint
East wall - Single wall – Fixed crack (X+)	0.160	0.140	Lowest stiffness and strength
East wall - Single wall – Rotating crack (X+)	0.201	0.239	Rotating > fixed, in terms of stiffness and ductility

5.2. Performance Point Calculation

To estimate the mosque's seismic performance without running nonlinear time-history analysis, the N2 method is applied. The nonlinear static pushover curve is converted to an equivalent first-mode SDOF system in ADRS coordinates using the modal participation factor Γ and the effective modal mass m^* from the eigenvalue analysis. Following EC8 Annex B and Fajfar's N2, the spectrum–capacity intersection is taken on the equal-energy bilinear SDOF envelope, not on the equivalent SDOF curve, to ensure consistency with the elasto-plastic SDOF assumptions of the inelastic spectra. Using the equal-energy bilinear preserves global strength and deformation capacity of the equivalent SDOF while removing local serrations that can cause multiple crossings, so the performance point is unique and method-consistent.

The control coordinate is the average of five roof points and the first mode is scaled so that the modal component at the control coordinate equals one, $c^T\phi_{control} = 1$. The mapping is

$$F^* = \frac{V_b}{\Gamma}, \qquad d^* = \frac{d_{control}}{\Gamma}, \qquad (5-1)$$

$$S_a = \frac{F^*}{m^*}, \qquad S_d = d^*, \qquad (5-2)$$

The SDOF capacity is idealised to a bilinear envelope and plotted against the site-specific inelastic spectrum. The primary read is whether the spectrum intersects the capacity on the elastic branch (strength clearly sufficient) or on/near the plateau (strength engaged, check ductility and drift). The formal "performance point" ($S_{d,t}$, $S_{a,t}$) is then taken at the intersection for reporting, with mapped values

$$d_{roof,t} = \Gamma\, S_{d,t}, \qquad V_{b,t} = \Gamma\, m^* S_{a,t} \qquad (5-3)$$

Following EC8 Annex B and Fajfar's N2, the demand–capacity check must use an elasto-plastic SDOF idealisation; the equal-energy bilinear preserves the area (strength × deformation) of the equivalent SDOF curve while removing local serrations, ensuring a unique and method-consistent intersection.

The control displacement is defined as the average of five roof points, presented in pushover analyses result, to reduce local noise and torsional bias. This choice is justified by:

- Averaging suppresses local irregularities and minor asymmetries,
- It approximates a mass-centre measure when torsion is limited, and
- Sensitivity checks with single points give comparable initial slopes. This follows common practice for macro models of masonry buildings (Fajfar, 1999; Eurocode 8 Annex B; Tomaževič, 1999).

With value of Γ = 2.544, a SDOF scaled from MDOF capacity curve can be obtained.

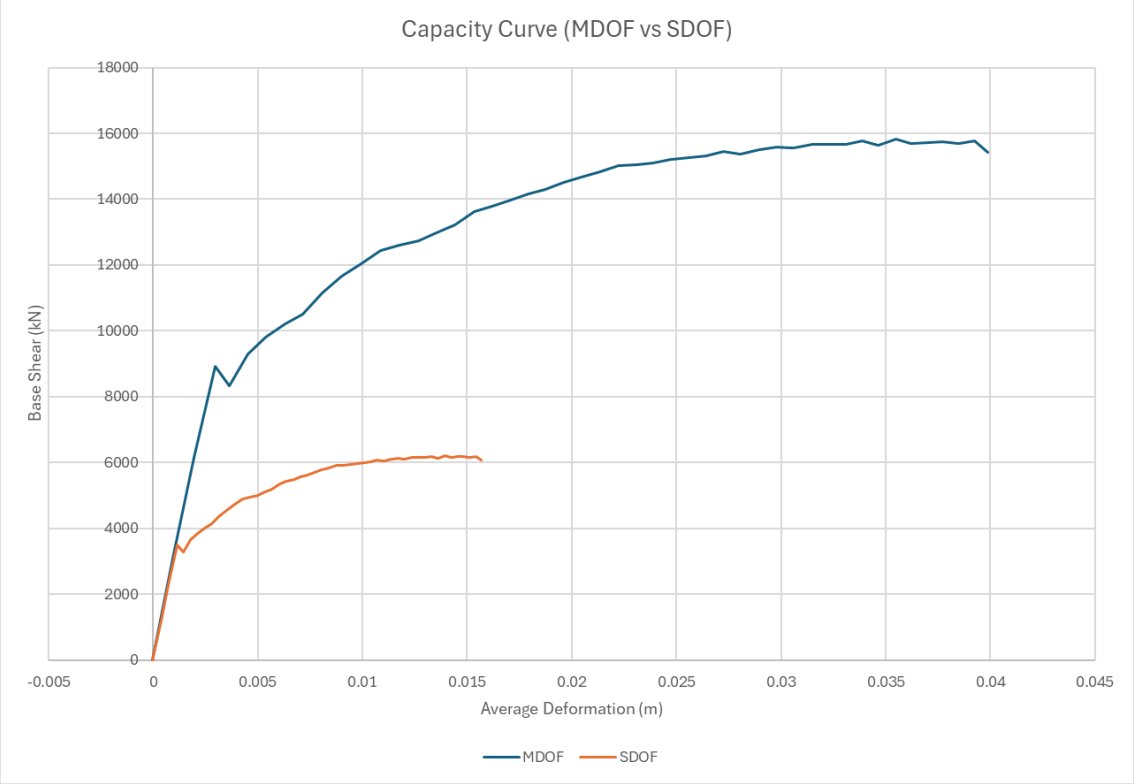

Figure 5-12 Comparison of MDOF and SDOF Capacity Curve

The N2 method compares demand with a bilinear idealisation of the first-mode SDOF capacity because both the inelastic spectra and the reduction rules are derived for an elasto-plastic SDOF oscillator defined by a yield point and ductility. The equivalent SDOF curve from pushover often contains local serrations and softening plateaus due to progressive localisation and solver effects; intersecting the spectrum with that raw curve can produce multiple or spurious crossings. The equal-energy bilinear smooths these details while preserving global strength and deformation capacity, yielding a unique intersection that is consistent with the assumptions of the demand model and with EC8 Annex B and Fajfar's formulation of N2. The equivalent SDOF curve is still useful for context, but the performance point and acceptability checks must be read on the bilinear envelope for methodological consistency.

The SDOF curve is idealised to a bilinear elastic–plastic envelope, following equal-energy rule of Tomaževič (1999), which are:

1. Determine the initial elastic stiffness k_e from the scaled SDOF curve by determining critical deformation (d_{cr}), and the corresponding critical base shear force (F_{cr}), where then elastic stiffness k_e can be calculated as $\frac{F_{cr}}{d_{cr}}$,
2. By calculating the equivalent ultimate shear force (Fu,eq) from equation

$$F_{u,eq} = k_e \left(d_{u,eq} - \sqrt{{d_{u,eq}}^2 - \frac{2A_{env,exp,u,eq}}{k_e}} \right) \qquad (5-4)$$

3. Where $d_{u,eq}$ is the corresponding deformation for $F_{u,eq}$, while $A_{env,exp,u,eq}$ is the enveloped area below the capacity curve, with same value for both SDOF equivalent and bilinear.
4. The maximum elastic deformation $d_{e,eq}$ can be then calculated following $k_e = \frac{F_{u,eq}}{d_{u,eq}}$

The calculations are essentially iterative process as there are two unknowns in equation 5-4 ($d_{u,eq}$ and $F_{u,eq}$), while $A_{env,exp,u,eq}$ can be calculated manually from SDOF equivalent curve. Once the value of $d_{u,eq}$ and $F_{u,eq}$ are obtained, the bilinear SDOF curve can be seen in the figure below

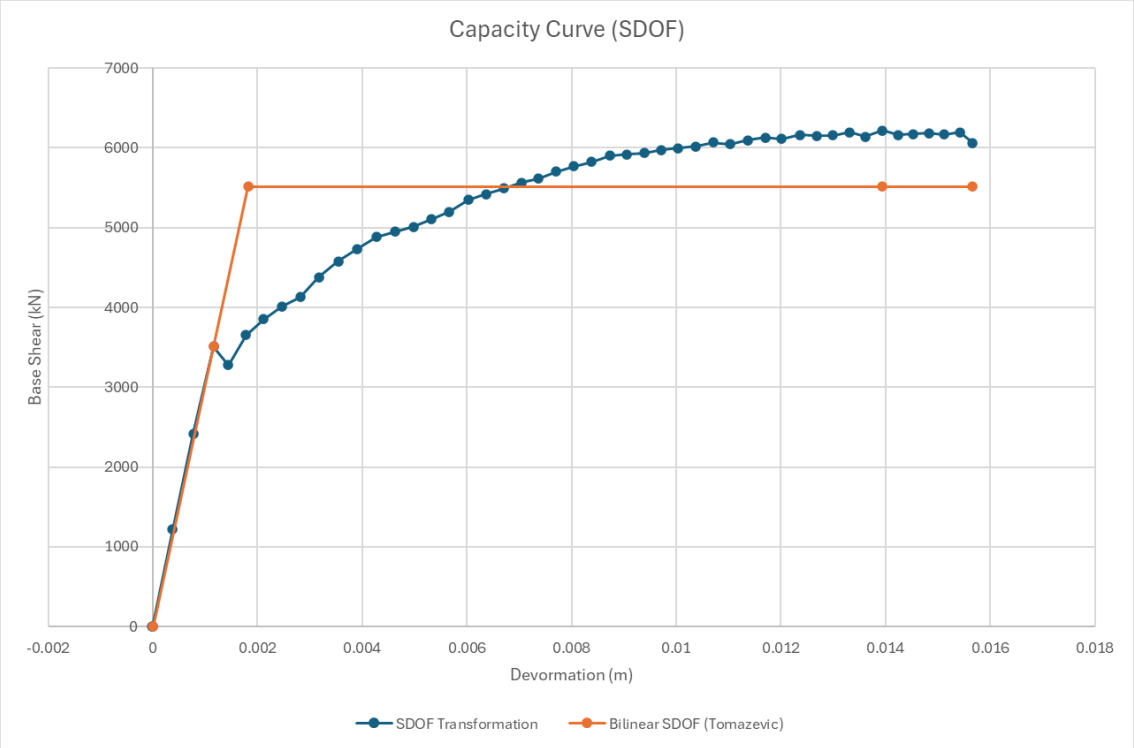

Figure 5-13 SDOF curve bilinearization

With the bilinear curve defined, the capacity is plotted in ADRS as (S_d, S_a), calculated according to equation 5-2. The elastic demand spectrum is placed in ADRS via

$$S_{a,ADRS,j} = S_{a,j}, \qquad S_{d,ADRS,j} = \frac{T_j^{\,2}}{4\pi^2} S_{a,j}, \qquad (5-5)$$

Where $S_{a,j}$ and T_j are the corresponding points from the demand response spectrum. By using site specific response spectrum, N2 capacity–demand check can be seen as

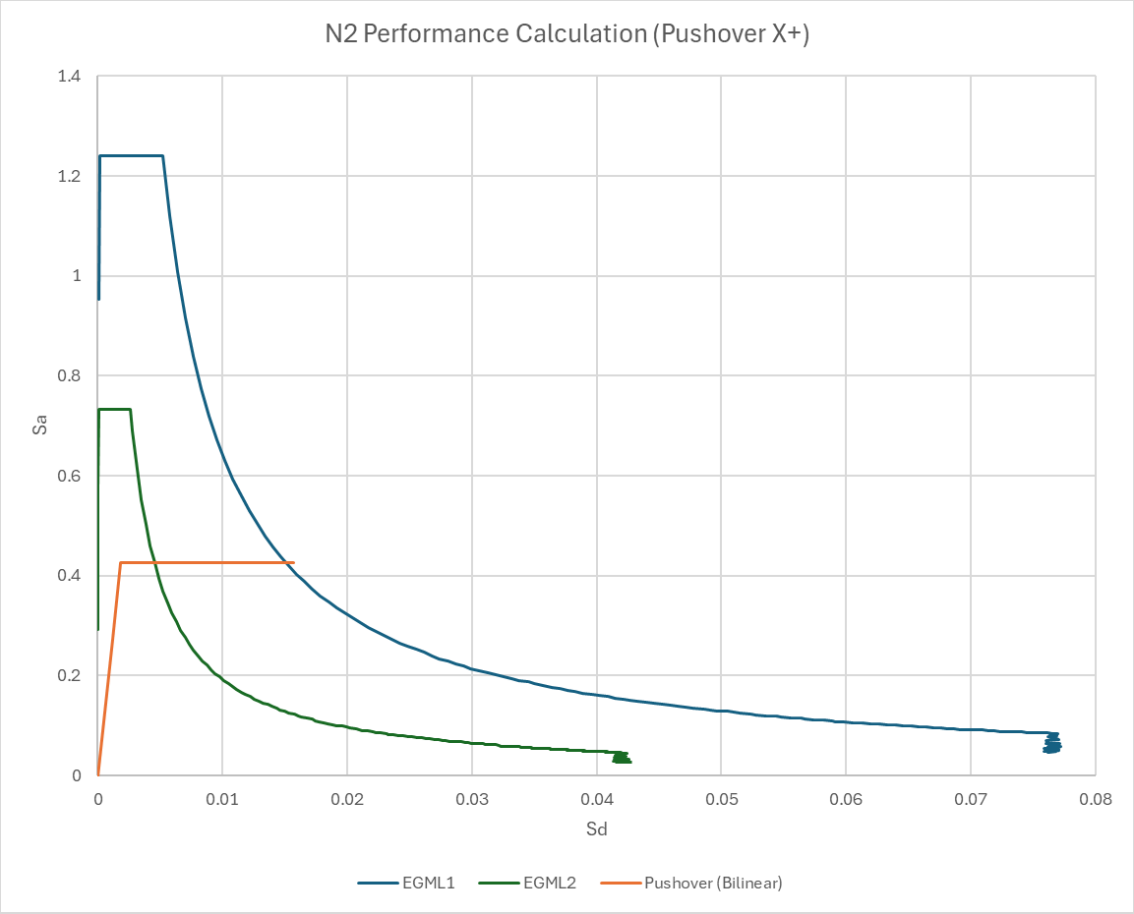

Figure 5-14 Capacity curve against site-specific response spectrum

From Figure 5-14 above, the bilinear SDOF capacity (orange) is met by both spectra on the horizontal plateau at about $S_{a,y}$ = 0.427 g. The elastic limit is exceeded in both cases (for Pushover X+), so first yield is reached for both components. Earthquake Ground Motion Level -2 (EGML2) cuts the plateau close to the knee, which implies a small ductility demand; EGML1 crosses further along the plateau, implying a larger ductility demand. Performance demand is therefore governed by the displacement at the intersection rather than by strength. This read is consistent with the pushover results: the elastic limit is about 0.28 - 0.29 g, peak strengths are about 0.46 - 0.53 g, and the plateau lies between them, indicating post-yield reserve before peak. The conclusion is that capacity is strength-controlled for both spectra; EGML2 requires modest ductility, while EGML1 requires more, and acceptability depends on the resulting drift.

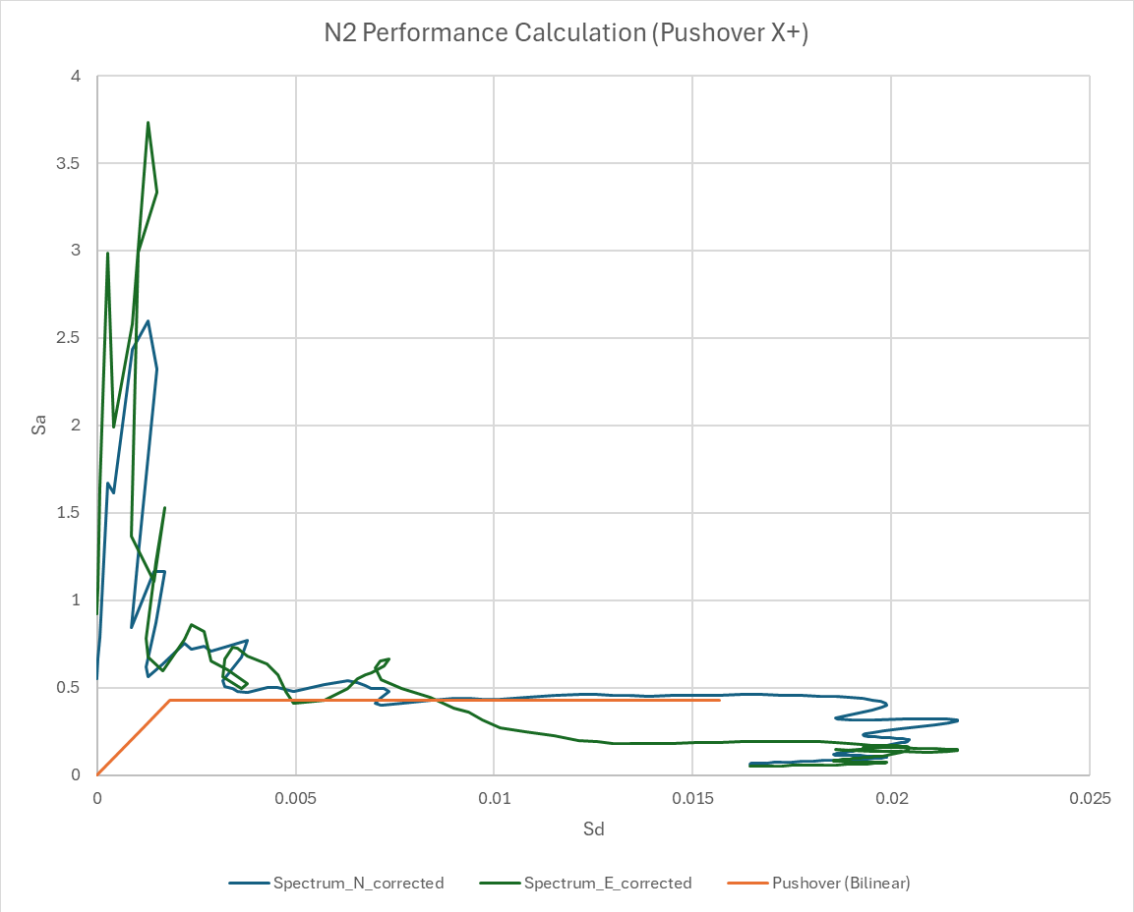

Figure 5-15 Capacity curve against 2023 Kahramanmaraş earthquake response spectrum

The N and E component spectra intersect the horizontal plateau of the bilinear SDOF capacity at about $S_{a,y} = 0.427$ g. The elastic limit is exceeded in both cases, so first yield is reached for both components. The E spectrum crosses the plateau close to the elastic limit, which implies a small ductility demand. The N spectrum crosses further along the plateau and then drops below it at larger S_d which implies a moderate ductility demand at the intersection. Early spikes above 1–3 g occur at very small S_d and reflect high-frequency content; they do not control the first-mode response near $T^* = 0.131$ s. This outcome is consistent with the pushover results, which show an elastic limit around 0.28 - 0.29 g and peak strengths around 0.46 - 0.53 g. The plateau at about 0.427 g lies between those values, confirming that both records trigger yield but do not require strength beyond the modelled peak; performance requirement is judged on displacement and drift at the intersection rather than on strength.

5.3. Discussion

After the initial elastic branch, the capacity curves flatten as tensile cracking and local compression damage spread, reducing tangent stiffness. Base reaction then stabilises while lateral drift continues to grow. The small slope changes (“ridges”) mark sequential localisation: different wall panels and arch–window zones start to contribute and soften at slightly different drifts. Short snap-back segments can appear when a concentrated band forms and resistance at the control DOF drops; under displacement control the solver continues to increase

displacement while the recorded force falls, and step size / tolerances can accentuate the jagged appearance. For strength reads, consequently, take the envelope up to the post-yield plateau and ignore the noisy tail. For the N2 procedure the curve is idealised as bilinear, using an effective yield point and the maximum attained base reaction (Section 5.2).

These traits are expected for monotonic pushover of historical masonry, but the method has known limits: it omits cyclic degradation and does not update the lateral pattern as modal content evolves. As a result, fixed-pattern pushover can overestimate strength and under-predict deformation capacity compared with cyclic or incremental dynamic procedures, particularly for irregular masonry where higher-mode participation changes with damage (e.g., Aşıkoğlu et al., 2020/2021; D'Altri et al., 2020). In this study those limits were acknowledged by (i) interpreting the curves at the level of mechanisms (bands near opening or floor levels, vertical splits beside openings, stepped diagonals) rather than as literal crack maps, and (ii) cross-checking key reads with time-history results in Section 6. Principal-strain (E_1) plots from smeared-crack models are thus used as indicators of likely cracking zones, not as exact fracture traces (Betti & Vignoli, 2011; D'Altri et al., 2020).

The capacity figures in Table 5-7 and the bilinear/SDOF transformation used for Section 5.2 follow this reading (envelope to the post-yield plateau, then bilinear for the N2 check). The MDOF to SDOF transformation in N2 is a first-mode approximation. It performs well for predominantly first-mode, regular systems, but accuracy diminishes when higher modes, torsion, or localised wall mechanisms influence the global response, conditions typical of historic masonry and complex roof–wall interactions. Consequently, pushover/N2 results are cross-checked with time-history analyses to capture cyclic degradation, sequence effects, and demand redistribution.

6. Nonlinear Dynamic Analysis

This chapter evaluates the seismic response of the mosque under the recorded ground motion using the validated macro-FE model, in order to quantify peak lateral demands and their timing, compare displacement and cracking trends with pushover and N2 assessments, and establish a reference for the neighbour-interaction study.

At a glance, the time-history results exhibit narrow elastic hysteresis loops at the start of shaking, then widening loops as cracks open and close cyclically, followed by dominant cycles in the strong-motion window where stiffness degrades and higher-mode participation increases. Peak displacements and base reactions align with the main pulses of the record. Principal-strain maps show horizontal cracks above openings, diagonal bands between openings, and local rotation lines at window and arch–wall junctions, with mild torsional participation that weakens box behaviour. These features corroborate the mechanisms inferred from pushover while revealing their cyclic evolution under realistic loading.

Base excitation is prescribed as uniform translational accelerations in the X and Y model axes, applied simultaneously; time integration uses a fixed step $\Delta t = 0.01$ s. Motion processing (baseline correction and intensity framing) follows 3.4.4. Section 6.1 summarises the windows used and the adopted damping (derivation in Appendix A).

Key response metrics are:

a. Base accelerations versus input (sanity check),
b. Base reactions F_x, Fy,
c. Control-point displacements and drifts
d. Strain maps at the times of peak displacements, and
e. Force-displacement (hysteresis) loops.

It should be noted that nonlinear static (pushover) and nonlinear dynamic (time-history) analyses are not directly comparable in absolute terms. Pushover applies monotonic lateral loading with a fixed force pattern, while dynamic analysis captures cyclic, time-dependent loading and higher mode participation. In this study, pushover results are used primarily to establish capacity bounds and likely failure mechanisms, whereas dynamic analysis provides insight into transient demands, cyclic opening and closing of cracks, and overall stability under realistic loading.

6.1. Input Motion and Damping

The horizontal ground motion records from the nearest strong-motion station were baseline-corrected and imposed as uniform base accelerations in DIANA. Full processing details are provided in Section 3.4.4 (full records and Arias-intensity plots). This section specifies the selected analysis windows and the damping adopted for the dynamic runs.

The original records span 0–25.19 s. Cumulative Arias intensity was computed, and two windows were extracted (Figure 6-1):

- **Window A** (reference run): 13.14–25.19 s (12.05 s), starting when the Arias intensity exceeded 2%. This excludes low-energy pre-shaking and long-period drift from micro-motion.
- **Window B** (short/interaction runs): 23.14–25.19 s (2.05 s), focusing on the strong pulses where the Arias intensity exceeded 50%. This provides rapid verification and ensures a consistent intensity frame for the neighbour-interaction study.

Both components were applied simultaneously in X and Y with a constant time step of Δt = 0.01 s and no additional scaling. The selected ground motion windows are shown in Figure 6-1, and their key parameters are summarised in Table 6-1.

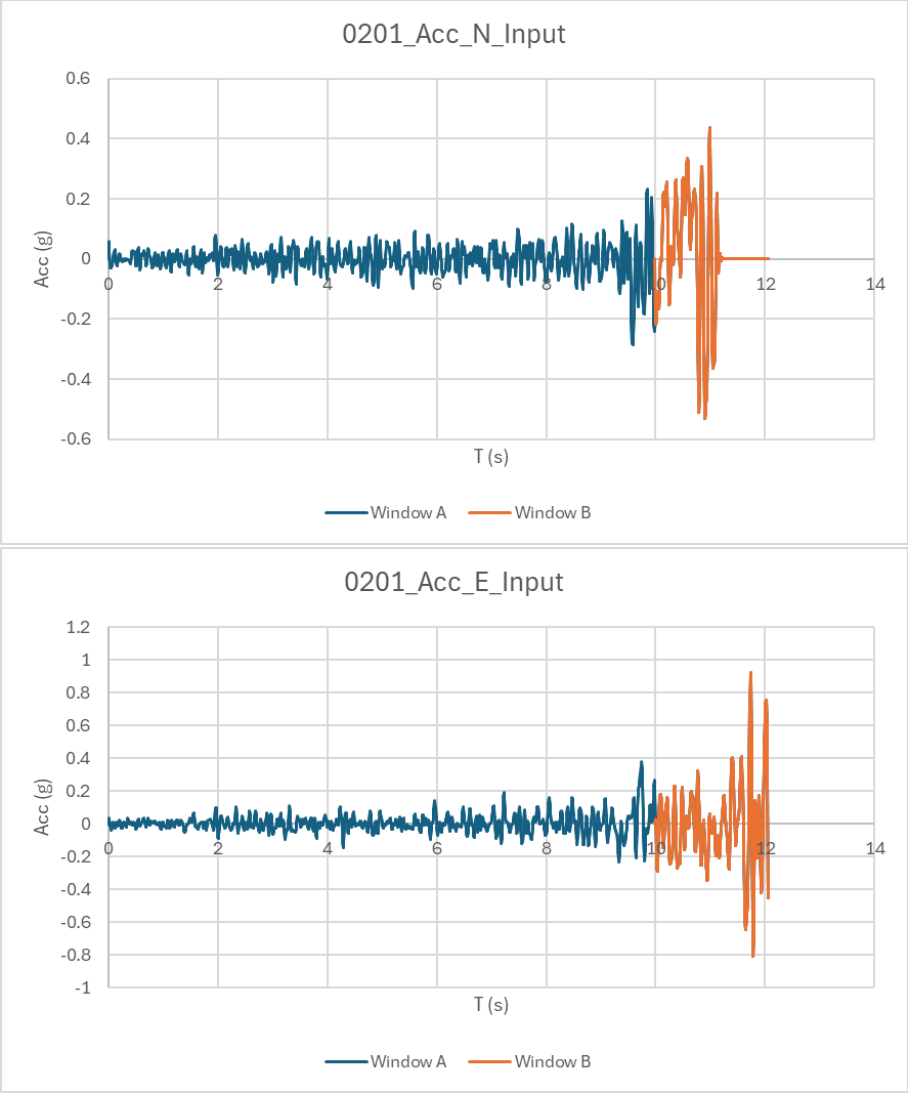

Figure 6-1 Ground motion input for Window A and Window B

Table 6-1 Summary of important analysis notes

Variables	Value	Notes
Time step	Δt = 0.01 s	Constant
Base excitation	Base acceleration in X and Y directions	Applied simultaneously

Window A	13.14 – 25.19 s (12.05 s)	Arias intensity ≥ 2%; full dynamic run
Window B	23.14 – 25.19 s (2.05 s)	Arias intensity ≥ 50%; short runs/impact analysis

Classical Rayleigh damping was adopted with a target damping ratio of $\zeta = 3\%$ around the dominant participation band identified in the eigenvalue study. A damping ratio of 3% is commonly used in nonlinear dynamic analyses of unreinforced masonry, as it limits unrealistic over-damping while approximating observed decay near the first mode (Betti & Vignoli, 2011). Using the minaret-excluded model (analysis model for dynamics) with $\omega_1 = 29.412$ rad/s (4.681 Hz) and $\omega_2 = 74.519$ rad/s (11.860 Hz) yields $\alpha = 1.265\ s^{-1}$ and $\beta = 5.773 \times 10^{-4}$ s. These coefficients restrict excessive damping of long-period content while maintaining realistic decay in the higher frequency range. A sensitivity checks against the full model (including the minaret) produced nearly identical coefficients (see Appendix B). Section 6.6 confirms that key peaks and drifts are not artefacts of the chosen ζ.

6.2. Input Base Acceleration and Response

The dynamic runs prescribe the recorded motion as uniform base accelerations in the X and Y directions (Section 6.1). Figure 6-2 and Figure 6-3 compare, for each axis, the imposed input (solid line) and the recorded base response at the supports (dashed line). The traces are visually coincident in amplitude and phase throughout the window, as expected when support motion is kinematically imposed. Minor pixel-level offsets arise from output sampling rather than physical effects. This comparison is a critical verification step, as it confirms that the applied input is faithfully transmitted to the model without numerical distortion. Establishing this consistency ensures that subsequent structural responses can be attributed to the dynamic characteristics of the mosque rather than artefacts of input application.

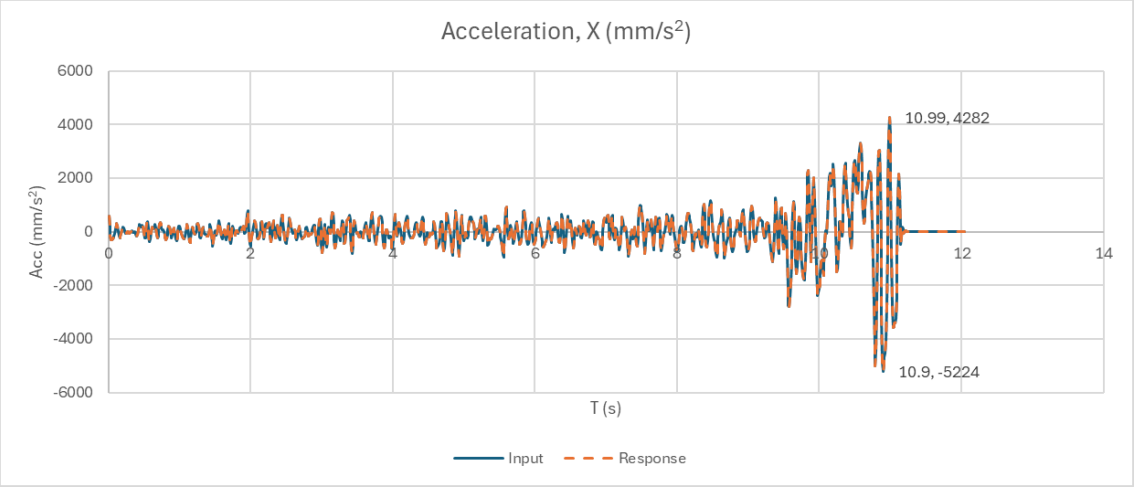

Figure 6-2 Base acceleration in X, showing imposed input is reproduced at supports without distortion.

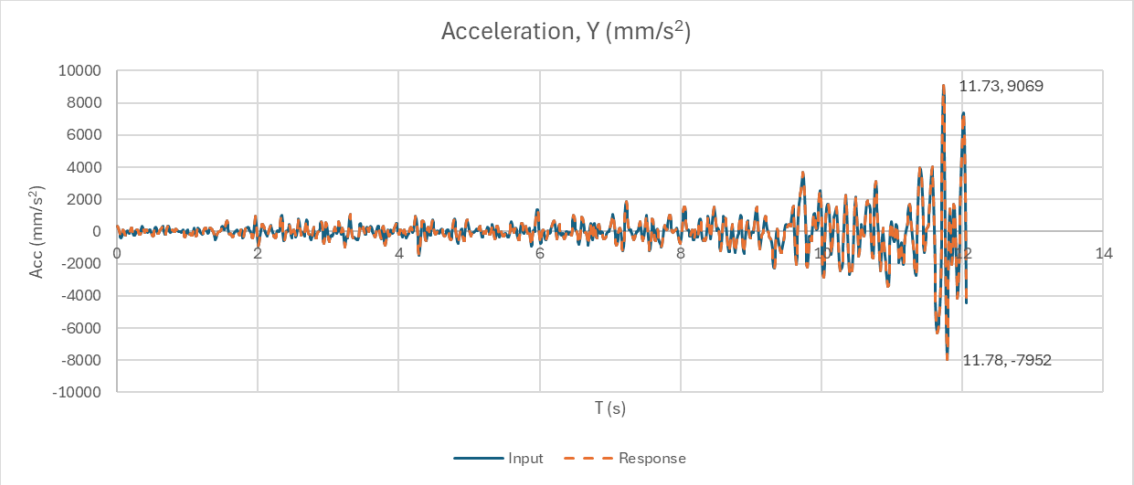

Figure 6-3 Base acceleration in Y, confirming accurate transmission of input record at supports.

The largest pulses occur in the final ~2 s of each axis, consistent with the intensity framing in Section 6.1. Their accurate reproduction at the base confirms that the imposed acceleration window and scaling procedure preserve both amplitude and phase characteristics of the selected record. After the cut-off, the response returns to zero, confirming no residual drift or integration bias in the baseline-corrected inputs.

Table 6-2 summarises the peak values and timestamps at the base. Both axes reproduce the maximum input accelerations with negligible differences (<0.05%), and the peak timings are coincident to within plotting tolerance. The near-identical amplitudes and timings confirm the accuracy of baseline correction and numerical time integration, demonstrating that the simulation framework is stable. This provides confidence that subsequent response quantities, including drifts, base reactions, and strain distribution, can be evaluated without bias from the input application stage.

Table 6-2 Peak base accelerations and times (input vs. response) in X and Y, confirming input–response agreement within plotting tolerance.

Axis	Peak Input	Peak Response
X	4282.13 mm/s2	4282 mm/s2
	10.99 s	10.99 s
	-5224 mm/s2	-5224 mm/s2
	10.9 s	10.9 s
Y	9069.41 mm/s2	9069 mm/s2
	11.73 s	11.73 s
	-7952.25 mm/s2	-7952 mm/s2
	11.78 s	11.78 s

6.3. Base Reaction vs Time

The summed base reactions in X and Y (Figure 6-4 and Figure 6-5) show pronounced pulses in the late stage of the record, coinciding with the window of maximum Arias intensity. Peak values occur at 10.94 s in the X direction (min −8,370 kN, max +15,000 kN) and at 11.69–12.03 s in the Y direction (min −11,200 kN, max +11,300 kN).

The horizontal dashed lines mark the pushover plateaus interpreted in Chapter 5 as monotonic strength limits. The plateaus are plotted with their respective signs but are read in absolute terms as direction-specific reference capacities.

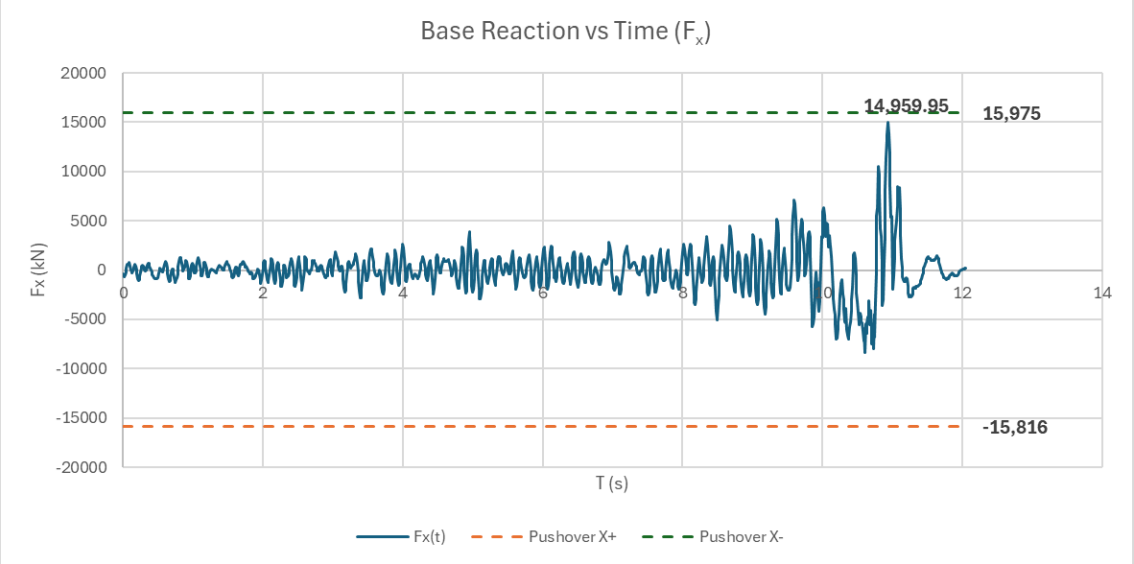

Figure 6-4 Base Reaction on X-axis (Fx), Compared to Pushover Result

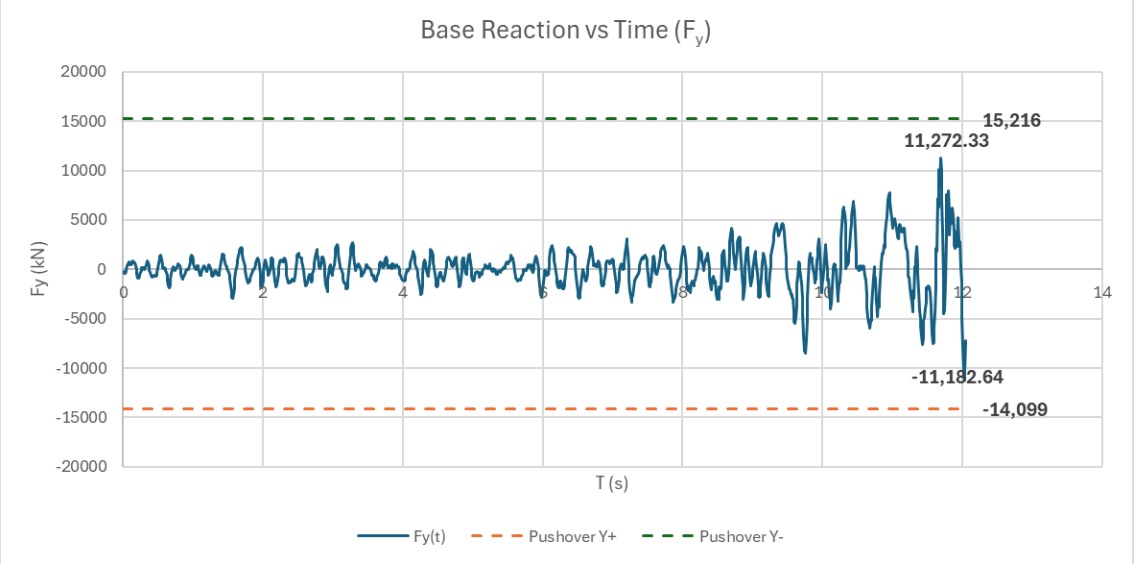

Figure 6-5 Base Reaction on Y-axis (Fy), Compared to Pushover Result

The largest absolute base reactions remain within the monotonic pushover plateaus in both axes. In X, the peak reaches about 94% of the positive plateau, with a smaller negative peak. In Y, the largest absolute peaks are about 80% of the plateaus. Therefore, the strong-motion record did not exceed the static global strength from pushover. The damage evidenced by the

drift and strain results should be read because of redistribution, cyclic degradation, and out-of-plane response, rather than exceedance of global base-shear capacity.

These findings are consistent with previous work on nonlinear dynamic assessment of masonry, which highlights that time-history demands often remain within monotonic strength envelopes when damping is realistically represented (Betti & Vignoli, 2011; D'Altri et al., 2020). The results therefore provide a robust baseline for subsequent shortened-window and impact-loading analyses.

6.4. Control-Point Drifts

Figure 6-6 to Figure 6-9 present the displacement and drift histories of the five selected control points, located at the tips of the four main walls and the crown of the dome. These positions allow both in-plane and out-of-plane behaviour to be tracked. Displacements are reported in millimetres, while drifts are normalised by the building height (H = 11.15 m).

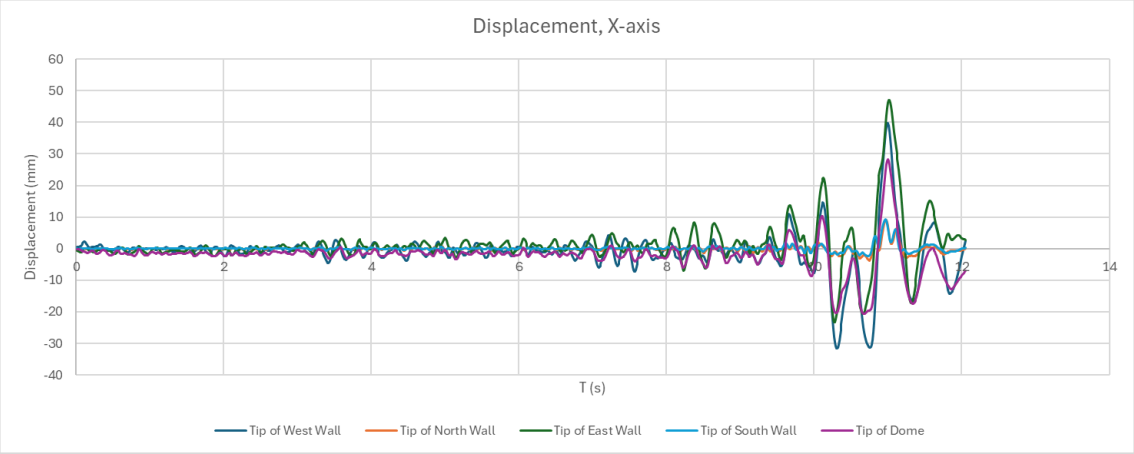

Figure 6-6 Displacement of Control Points Over Time, X-axis

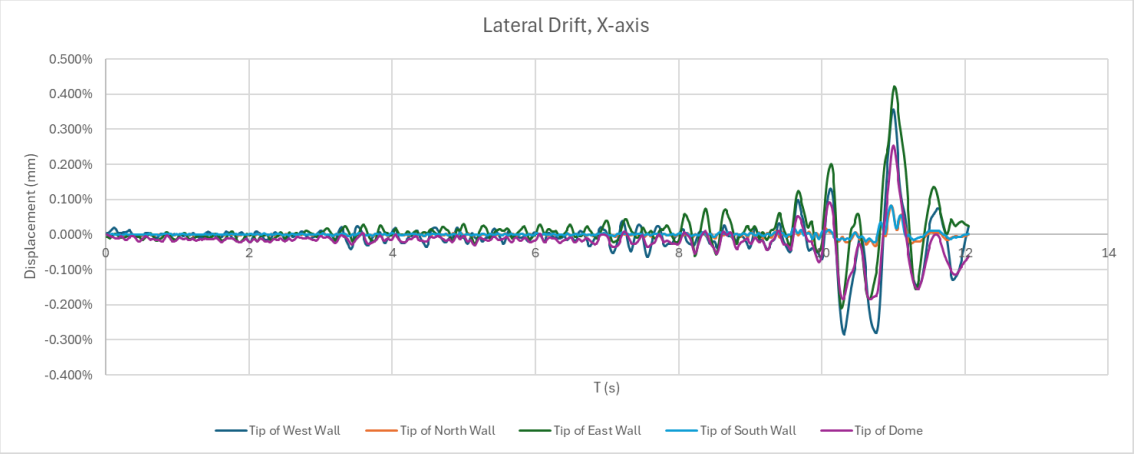

Figure 6-7 Lateral Drift of Control Points Over Time, X-axis

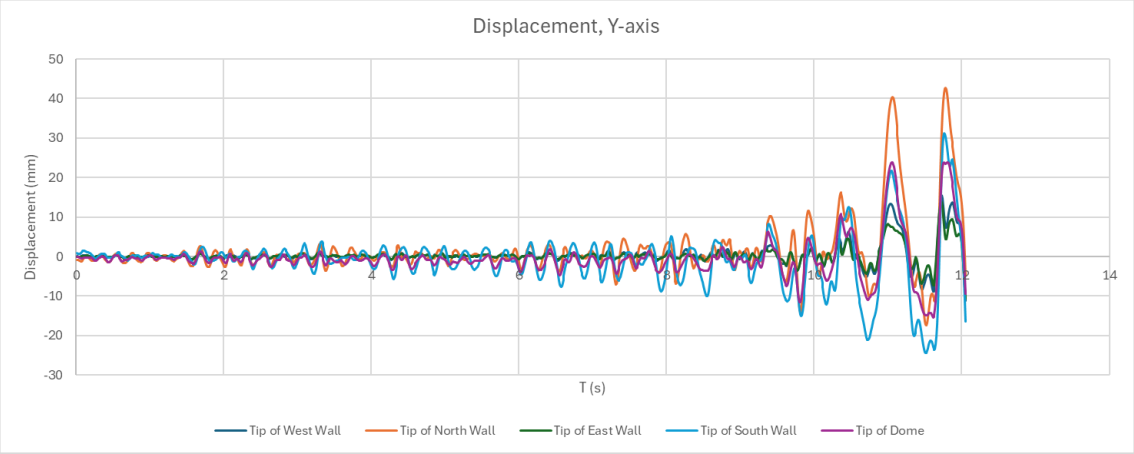

Figure 6-8 Displacement of Control Points Over Time, Y-axis

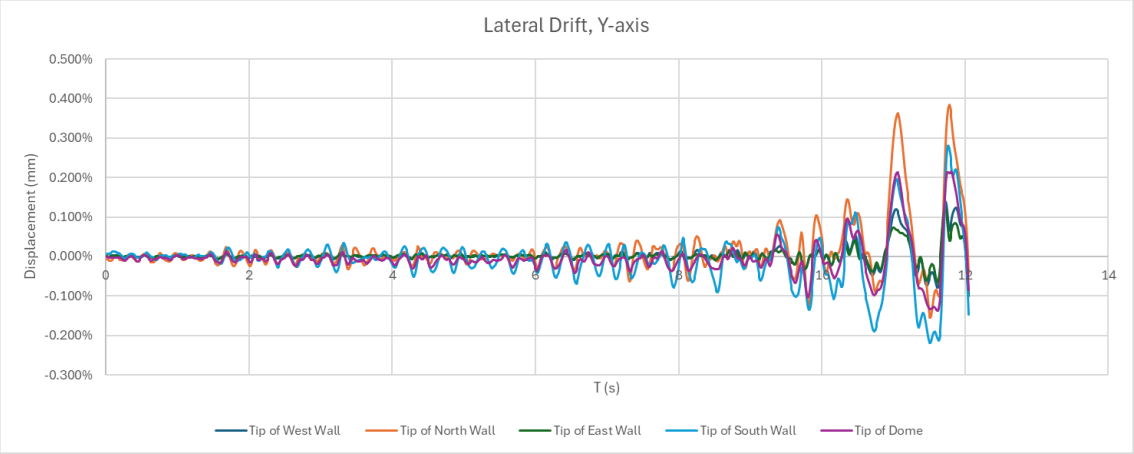

Figure 6-9 Lateral Drift of Control Points Over Time, Y-axis

The time histories show that the strongest pulses occur during the interval 10.9–11.8 s, coinciding with the peaks identified in the base reaction traces. At these instants, maximum displacements reach approximately 40–47 mm in the X direction (East and West walls) and up to 43 mm in the Y direction (North wall). When expressed as drift, these translate to about 0.35–0.42 % in the X direction and 0.38 % in the Y direction, as summarised in Table 6-3.

Table 6-3 Peak displacement and drift at control points

No	Control Points	Max Disp. X (mm)	Max Drift X	Max Disp. Y (mm)	Max Drift y
1	Tip of West Wall	39.72	0.356%	15.53	0.139%
2	Tip of North Wall	9.16	0.082%	42.76	0.383%
3	Tip of East Wall	46.98	0.421%	13.95	0.125%
4	Tip of South Wall	9.19	0.082%	31.24	0.280%
5	Tip of Dome	28.18	0.253%	23.90	0.214%

Although these values remain below the often-cited 1 % drift threshold for significant damage in unreinforced masonry (FEMA 356; ASCE 41; Lagomarsino & Cattari, 2015), they represent an important range where cracking, sliding, and loss of box behaviour are expected to emerge.

The correspondence with known fragility ranges confirms that the modelled structure is approaching the onset of severe cyclic degradation.

The distribution of displacements reveals two distinct regimes:

- Coherent motion up to ~0.1 % drift: all control points move in phase, consistent with global box-type behaviour.
- Differentiated response beyond ~0.1 % drift: out-of-plane wall tips (East in X, North and South in Y) register larger displacements, while in-plane tips remain more restrained. This transition indicates a shift from global box behaviour to local panel behaviour, with wall tips progressively decoupling as cyclic pulses intensify.

This shift is particularly important for historic masonry: once box behaviour is compromised, stability relies on post-yield reserves and on the ability of individual panels to resist out-of-plane overturning, both of which are vulnerable to degradation under strong cyclic demand (Magenes & Calvi, 1997).

Overall, the relative distribution of displacements confirms the pushover analysis in Chapter 5, which identified wall tips as the governing elements for each direction. The dynamic results complement this by demonstrating how those mechanisms evolve over time: from coherent global resistance to a more localised and unstable regime.

The hysteresis curves in Figure 6-10 and Figure 6-11 provides further insight. Four distinct phases can be recognised, linked to features of the ground-motion record (Arias intensity in Figure 3-22:

- **0–8 s:** compact, narrow loops with little hysteretic dissipation, reflecting elastic behaviour.
- **8–10.5 s:** widening loops, signalling the onset of cracking and frictional sliding, though overall stiffness is largely maintained.
- **10.5–11.9 s:** dominant cycles, with markedly broadened loops and clear stiffness degradation. Loop extents remain broadly consistent with (and in places slightly below) the monotonic pushover plateaus.
- **11.9–12.05 s:** residual loops with minor offsets from the origin, indicating transient unrecoverable deformation and pinching effects due to sliding and joint opening. The small residual drift (–0.094% in the Y-direction) suggests some permanent deformation, but not a complete loss of box behaviour.

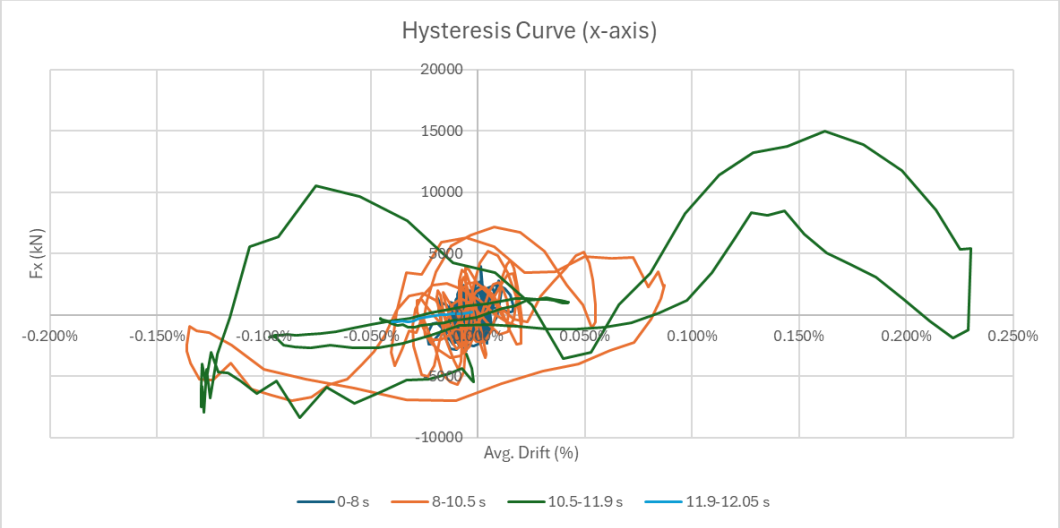

Figure 6-10 Hysteresis Curve, X-axis

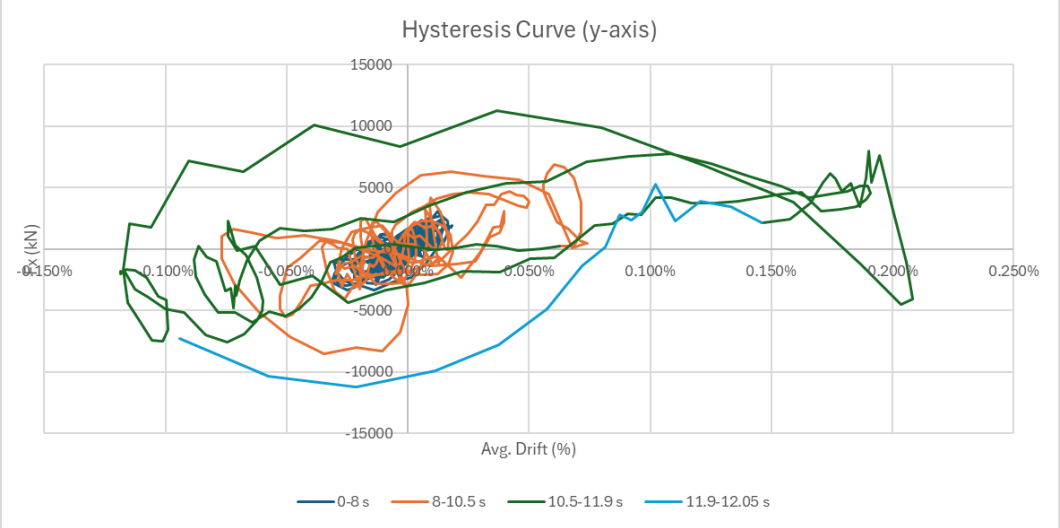

Figure 6-11 Hysteresis Curve, Y-axis

Physically, this progression implies that the mosque initially resisted elastically, then engaged local cracking during the build-up, before entering a regime of significant cyclic degradation during the main pulse. As the pushover envelope was approached and locally engaged, additional mechanisms such as out-of-plane flexural rotation and torsional coupling were activated. The persistence of residual loops in the tail phase shows that, even after input motion subsided, the structure retained unrecoverable displacements and experienced reduced stiffness.

Comparison with pushover findings is instructive. While absolute drift values are below the monotonic capacity (~1 %), the hysteresis loops show near-threshold cyclic demand with notable degradation. Peak base reactions remain within the pushover plateaus; exceedance of global base-shear capacity is therefore not indicated. The key point is reliance on post-yield reserves and cyclic degradation mechanisms that static checks do not capture. For historic masonry, once cracking accumulates and box behaviour is weakened, stability against further shaking or neighbour interaction is significantly undermined.

6.5. Strain Pattern Comparison

Figure 6-12 to Figure 6-14 present the global distribution of tensile strains at t = 10.99 s, a stage selected deliberately because results were recorded at every 10-time steps in DIANA for practicality. While this snapshot does not coincide exactly with the time of peak global displacements (11.01 s), the interval is sufficiently close that the strain field remains representative of the governing mechanisms.

The top-view and isometric plots illustrate that the building undergoes a combined response resembling pushover X+ and Y+ simultaneously. Each wall exhibits both in-plane and out-of-plane deformation, albeit to different degrees, with the east wall emerging as the most critical in terms of global deformation demand. This pattern indicates a breakdown of box behaviour, where orthogonal walls no longer act as a unified system but instead deform independently under the compounded excitation (Lourenço et al., 2011; Betti & Vignoli, 2011; D'Altri et al., 2020).

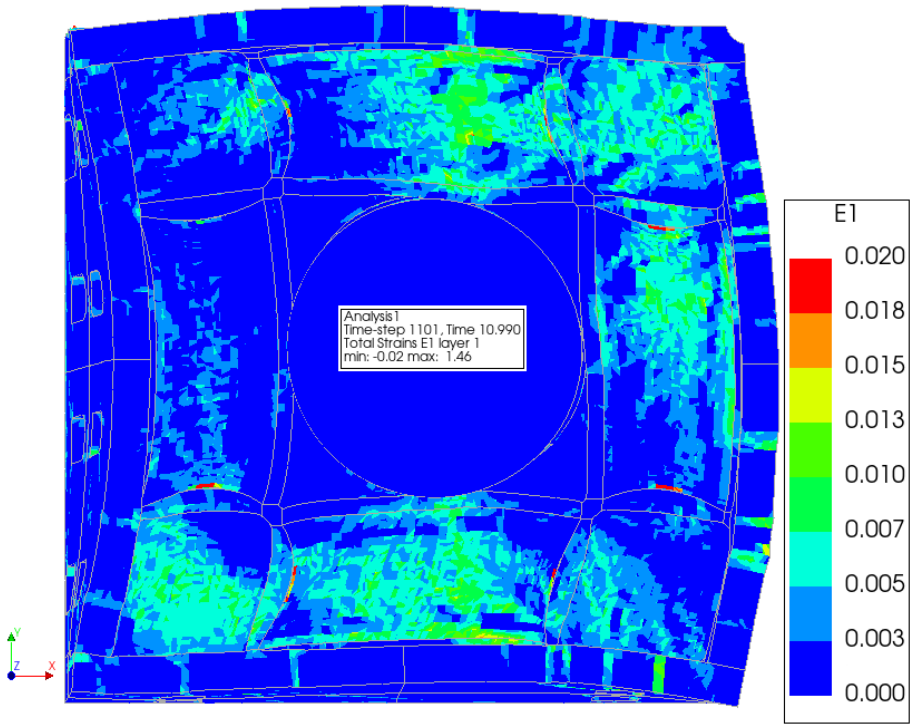

Figure 6-12 Top View of the Mosque's Strain Pattern during Time Step 10.99s

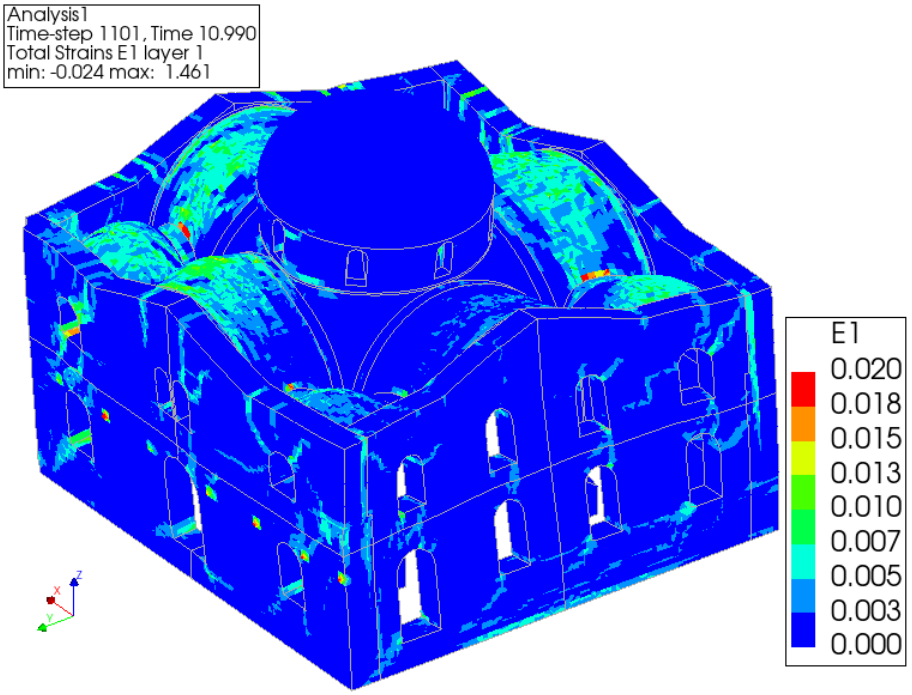

Figure 6-13 Isometric View Showcasing Strain Pattern on North and West Walls

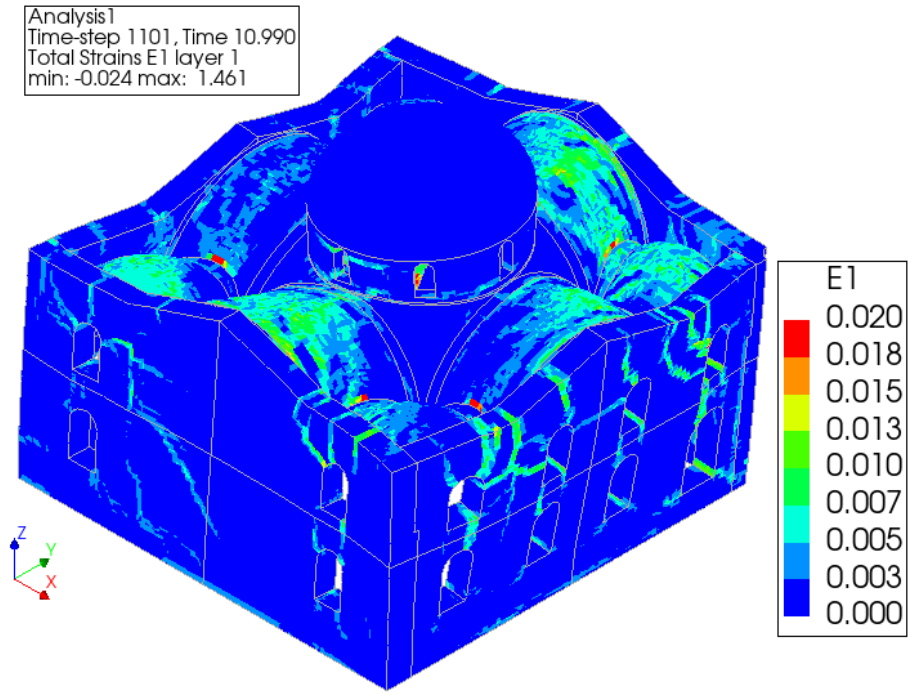

Figure 6-14 Isometric View Showcasing Strain Pattern on South and East Walls

From a physical standpoint, the observed strain fields show:

- Horizontal bands forming along opening levels, consistent with hinge lines from pushover results.
- Vertical cracks near wall edges, enabling out-of-plane flexural rotations.
- Strain concentrations at the arch–dome interfaces, highlighting stress transfer inefficiencies once diaphragm action weakens.

Together, these features demonstrate that the mosque mobilises both first-mode pushover mechanisms and higher-mode local failures when subjected to strong cyclic pulses. The dynamic analysis therefore reinforces and extends the pushover findings, showing that mechanisms identified under monotonic loading do indeed emerge under seismic excitation, but in more complex, coupled forms.

The subsequent subsections (6.5.1–6.5.4) discuss each wall separately, contrasting their dynamic strain patterns with the corresponding pushover envelopes, to trace how local damage modes interact within the global response.

6.5.1. East Wall

Figure 6-16 present the East Wall crack distribution at two successive timesteps bracketing the global deformation peak (10.99 s and 11.09 s). Both snapshots show diagonal tensile strain bands linking window openings with the upper wall segments and arch bases. The comparison between the two steps highlights cyclic opening and redistribution, with new cracking superimposed on previously activated regions.

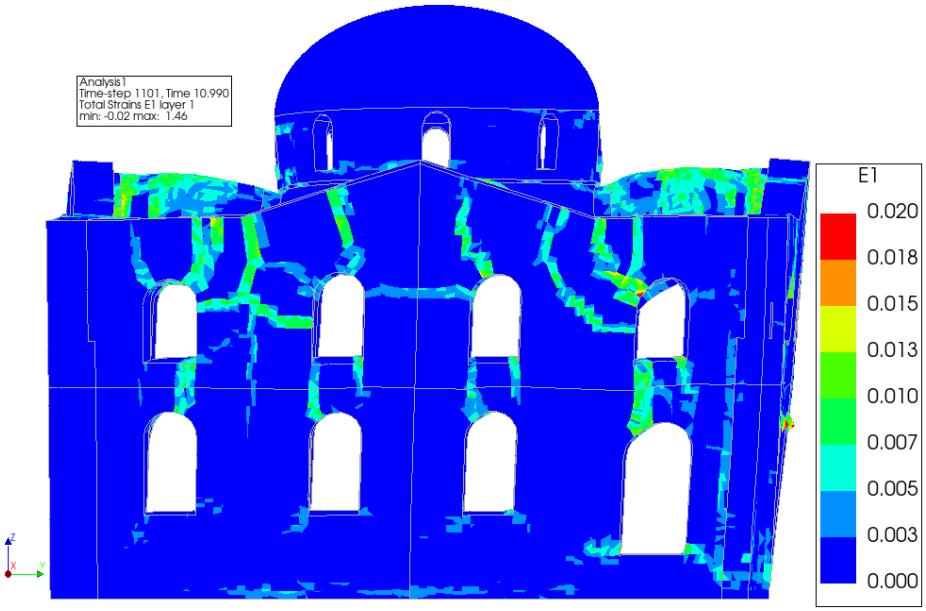

Figure 6-15 Smeared Crack Pattern on East Wall Before Max Global Deformation Occur (Time Step 10.99s)

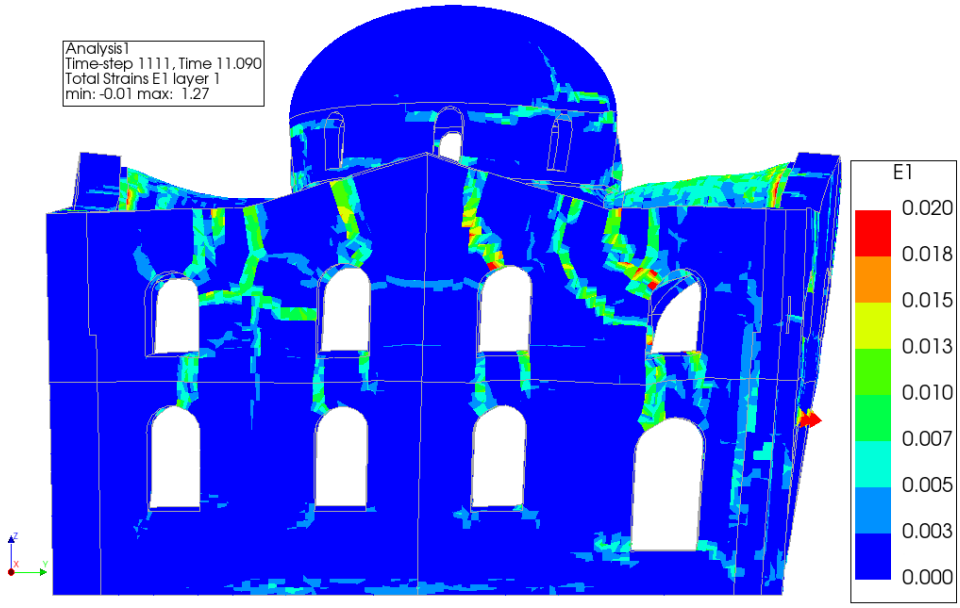

Figure 6-16 Smeared Crack Pattern on East Wall After Max Global Deformation Occur (Time Step 11.09)

When compared with the pushover results, the correlation is evident. Under X+ pushover loading, the East Wall exhibits pronounced out-of-plane deformation, particularly around the upper wall connections. Under Y+ pushover, the wall develops additional in-plane diagonal bands along the window alignments. The dynamic pattern represents a hybrid of these behaviours: out-of-plane bending consistent with the X+ pushover, together with diagonal shear consistent with the Y+. This explains why the East Wall reached the largest X-direction displacements (Table 6-3) while still accumulating diagonal cracking in the Y direction.

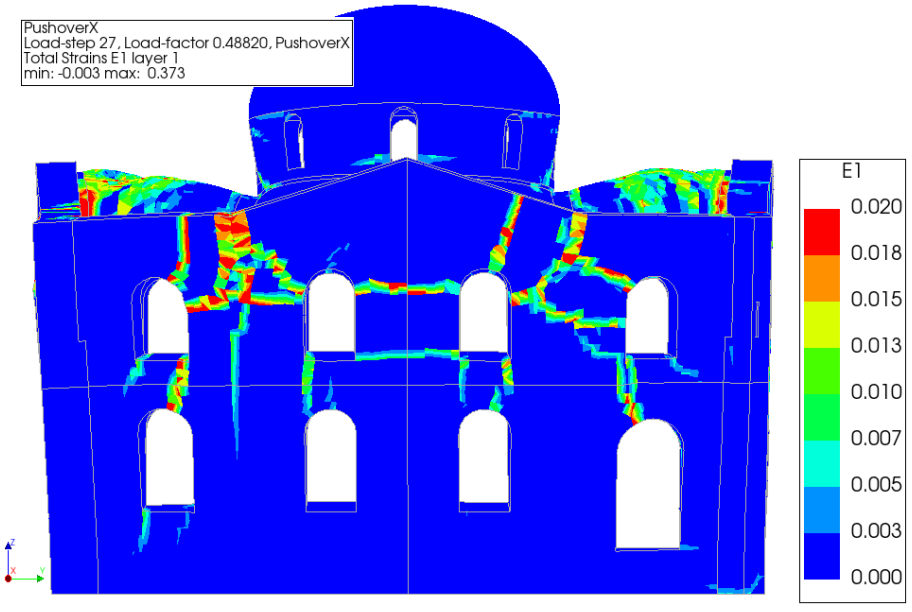

Figure 6-17 Smeared Crack Pattern on East Wall Under Pushover X+ (out-of-plane) Analysis

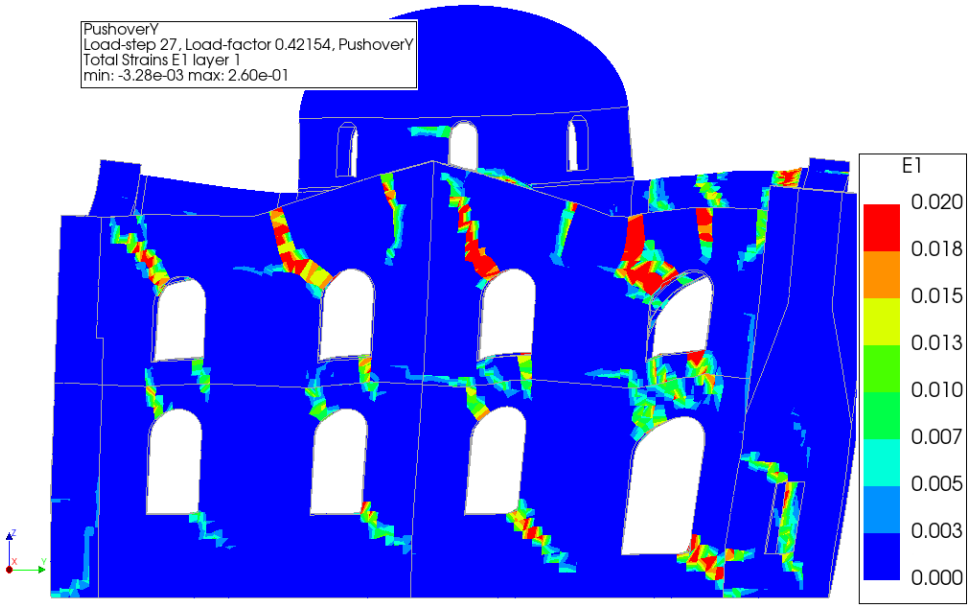

Figure 6-18 Smeared Crack Pattern on East Wall Under Pushover Y+ (in-plane) Analysis

Physically, the East Wall reflects the absent box behaviour once the structure is pushed out of the elastic region. Rather than moving coherently with the adjacent walls, it undergoes amplified deformation governed by both bending out of the plane and in-plane shear. This hybrid mechanism shows how torsional coupling and asymmetric stiffness redistribution led to walls responding differently under the same dynamic pulse.

These findings are consistent with prior nonlinear dynamic masonry studies, which reported combined in-plane and out-of-plane damage modes under strong ground motion when torsional participation is significant (Betti & Vignoli, 2011; D'Altri et al., 2020). Within this case study, the East Wall is therefore the clearest expression of coupled deformation mechanisms.

6.5.2. West Wall

Figure 6-19 and Figure 6-20 presents the West Wall strain distribution at two successive timesteps bracketing the global deformation peak (10.99 s and 11.09 s). Both images show diagonal tensile cracks forming across window alignments and intensifying around the window bands and roof junctions. The shift from the first to the second snapshot illustrates cyclic re-opening of existing cracks and extension into neighbouring regions, especially at the upper corners and arch interfaces.

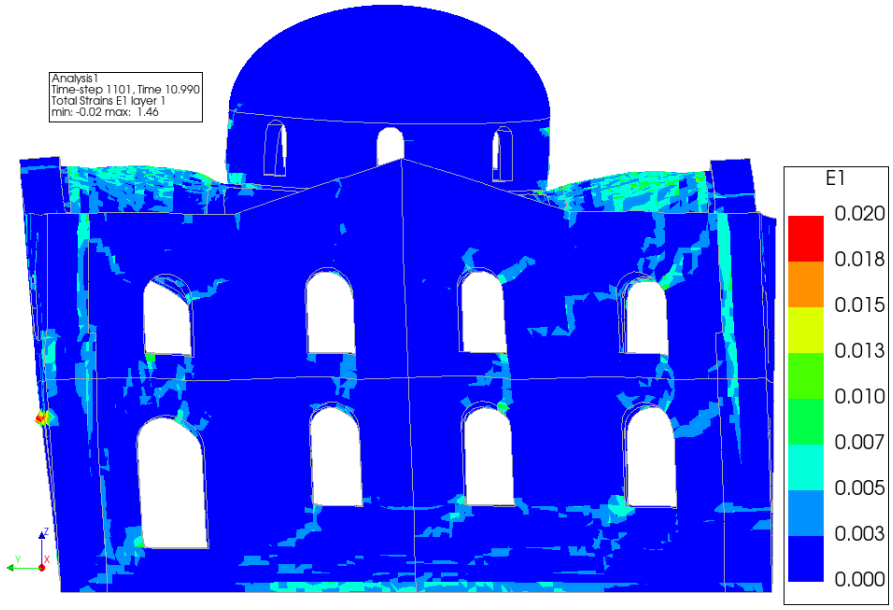

Figure 6-19 Smeared Crack Pattern on West Wall Before Max Global Deformation Occur (Time Step 10.99s)

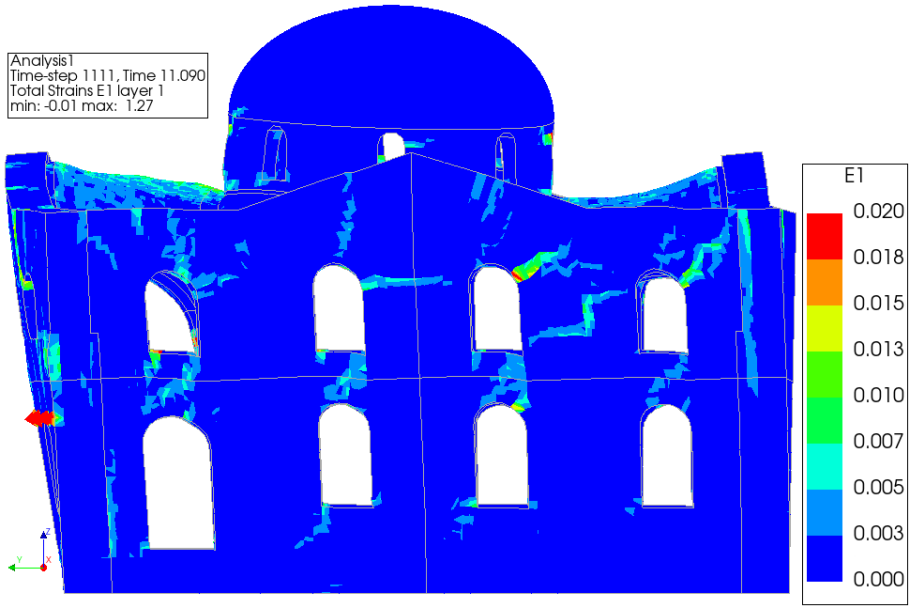

Figure 6-20 Smeared Crack Pattern on East Wall After Max Global Deformation Occur (Time Step 11.09s)

When compared with pushover responses, the correlation is again evident. Under X+ pushover, the West Wall experiences noticeable out-of-plane flexure across the façade, with horizontal bands concentrated at the wall–roof junction. Under Y+ pushover, diagonal crack bands emerge along the window zones and arch edges. The dynamic response combines these two mechanisms: out-of-plane deformation driven by X-direction excitation, superimposed with diagonal shear bands consistent with Y-direction response. This hybrid mechanism explains why the West Wall registered sizeable displacements in both axes (Table 6-3), even though it did not reach the maxima observed at the East and North walls.

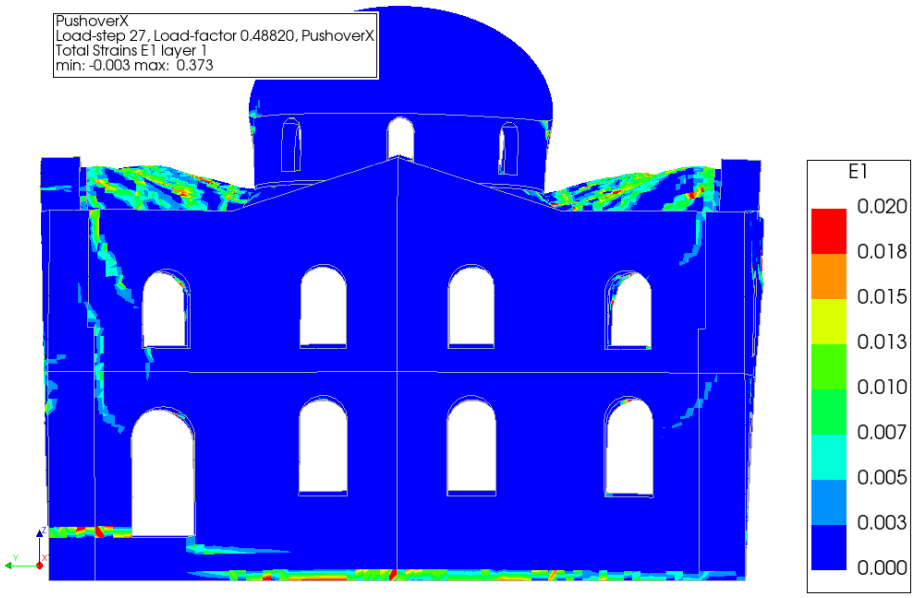

Figure 6-21 Smeared Crack Pattern on West Wall Under Pushover X+ (out-of-plane) Analysis

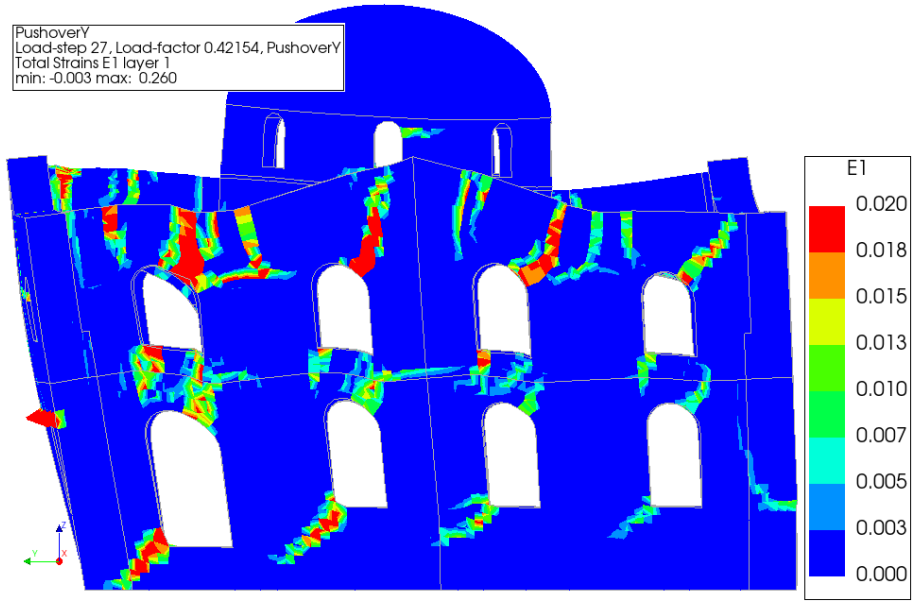

Figure 6-22 Smeared Crack Pattern on East Wall Under Pushover Y+ (in-plane) Analysis

Physically, the West Wall again reflects the absent box behaviour once the structure is pushed beyond elastic limits. Instead of moving in phase with the other façades, it exhibits torsional participation, with strain localisation at the wall–roof interface and diagonal shear through the openings. This combination points to redistribution of stiffness under dynamic loading, where the West Wall acts as a tension-demanded façade while the adjacent walls undergo relatively less cracking.

These findings are consistent with prior nonlinear masonry simulations, which show that coupled in-plane and out-of-plane cracking, amplified by torsion, can dominate the response of façades aligned with the input direction (Betti & Vignoli, 2011; D'Altri et al., 2020). In this case, the West Wall illustrates a transitional behaviour: while not hosting the largest absolute drifts, it plays a key role in accommodating torsional distortion and sustaining redistributed tensile demand during the strong-motion pulse.

6.5.3. North Wall

Figure 6-23 and Figure 6-24 show the North Wall crack distribution at 10.99 s and 11.09 s, bracketing the global deformation peak. The dynamic response is characterised by diagonal tensile cracks emerging across the wall panels, with particular concentration around the window bands and upper wall–roof junctions. The two snapshots highlight incremental widening of the cracks and redistribution of strain intensity, consistent with cyclic opening–closing behaviour.

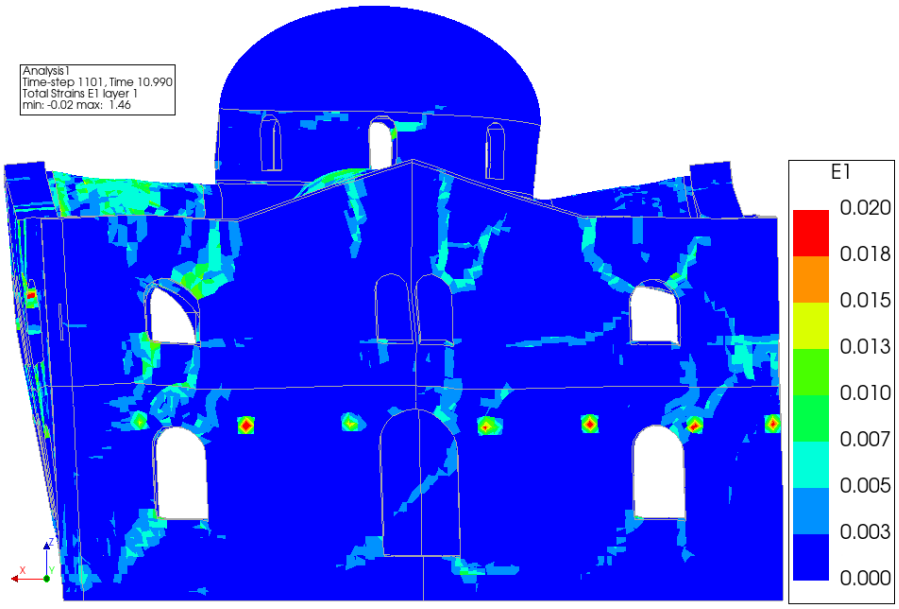

Figure 6-23 Smeared Crack Pattern on North Wall Before Max Global Deformation Occur (Time Step 10.99s)

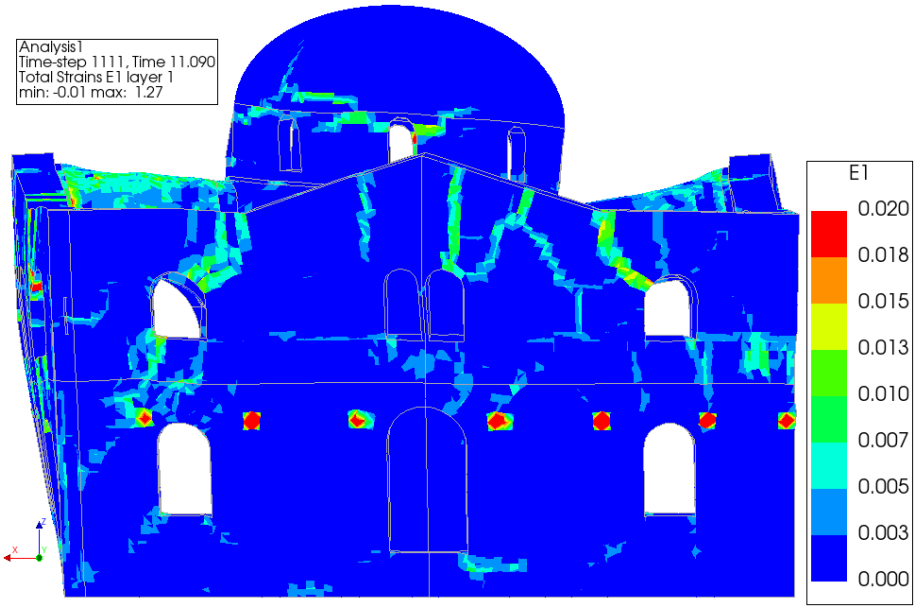

Figure 6-24 Smeared Crack Pattern on North Wall After Max Global Deformation Occur (Time Step 11.09s)

To interpret the physical mechanisms, Figure 6-25 and Figure 6-26 compare the dynamic pattern with the pushover envelopes. Under X+ pushover, the North Wall develops vertical

bending cracks at the corners and diagonal cracks spanning window openings. Under Y+ pushover, the wall exhibits diagonal bands cutting through the window lines, together with flexural cracks at the top. The dynamic snapshots reflect a combination of these two behaviours: out-of-plane deformation consistent with X+ pushover, superimposed with diagonal shear bands typical of Y+ pushover.

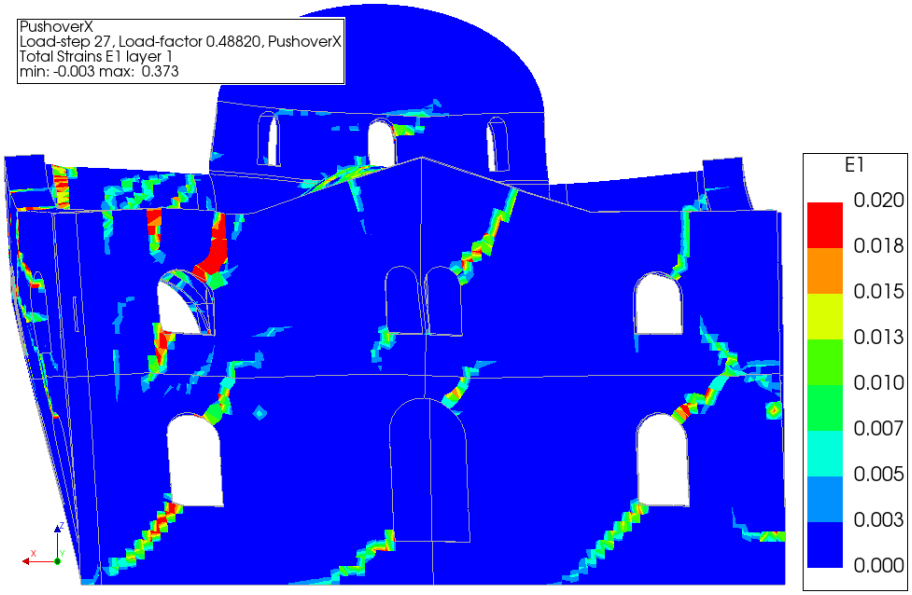

Figure 6-25 Smeared Crack Pattern on North Wall Under Pushover X+ (in-plane) Analysis

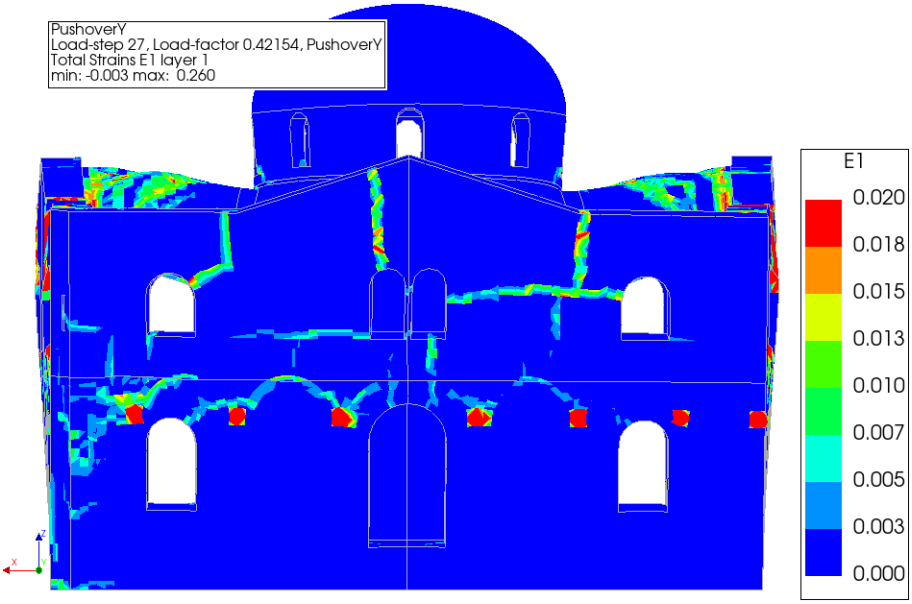

Figure 6-26 Smeared Crack Pattern on North Wall Under Pushover Y+ (out-of-plane) Analysis

Physically, the North Wall illustrates how the structure departs from coherent box response once cyclic pulses dominate. While initially aligned with pushover predictions, the dynamic behaviour shows torsional coupling and asymmetric redistribution of stiffness. The wall attracts significant diagonal cracking in the Y direction while simultaneously exhibiting bending-type cracks in the X direction. This dual response aligns with reported findings in nonlinear masonry dynamics, where strong ground motion often activates mixed in-plane and out-of-plane modes (Betti & Vignoli, 2011; D'Altri et al., 2020).

The North Wall exhibits a combined response under dynamic loading, with crack localisation reflecting both X+ and Y+ pushover patterns. Out-of-plane bending is most pronounced at the corners and upper wall–roof junctions, while diagonal shear bands form across window zones in line with Y+ pushover. Compared with pushover envelopes, the dynamic response demonstrates asymmetric redistribution of stiffness and minor torsional participation, confirming that the wall partially contributes to the overall global behaviour but shows independent deformation once the structure is pushed beyond the elastic range. These results reinforce the utility of pushover analysis for mechanism identification while illustrating the nuanced redistribution and cyclic effects captured by the time-history simulation.

6.5.4. South Wall

Figure 6-27 and Figure 6-28 present the South Wall crack distribution at two successive timesteps bracketing the global deformation peak (10.99 s and 11.09 s). Both snapshots highlight strain localisation concentrated above window crowns and along the roof–wall junctions. The first snapshot shows early diagonal bands linking the openings with the mid-wall window lines, while the second reveals widening and extension of these cracks into continuous horizontal hinges across the façade.

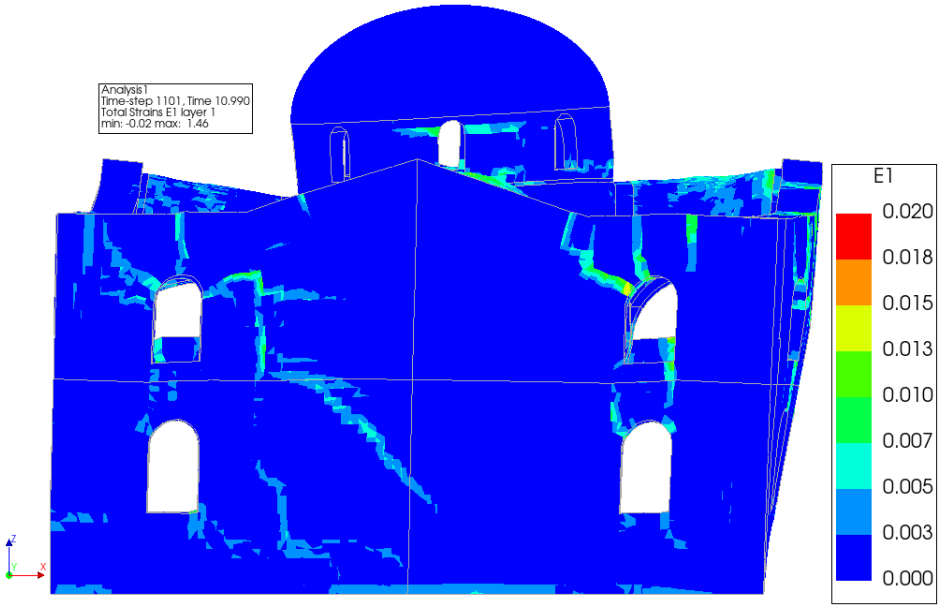

Figure 6-27 Smeared Crack Pattern on South Wall Before Max Global Deformation Occur (Time Step 10.99s)

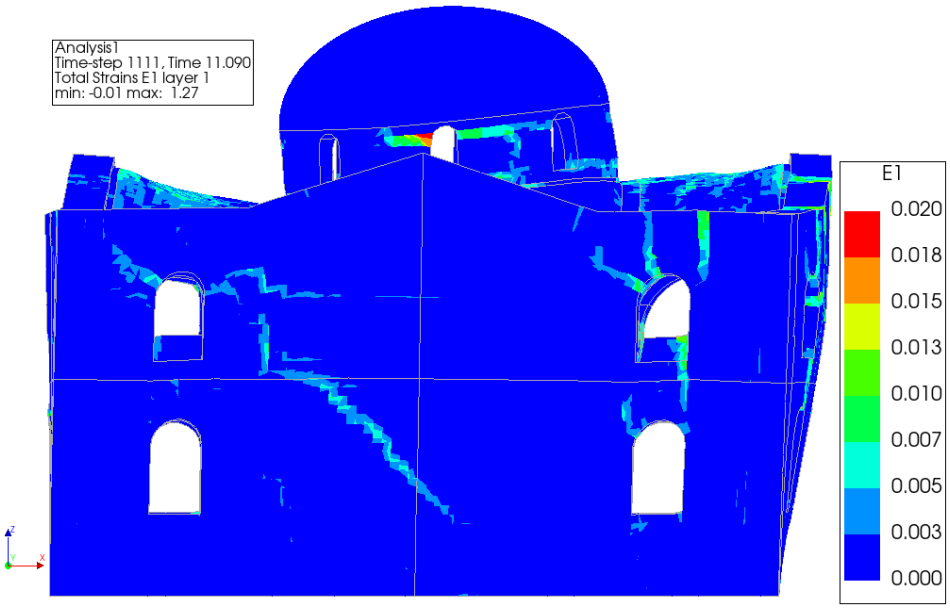

Figure 6-28 Smeared Crack Pattern on South Wall After Max Global Deformation Occur (Time Step 11.09s)

When compared with pushover envelopes, the correlation is again evident. Under X+ pushover (Figure 6-29), the South Wall exhibits out-of-plane flexural cracking concentrated near the upper window alignment. Under Y+ pushover (Figure 6-30), diagonal shear bands form between the window openings and spread towards the roof interface. The dynamic response represents a combination of these mechanisms: cyclic out-of-plane bending consistent with X+ pushover, overlaid with diagonal shear pathways typical of Y+ pushover.

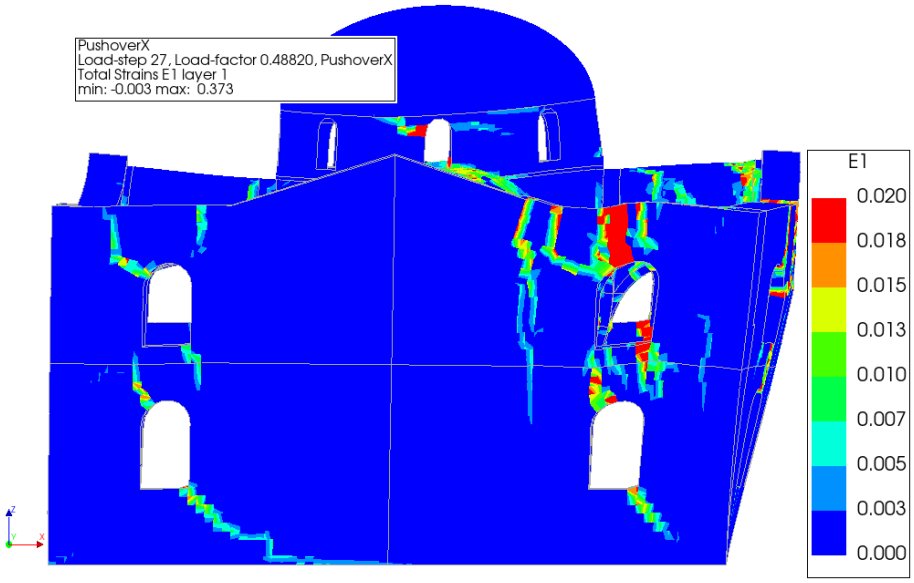

Figure 6-29 Smeared Crack Pattern on South Wall Under Pushover X+ (in-plane) Analysis

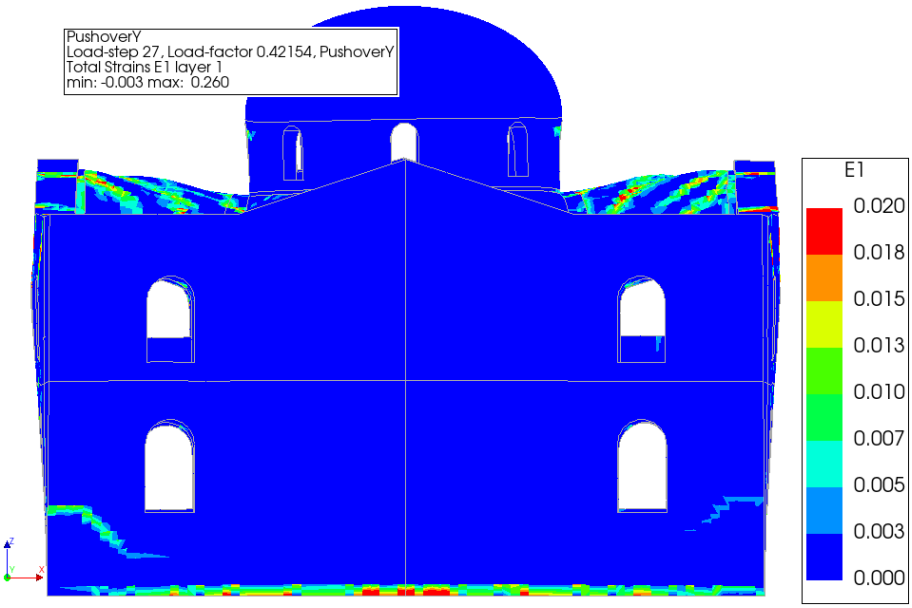

Figure 6-30 Smeared Crack Pattern on South Wall Under Pushover Y+ (out-of-plane) Analysis

Physically, the South Wall illustrates a two-level cracking mechanism. Horizontal strains develop both at the upper window bands and at the roof–gable interface, connected by vertical splitting beside the openings. This interaction produces four-hinge behaviour, enabling rotation of the upper wall panels and accelerating the out-of-plane response. In addition, stepped diagonal cracks highlight secondary shear participation, which weakens the residual stiffness of the façade.

These findings are consistent with prior nonlinear masonry dynamics research (Betti & Vignoli, 2011; D'Altri et al., 2020), showing that walls with multiple openings tend to combine out-of-plane bending with in-plane shear once box behaviour is lost. Within this case study, the South Wall therefore represents a façade highly vulnerable to seismic demand, in agreement with post-event field evidence of heavy cracking and partial failure.

6.5.5. Pillars and Arches

The interior strain plots below show principal tensile strain E1 at t = 10.99 s (just before the global response peak) and t = 11.09 s (just after). The primary 2×2 panel keeps the arches and vaults visible to preserve load-path context; the follow-up 1×2 pair crops to the columns only at 11.09 s to highlight column-head behaviour.

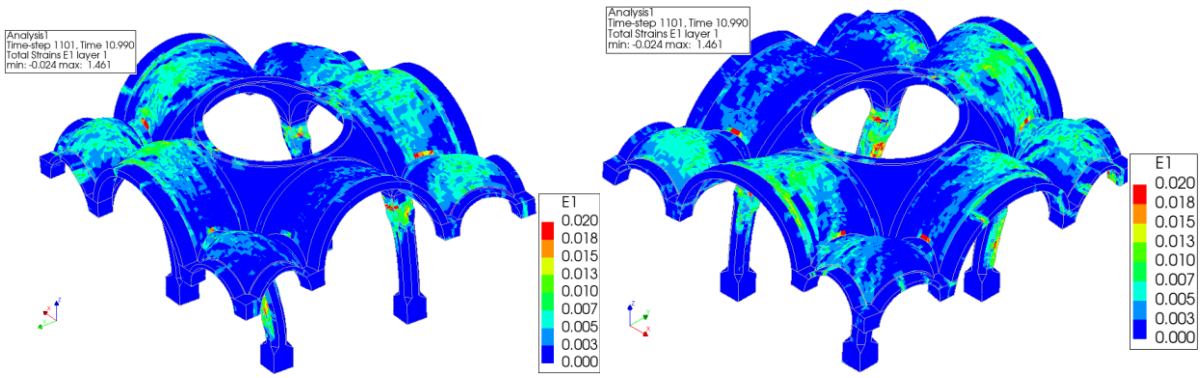

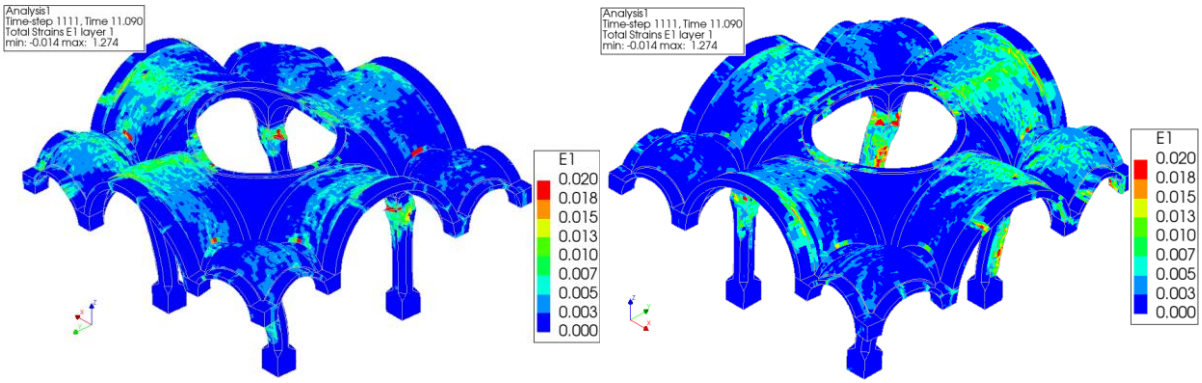

Figure 6-31 Interior E1 strain maps at t = 10.99 s and t = 11.09 s. Left pair: NW view (10.99 s above, 11.09 s below). Right pair: SE view (10.99 s above, 11.09 s below). Warmer colours indicate higher E1 (tension).

The four frames reveal a consistent pattern that complements the façade reads in Sections 6.5.1 to 6.5.4:

- Column–arch interfaces. Localised E1 concentrations occur at the tops of the interior columns where the arches start. These bands intensify from 10.99 s to 11.09 s, indicating cyclic opening at the column–arch interface.
- Arch ribs (haunch and crown zones). Diagonal E1 bands develop along the lower portions of the arch ribs (haunch regions) and at mid-span (crown/keystone). The bands are stronger in directions aligned with façades that show larger out-of-plane drifts, consistent with thrust redistribution once box behaviour weakens.
- Pendentives and drum seat. Short vertical splits and short bands appear at the transitions between the pendentives and the circular drum (drum seat), and at drum–roof/drum–wall junctions, matching the hinge tendencies noted at the dome–drum and roof–wall connections.
- Vault (underside/soffit). The underside of the vaults (intrados) shows diffuse, low-level E1 rather than continuous hinge lines, suggesting mainly membrane action with localised cracking; no interior mechanism dominates independently of the façades.
- Asymmetry and torsion. Comparing the NW and SE views shows mild asymmetry in band intensity, consistent with the torsional participation inferred from the façade results and hysteresis.
- Timing. From 10.99 s to 11.09 s the pattern mostly intensifies at existing hot spots rather than spreading to new regions, which matches the short strong-pulse window identified in the time histories.

These interior reads are therefore a visual confirmation of the load path already discussed: façade out-of-plane demand feeds the interior through the arches into the columns and drum supports. The images do not introduce a new failure mode and they remain compatible with the “repairable” qualitative interpretation adopted for the isolated run.

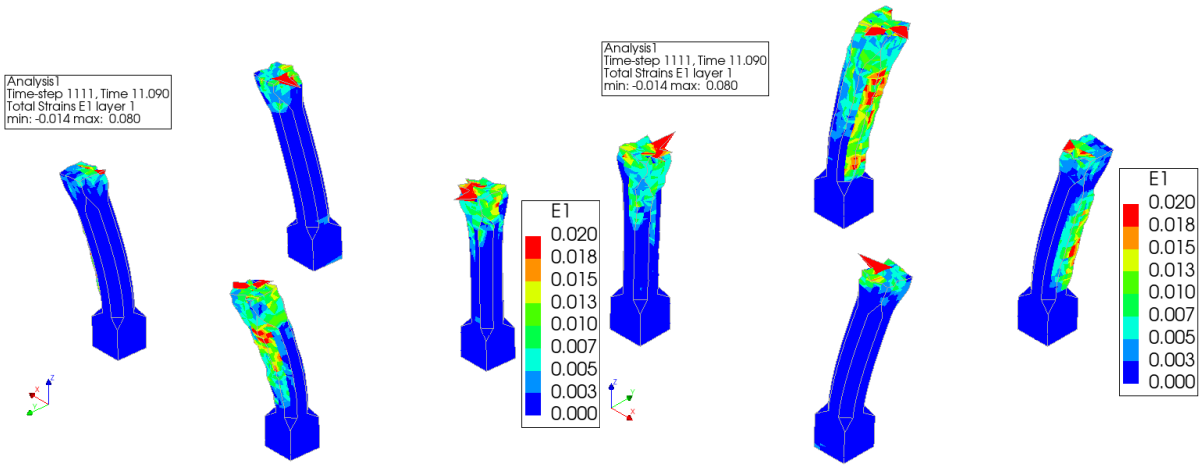

Figure 6-32 Columns only, E1 at t = 11.09 s. Left: NW view. Right: SE view. Concentration at capitals highlights bending demand transferred from the arches.

Figure 6-32 shows the principal tensile strain distribution at 11.09 s, and it is observed that:

- E1 concentrates at the column capitals and abaci, with short vertical streaks along the first segment of the shaft, indicating bending with tension on the interior faces.
- The pattern is stronger where adjacent façades attract larger out-of-plane drifts, supporting the link between façade demand and column-head action.
- No continuous column-height banding is observed; the hot spots are confined to the head region, which is consistent with transfer through the arches rather than a column-governed mechanism.

These interior views are supplementary. They reinforce that, under the isolated record, damage concentrates at openings, arches, and the dome–drum transition, with interior columns picking up bending at their heads as façade panels lose box restraint. The observations remain consistent with repairable interior states and do not alter the discussions of Section 6.6.

6.6. Discussion

The combined outcomes of the modal, pushover, and dynamic analyses provide a coherent picture of the seismic behaviour of the mosque and the mechanisms underlying its vulnerability. Across all methods, the findings converge on the same weaknesses: cracks at openings, hinge formation along windows, edge splitting, and torsional coupling once box behaviour is lost. This consistency reinforces the validity of the FE modelling approach, in line with established recommendations for mechanism-level interpretation of historic masonry (Lourenço, 2002; Betti & Vignoli, 2011).

The pushover simulations proved effective in identifying critical deformation modes under monotonic loading. They showed that horizontal cracks above openings and diagonal shear bands form under in-plane demand. The dynamic analysis extended these insights by demonstrating that under cyclic pulses these monotonic mechanisms are not isolated but act in coupled and evolving forms. For example, the East and North Walls combined out-of-plane flexure with diagonal shear (Figure 6-15 and Figure 6-23), while the West and South Walls

exhibited multi-level hinge mechanisms accentuated by torsional redistribution (Figure 6-19 and Figure 6-27). These findings align with prior nonlinear dynamic studies, which emphasise that mixed-mode responses are inevitable once cyclic demand interacts with asymmetric stiffness distribution (Betti & Vignoli, 2011; D'Altri et al., 2020).

Crucially, the analyses demonstrate the progressive breakdown of box behaviour. Rather than deforming as a coherent unit, the four façades acted increasingly independently, with loss of diaphragm restraint at arch and dome connections accelerating this process (Figure 6-12 to Figure 6-14). Similar observations have been reported in post-earthquake surveys of historic masonry, where out-of-plane failure of individual walls dominates once diaphragm integrity is compromised (Işık et al., 2023; Kocaman, 2024). In this case study, the same mechanism explains both the large dynamic displacements recorded in specific façades and the field damage observed after the 2023 event.

The base reaction plots (Figure 6-2 and Figure 6-3) further clarify this behaviour. They show that dynamic force demand approached but did not exceed the static pushover capacity in either X or Y direction. This indicates that although shaking mobilised the full strength of the structure, it did not push it beyond the ultimate limits identified by pushover analysis. The time-history traces also reveal that demand fluctuates with the cyclic pulse and decreases once shaking subsides. This observation is consistent with the strain field patterns, where cracks accumulated but also partially closed during unloading. Cyclic opening and closing of cracks has been widely reported in experimental and numerical studies of masonry subjected to strong ground motion, and smeared strain plots are therefore best interpreted as upper-bound envelopes of maximum demand rather than residual damage states (Milani & Lourenço, 2012; D'Altri et al., 2020).

This interpretation helps explain why the structure exhibited progressive cracking without global collapse. The cyclic nature of loading allowed partial recovery of stiffness as cracks closed, even though the cumulative effect still degraded box behaviour and out-of-plane stability. This behaviour is consistent with previous nonlinear masonry dynamics research, which shows that cracks act as load-dependent hinges that repeatedly open and close depending on the motion (Betti & Vignoli, 2011; D'Altri et al., 2020).

It should be reiterated that pushover and dynamic analyses are not directly comparable in absolute terms. Pushover identifies governing mechanisms and approximate thresholds, while dynamic simulations capture cyclic degradation and higher-mode effects. The focus here is on consistency in mechanisms, not numerical equivalence of capacities or drifts.

Overall, the discussion highlights the complementary value of static and dynamic analyses. Pushover analysis is useful for identifying governing mechanisms, while dynamic simulation captures cyclic degradation, torsional participation, and higher-mode effects. Taken together, the findings demonstrate that the mosque's performance, though degraded, remained within a repairable range, understood as localized cracking at openings and dome–drum transitions, absence of masonry crushing or stability loss, base reactions below the pushover plateau, and no sustained residual drifts that would require partial rebuilding, establishing a foundation for the wider societal and intervention-oriented discussion in Chapter 7.

7. Dynamic Analysis with Impact Loading

7.1. Introduction

The isolated dynamic analyses in Chapter 6 established the mosque's baseline seismic response and did not indicate a global collapse tendency under the applied record. In dense urban settings, however, the behaviour of historic masonry can be altered by interaction with neighbouring structures through mechanisms such as pounding, progressive "domino" collapse, or debris-induced pressure on façades (Miari et al., 2019; Brown & Elshaer, 2022). For masonry aggregates, such interaction is known to redistribute demand, reduce global displacements in some cases, and simultaneously concentrate local out-of-plane effects at vulnerable connections and openings (Malomo & DeJong, 2024; Bianchini et al., 2024). These observations motivate testing whether neighbour interaction could have influenced the Adıyaman Grand Mosque's response.

Field evidence from the 2023 Kahramanmaraş earthquakes around the mosque site shows widespread damage to mosques and minarets, with several studies highlighting the sensitivity of façade–floor connections and dome–drum regions to out-of-plane actions and secondary demands from adjacent construction (Işık et al., 2023; İzol et al., 2024; Kocaman, 2024). At Adıyaman, photographic records indicate the collapse of a reinforced-concrete building towards the mosque, plausibly producing debris contact and sustained lateral pressure on the upper south façade. Unlike brief cyclic pounding, such contact can behave as a one-sided, prolonged demand acting concurrently with seismic shaking (Brown & Elshaer, 2022).

The aim in this chapter is therefore not to reproduce debris kinematics or contact mechanics, but to explore how the mosque's response trends change when a simplified one-sided lateral pressure, representing debris contact, is superposed on the recorded ground motion. Following common practice for heritage assessments that balance realism and parsimony (Lourenço, 2001; D'Altri et al., 2020; Roca et al., 2019), an equivalent façade pressure is superposed on the recorded base excitation to mimic a sustained debris "lock-in." The approach is intended to indicate trend-level redistribution of response rather than to deliver calibrated predictions of impact behaviour.

The scope is explicitly limited. The simplified loading representation neglects short-duration force spikes, momentum transfer, frictional slip and wedging at contact points, vertical load transfer through deposited debris, and time-varying engagement as rubble settles, phenomena that the pounding literature indicates can decisively influence outcomes (Miari et al., 2019; Brown & Elshaer, 2022; Malomo & DeJong, 2024). Results are interpreted qualitatively and comparatively against the isolated baseline from Chapter 6, and no quantitative claims are made about damage states or collapse triggers.

Within these boundaries, the chapter contributes to RQ2 by (i) formulating a transparent and traceable equivalent sustained lateral-pressure model for neighbour interaction, (ii) discussing the assumptions required to implement it using the available information, and (iii) demonstrating why, given the neglected mechanisms, this simplified approach is insufficient to reach a realistic, evidence-consistent conclusion. The discussion identifies the additional data and modelling ingredients needed for a defensible assessment of debris–structure interaction on historic masonry, namely explicit contact mechanics with restitution and friction,

time-varying contact area and pressure, possible eccentric contact paths, and vertical load transfer or wedging through rubble, as highlighted in recent interaction and pounding studies (Miari et al., 2019; Brown & Elshaer, 2022; Malomo & DeJong, 2024; Bianchini et al., 2024; Maniatakis et al., 2018). These requirements should be embedded within heritage modelling frameworks that balance parsimony and realism (Lourenço, 2002; Giamundo et al., 2014)..

7.2. Methodological Approach

This section adopts an idealised representation of neighbour interaction as a sustained, one-sided lateral pressure added to the recorded base excitation. The objective is to examine changes in response trends, such as façade criticality and out-of-plane effects, under a simplified pressure that represents debris lock-in, rather than to provide quantitative predictions of impact behaviour. The model does not simulate debris kinematics, contact friction, or momentum transfer. It is an equivalent sustained lateral-pressure model used only to test whether additional out-of-plane demand could redistribute the response; results are interpreted in qualitatively terms, not as calibrated predictions.

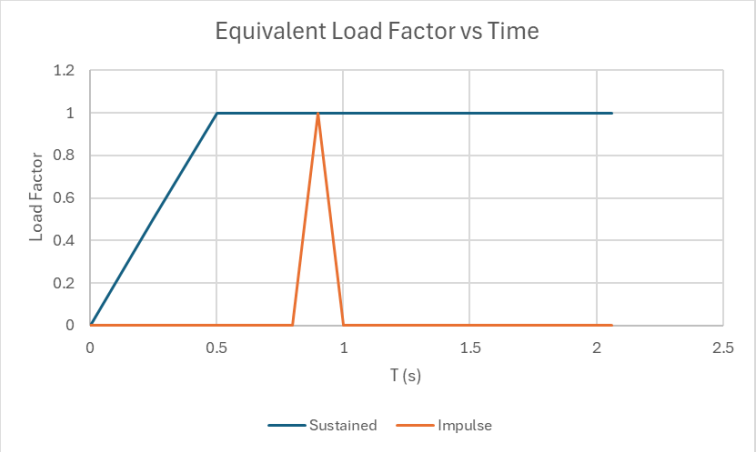

Figure 7-1 Adopted sustained pressure history and an idealised impulse shown for context (impulse not used).

Once debris bears on the façade, contact is assumed to remain engaged and to apply a continuous pressure rather than an impulsive pounding force. Numerically, a façade area load is ramped linearly over 0.5 s to represent engagement and then held constant for the rest of the duration (Figure 7-1). The 0.5 s ramp is a modelling convenience to avoid numerical transients; it is not a measured collision time.

To set the magnitude of this pressure, a simplified reconstruction of the neighbouring RC frame was used to estimate mass, fundamental period, and modal participation in the collapse direction. These were combined with site-specific spectral acceleration at that period (Figure 7-5) to derive an equivalent lateral force and the corresponding uniform wall.

However, it should be noted that this approach neglects some key aspects such as short-duration force spikes from debris impacts, time-varying contact as rubble settles, vertical load transfer and torsional effects, and local crushing or wedging at contact points. The approach is intended for sensitivity trends only.

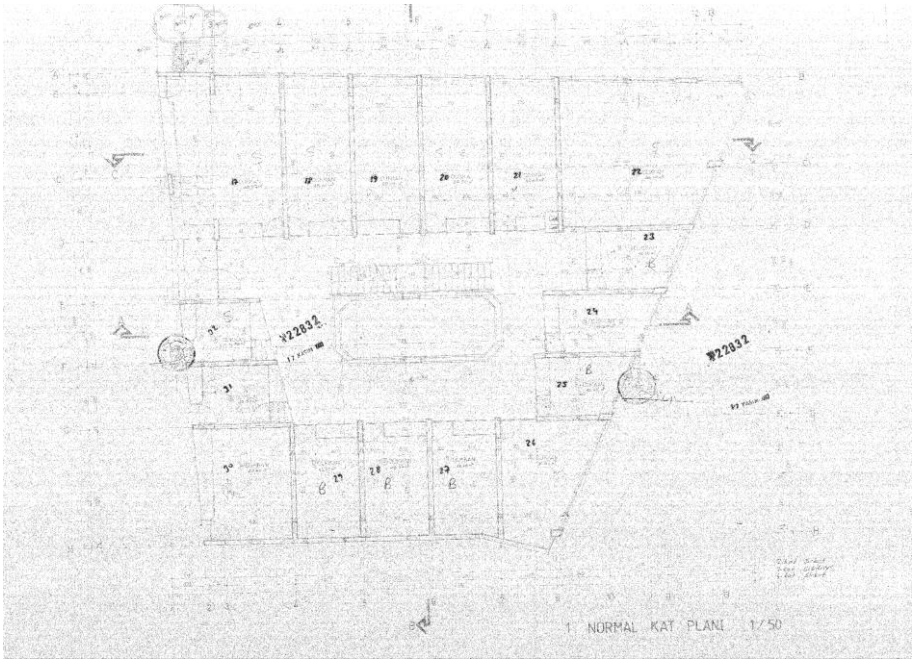

Figure 7-2 Typical floor plan of the neighbouring RC building (archival drawing, dimensions partially assumed)

Figure 7-2 shows the typical floor plan of the neighbouring RC building. Archival drawings were incomplete, with limited details on the dimensions of columns, beams, and slabs. Consequently, geometry modelling was supplemented by reasonable engineering assumptions, using typical cross-section sizes for reinforced-concrete frames in mid-rise residential buildings, for example, a column height of 3.5 m, and a beam/column dimensions of 300 × 600 mm^2 based on the proportion in archived drawings.

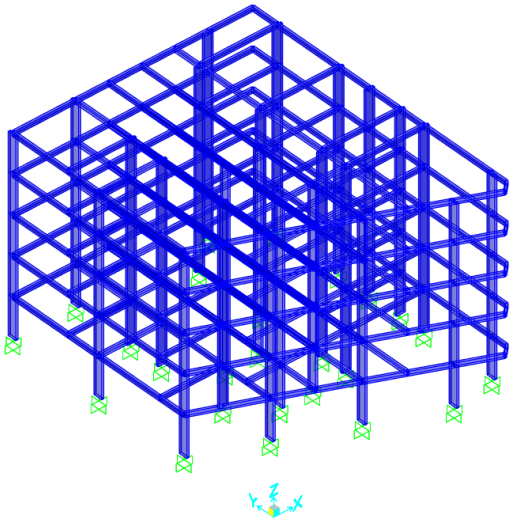

Figure 7-3 Reconstructed RC frame used to estimate m, T_n and ϕ.

Figure 7-3 shows the analytical model of the neighbouring reinforced-concrete (RC) frame. This additional model was not coupled to the mosque; it was used solely to extract the parameters required to size an equivalent lateral pressure:

- Building mass (m).
- Natural period (T_n).
- Mass participation factor in the collapse direction (ϕ).

The building mass was estimated from the approximate floor plans and elevations using typical slab and beam thicknesses and a unit weight of 25 kN/m³ for reinforced giving m = 3.93×10^5 kg. An eigenvalue analysis of the frame gave T_n = 0.963 s and ϕ = 0.66 for the direction consistent with the observed collapse (Figure 7-4).

Figure 7-4 Photographic evidence indicating collapse direction toward the mosque.

To represent the inertial demand mobilised during collapse, the spectral acceleration at the RC frame's period was read from three spectra: the site-specific design spectrum and the recorded event spectra in the E–W and N–S directions (Figure 7-5). The site-specific spectrum produced the largest value at T_n = 0.963 s, namely a_{Tn} = 0.524 g, and was therefore adopted as conservative.

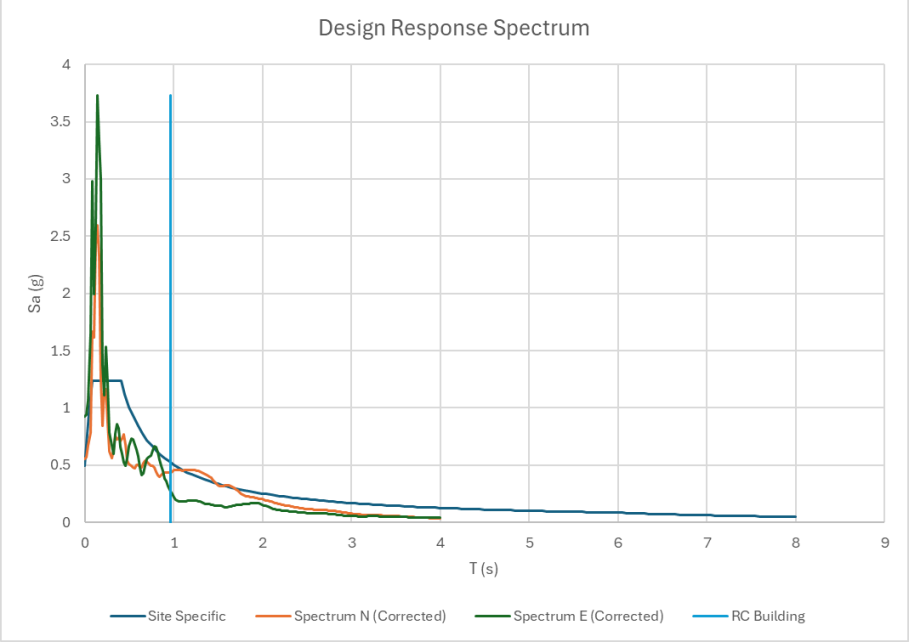

Figure 7-5 Spectral accelerations at T_n=0.963 s from site-specific and recorded spectra.

The equivalent lateral force associated with the collapsing RC mass is then

$$F_h = \phi\, m\, a_{Tn} \qquad (7-1)$$

$$F_h = 0.66 \times 3.93 \times 10^2 \times 0.524g\ kN$$

$$F_h = 1333.04\ kN$$

This force was mapped to a uniform pressure acting on the likely contact region at the top of the South façade. Taking an effective contact area A_{top} = 98.91 m^2, the imposed pressure is

$$q_h = \frac{F_h}{A_{Top}} = \frac{1333.04}{98.91} = 13.48\ kN/m^2 \qquad (7-2)$$

Figure 7-8 illustrates the applied façade pressure in the DIANA model. Numerically, the pressure ramps linearly from zero to q_h over the first 0.5s to represent engagement and then remains constant for the remainder of the two-second input window. The ramp is a modelling convenience to avoid numerical transients; it is not a calibrated contact duration.

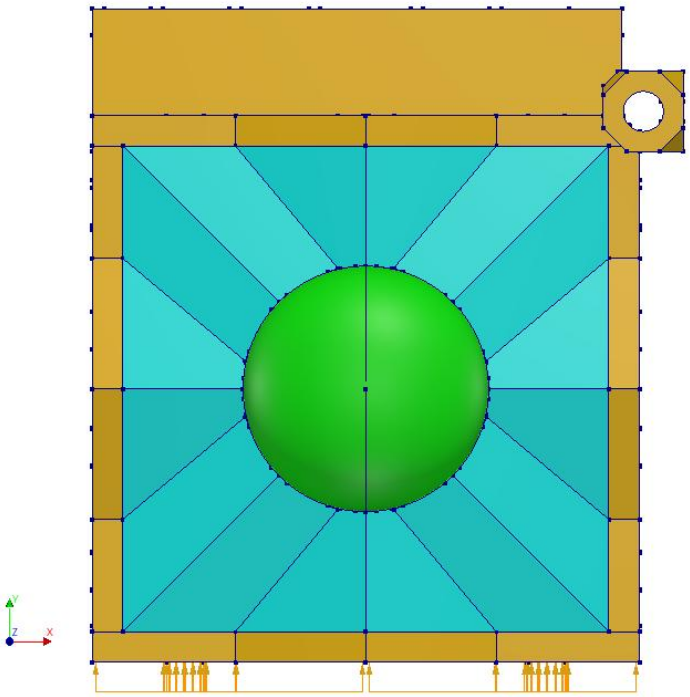

Figure 7-6 Plan view of loaded façade and collapse direction. The equivalent uniform pressure q_h is applied to the South wall along the highlighted contact zone.

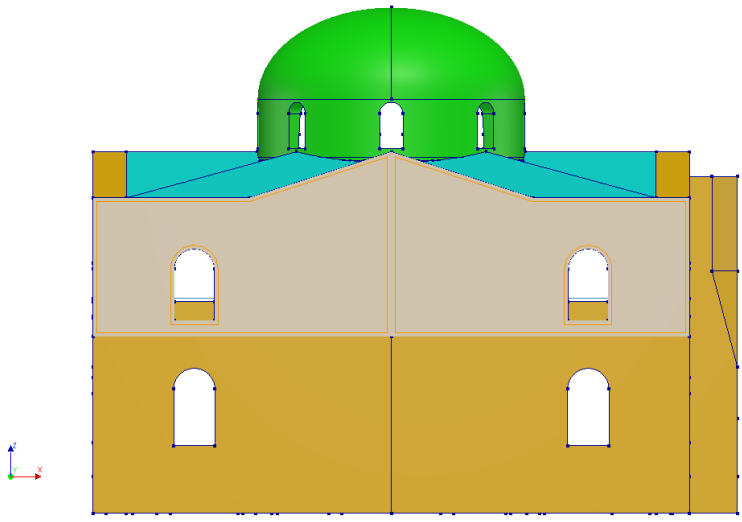

Figure 7-7 Elevation of the South façade showing the extent of the equivalent uniform pressure q_h applied to the upper wall zone; loading increases linearly over 0–0.5 s and then remains constant.

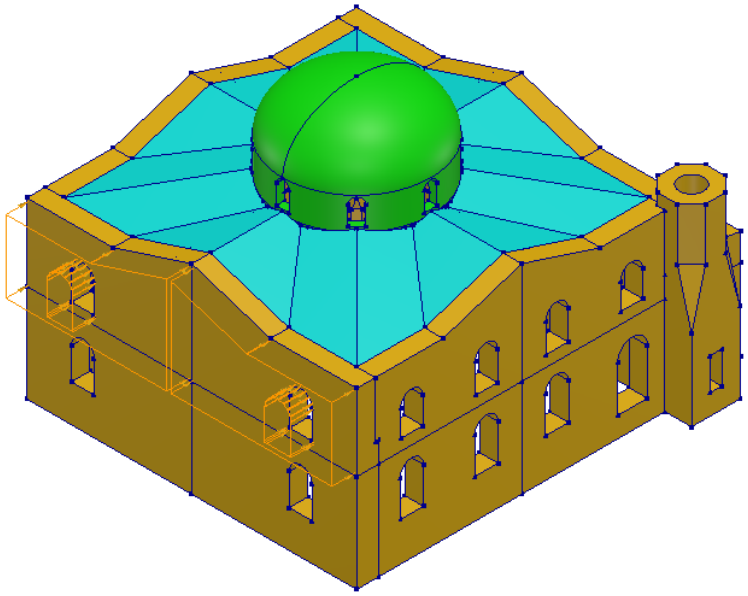

Figure 7-8 Implementation of the equivalent uniform pressure q_h on the South façade.

For consistency with Chapter 6, the same Rayleigh damping parameters as the corrected isolated model are used. Only the loading window is shortened to focus on the strong-motion pulse where the largest displacements occur. The intent is to test the sensitivity of global response to a sustained one-sided pressure superposed on the recorded base motion, not to reproduce debris kinematics.

The equivalent lateral load scheme:

- Treats the RC debris action as a continuous out-of-plane pressure (no pounding impulses, no momentum transfer, no contact friction).
- Assumes a uniform pressure over A_{top} (no local wedges, arching, or concentrated crushing at contact points).
- Neglects vertical load transfer, torsional effects from eccentric contact, and time-varying contact as rubble settles, and

- Uses a lower-bound spectral acceleration (largest at T_n) to size F_h while keeping the action constant in time.

Within these bounds, the setup offers a transparent and reproducible surrogate to examine whether additional one-sided demand could redistribute the response relative to the isolated case. Results are interpreted at trend level only and are not used as quantitative predictions of real impact behaviour. The setup considers a lower-bound scenario: the sustained uniform pressure likely underestimates transient contact impulses, local wedging, and torsional effects. If this simplified loading were to produce a severe response, a more realistic interaction would plausibly be worse; the converse does not hold.

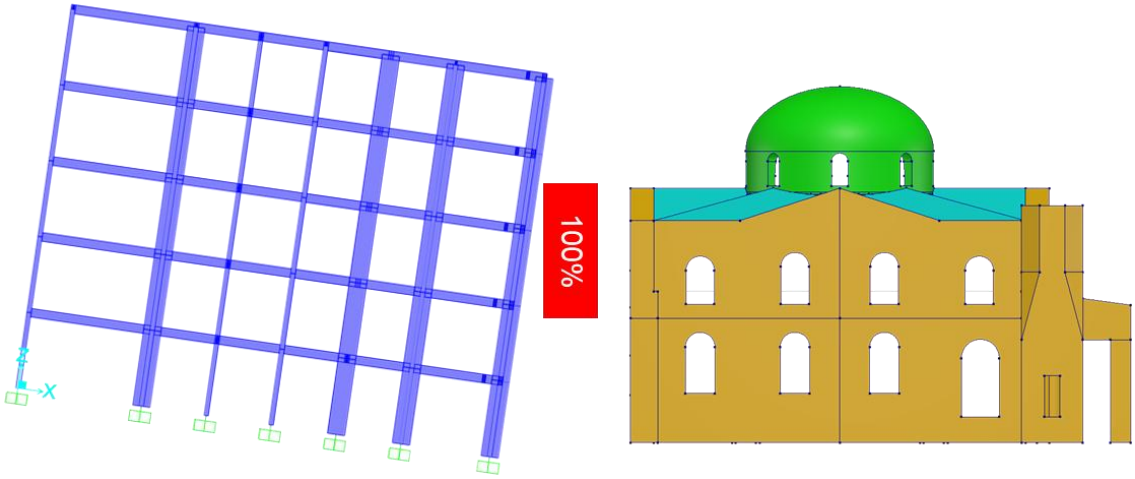

Figure 7-9 Location of applied load on the South wall (schematic).

7.3. Modelling Assumptions

The inclusion of the interaction loading case is set up to read the direction and relative size of changes in the mosque's response, not to predict exact values. In practice, the analysis is comparative and qualitative: it asks which façades become more or less critical, whether out-of-plane demand increases, and how strain localisation shifts when a sustained lateral pressure is added. It does not aim to deliver calibrated absolute drifts, forces, or damage states. This follows accepted practice in heritage modelling when information is limited, emphasising parsimony and transparent assumptions (Lourenço, 2001; Lourenço, 2002; Roca et al., 2019; D'Altri et al., 2020). To keep the comparison meaningful, all numerical settings from the isolated runs are retained, including the recorded base motion, Rayleigh damping, mesh, and constitutive parameters; the only change is the added façade pressure (Betti & Vignoli, 2011).

Table 7-1 Key inputs for the sustained-pressure case and values used in the analysis.

Symbol	Quantity (definition)	Adopted value/ Units	Source	Notes & uncertainty
m	Estimated total mass of the neighbouring RC frame	3.93×10^5 kg	From reconstructed floor plans with typical RC densities and section thicknesses	Approximated geometry; ±15–25% uncertainty typical for archive-based estimates.
Φ	Modal participation factor in the collapse direction	0.66	From the eigenvalue analysis of the RC frame	Direction aligned with observed collapse path.
T_n	Fundamental period of RC frame	0.963 s	From the eigenvalue analysis of the neighbouring RC frame	Period used to read spectral acceleration.
a_{Tn}	Spectral acceleration at (T_n) (site specific)	0.524 g	From site-specific spectrum at (T_n)	Convert to m/s² when forming a force.
F_h	Equivalent lateral force	1,333 kN	Calculated from ($m\ \Phi\ a_{Tn}\ g$)	Rounded to nearest kN for reporting transparency.
A_{top}	Loaded wall area (upper South façade patch)	98.91 m²	Measured from the FE model	Planar projection used; small curvature ignored.
q_h	Uniform façade pressure	13.48 kN/m²	Calculated from (F_h / A_{top})	Applied as constant patch pressure after ramp.
α, β	Rayleigh damping coefficients	$\alpha = 1.265\ s^{-1}$ $\beta = 5.773 \times 10^{-4}$ s As stated in Chapter 6	Carried over from the calibrated isolated model	Ensure the exact values are repeated here for completeness.

The temporal history of the added action is a short linear ramp that reaches the target level at 0.5 s and then remains constant for the rest of the analysis window (Figure 7-1). This history is intended to stand in for debris that becomes engaged and remains pressed against the wall rather than for an impulsive pounding force. Reviews and experiments on interaction show that contact mode, duration, and friction strongly influence outcomes, and that contact can extend beyond instantaneous hits, especially in dense aggregates (Miari et al., 2019; Brown & Elshaer, 2022; Bianchini et al., 2024; Malomo & DeJong, 2024).

The spatial footprint is limited to the upper band of the south façade, where debris contact is most plausible. The pressure acts normal to the wall, uniformly over the shaded patch, so that local effects are not prescribed and global redistribution can be read clearly.

The magnitude of the sustained pressure is obtained from a simplified reconstruction of the neighbouring reinforced-concrete frame, used only to estimate the mass, fundamental period, and modal participation in the collapse direction. These are combined with the site-specific spectral acceleration at that period to obtain an equivalent lateral force, which is divided by the

contact area to give a uniform pressure on the façade. The calculation is reported so it can be traced independently of the numerical model.

Table 7-2 Summary of assumptions and mechanisms not represented in the simplified interaction model.

Mechanism / effect	Represented in model?	How it is represented	Omitted aspects	Likely influence on trends
Recorded base excitation	✓	Site record applied at base (shortened window)	Long-duration low-frequency content in longer recorded motion	Minimal for the intent of this chapter; full record treated in Ch.6.
Sustained debris "lock-in" pressure	✓	Uniform pressure q_h on South upper façade; linear ramp $0 \rightarrow q_h$ to q_h in 0.5 s; then constant	Contact area growth/decay; non-uniform patching; eccentricity	Captures trend toward out-of-plane demand redistribution.
Impulsive impact spikes	✗	—	Short-duration force peaks, restitution, and local contact stiffness	Would increase peak local stresses and may trigger cracking earlier.
Time-varying engagement	✗	—	Pressure evolution as rubble settles or sheds	Could shift response timing and produce additional cycles.
Vertical load transfer / wedging	✗	—	Axial thrust into parapets/gables; arching of debris	Could amplify compression near the contact and change hinge locations.
Torsional effects about vertical axis	✗	—	Eccentric line of action, asymmetric debris	Could bias drift between return walls.
Local crushing at contact	✗	—	Nonlinear contact pressure–area evolution	Would localise damage and reduce effective contact width.
Energy loss at contact (friction, sliding)	✗	—	Stick–slip, frictional dissipation	Would alter the effective duration and amplitude of pressure.
Material nonlinearity of the mosque	✓	Total Strain Crack model with softening in tension/compression	Rate effects; dynamic fracture-energy variation	Suitable for trend-level global redistribution.
Roof/floor diaphragm action	✓	As per Ch.6 model	Diaphragm degradation due to contact	Could reduce box behaviour and increase out-of-plane deflection.

This representation makes deliberate simplifications. Short-duration force spikes due to block impacts, momentum transfer at first contact, frictional slip or wedging at edges, vertical load transfer and torsion from eccentric debris mounds, and time-varying engagement as rubble settles are not simulated. The pounding and contact literature show that these mechanisms can control local damage, alter out-of-plane response, and change crack nucleation at weak connections and openings (Miari et al., 2019; Brown & Elshaer, 2022; Malomo & DeJong, 2024; Bianchini et al., 2024). The intent here is therefore to examine how an additional sustained transverse demand could redistribute response trends relative to the isolated baseline from Chapter 6, not to infer damage states or collapse triggers.

Finally, the chosen history and uniform distribution constitute a lower-bound representation of interaction. If a sustained pressure at the level reported in Table 7-2 was sufficient to provoke severe response trends; more localised interaction would be expected to be at least as severe. Because the neglected mechanisms may either amplify or attenuate response depending on geometry and friction, the conservative character of the setup is acknowledged explicitly and is discussed further in the limitations that follow (Lourenço, 2001; Roca et al., 2019).

7.4. Expected Response under Simplified Interaction

The simplified interaction explored in this chapter assumes a one-sided, sustained lateral pressure that acts concurrently with the recorded base excitation. This pressure stands in for debris lock-in rather than a short impulsive hit and is intended only to reveal trend-level redistribution rather than to predict calibrated impact behaviour.

Within this idealisation, the added façade pressure biases the response towards the loaded side. Because the load acts over a limited area and is held approximately constant, its strongest influence is local: higher overturning on the pressed façade, earlier cracking around openings and at the wall-roof or wall-dome junctions, and a mild torsional drift towards the loaded corner. These outputs could be reported only as qualitative trends that indicate which façades become more or less critical and where strain tends to localise. Unfortunately, this set-up is not suitable for estimating absolute forces, drifts, or damage states because it omits short contact pulses, friction, eccentricity of the line of action, and any vertical load transfer through debris. A more reliable assessment requires the full ground-motion record and, preferably, explicit interaction modelling with time-varying contact, friction, plausible eccentricities, and debris-borne vertical transfer. The interpretation that follows therefore emphasises mechanisms: as box behaviour weakens on the loaded side, out-of-plane overturning becomes the critical response, while in-plane demand becomes secondary.

Regarding displacement and drifts, the critical response shifts toward the side subjected to pressure, where the out-of-plane overturning governs. Under such impact-dominated loading, drifts perpendicular to the pressed wall may increase significantly, as the façade undergoes overturning or collapse driven by the impulsive force. In contrast, the in-plane demand becomes comparatively less significant, since the structure is already driven toward failure by the out-of-plane action.

Such changes should be interpreted qualitatively, as the adopted load does not capture momentum transfer, restitution, or evolving contact patch stiffness that strongly influence impact transients (Miari et al., 2019; Brown & Elshaer, 2022). These trends must therefore be considered alongside clear limitations. The loading scheme neglects short-duration force spikes, frictional slip and wedging at contact points, vertical load transfer through debris arching, torsional effects, and time-varying engagement as rubble settles. Each of these omissions may either amplify local stresses or alter the initiation of critical mechanisms. Accordingly, the current scheme should be regarded as representing a lower-bound action in terms of short-duration peaks. As a result, the discussion of damage should remain at the mechanism level rather than at the state-of-damage level, and quantitative claims regarding collapse triggers are not warranted.

In summary, the simplified interaction is useful to discuss how neighbour effects could shift demand paths toward out-of-plane mechanisms on the pressured façade and to highlight the sensitivity of historic connections. It is not suitable for drawing calibrated conclusions about the severity or exact location of damage. This framing supports the overall argument of the chapter: with the available information and the necessary simplifications, the approach is adequate to discuss plausible trends, but insufficient for realistic, evidence-consistent conclusions about impact-driven failure.

7.5. Why Simplified Approach is not Sufficient

The equivalent sustained lateral-pressure model in Section 7.2 was designed to be transparent and minimal. It captures the idea of debris "lock-in" acting with the recorded shaking, and it allows trend-level discussion of how additional out-of-plane demand may redistribute response. It is also a lower-bound representation since it omits short spikes, local wedging, frictional slip, evolving contact area, torsional eccentricity, and vertical thrust paths through rubble, all of which the interaction literature identifies as decisive in aggregates of masonry buildings (Miari et al., 2019; Brown & Elshaer, 2022; Malomo & DeJong, 2024; Bianchini et al., 2024). Modelling guidance for historical masonry structures further cautions that when the governing mechanism is uncertain, simplified loads should frame hypotheses rather than support calibrated conclusions (Lourenço, 2001; Lourenço, 2002; Roca et al., 2019; D'Altri et al., 2020).

Two uncertainty groups dominate. Event-side uncertainties concern the neighbouring building, including the timing of its failure relative to the strong-motion pulses, the participating mass and its trajectory, the first-contact footprint and height, frictional characteristics at contact, and whether contact was intermittent as debris settled. Receiver-side uncertainties concern the mosque, including the continuity of diaphragms at roof and drum-arch junctions, potential torsional coupling, prior stiffness loss before contact, and any vertical load transfer that could shift hinge locations. Each factor can alter the time history, localisation, and severity of demand in ways a uniform sustained pressure cannot reproduce (Miari et al., 2019; Brown & Elshaer, 2022; Roca et al., 2019; D'Altri et al., 2020).

Because the adopted loading acts as a smooth bias rather than a sequence of impulses, global indicators such as summed base reactions and façade-top drifts are not diagnostic for impact phenomena. They are spatially averaged, insensitive to patchy or eccentric contact, and depend on cyclic degradation features that are not calibrated for repeated opening and closing under contact. As noted in historic-masonry dynamics, reading time-history demand against monotonic envelopes is useful for context, but it does not adjudicate mechanism when contact physics are outside the model scope (Betti & Vignoli, 2011; D'Altri et al., 2020; Roca et al., 2019).

The implication for RQ2 is therefore limited but clear. The isolated analyses up to Chapter 6 did not exhibit a global collapse tendency under the record, which supports a parsimonious view that an external trigger is plausible. The simplified interaction adopted here indicates the direction in which neighbour effects could shift demand paths, namely towards out-of-plane mechanisms at the pressured façade, yet it cannot provide a realistic or quantitative judgement of impact behaviour for the Adıyaman case. A credible assessment would require either explicit

contact modelling with normal and tangential laws, evolving contact area, and allowance for eccentric multi-point engagement, or a carefully designed set of bounding pulse-type load cases that vary amplitude, duration, area, and eccentricity to bracket plausible impulses without full contact mechanics. In both routes, additional evidence is needed to constrain the neighbour's participating mass and failure sequence, likely contact footprints and heights, and the diaphragm connectivity of the mosque.

In summary, the chapter establishes a clear and reproducible simplified interaction model, shows why its assumptions are likely to be insufficient for mechanism attribution, and delineates the data and modelling ingredients required for a defensible impact-interaction study. Accordingly, Chapter 7 supports a cautious position for RQ2: neighbour interaction remains a credible driver of the observed severity, but the present evidence and model are not adequate to attribute the sequence or to quantify damage. The findings from Chapter 6 should be treated as the robust baseline, and any future interaction study should incorporate contact-explicit effects or bounding pulses constrained by event data.

8. Conclusion

The analyses indicate that, in isolation, the mosque exhibited a stable yet vulnerable seismic response under the applied record. Modal analysis, pushover evaluation, and the dynamic time-history run consistently show equilibrium with drift demands and base reactions remaining below the direction-specific pushover plateaus. Cracking concentrates at openings, intermediate wall bands, and the dome to drum transition and forming hinge lines. In this report, repairable is used qualitatively to mean localized cracking at openings and roof–wall or dome–drum transitions, no masonry crushing or stability loss, base reactions within the peak lateral strength, and no persistent residual drifts that would necessitate partial rebuilding. Under this definition, the isolated response falls within a repairable range.

Neighbour interaction was explored using a simplified scheme that adds a sustained one-sided lateral pressure to the recorded base motion. The aim was to examine response trends, not to deliver calibrated impact predictions. Within that exploratory scope, the adopted loading scheme provides a lower-bound representation of impact action. These trends must be read with caution, since the model omits short-duration force spikes, time-varying contact, vertical load transfer through debris, and local wedging or crushing at contact points. The method, therefore, cannot support quantitative claims about damage states or collapse triggers.

Taken together, the findings support the view that the mosque possessed sufficient intrinsic capacity to endure the imposed shaking with repairable levels of damage. The more severe condition is plausibly associated with the neighbouring reinforced-concrete building, whose collapse could have transformed otherwise repairable cracking into non-repairable out-of-plane mechanisms through demand redistribution. The simplified interaction study in this chapter does not prove that sequence, but it reinforces the need for an interaction-aware assessment that includes explicit contact transients, evolving eccentricity of pressure, and vertical load sharing and bending.

Answers to Research Questions

1. **What is the seismic capacity of the mosque in isolation, and what mechanisms govern its failure?**
   The mosque sustains equilibrium under the applied record with base reactions below the pushover plateaus. Damage concentrates as horizontal cracking over openings, diagonal bands between openings, and hinge formation at the dome to drum and roof–wall regions, consistent with the mechanisms identified in pushover analysis. Using the qualitative definition above, the isolated response remains repairable.
2. **How does interaction with neighbouring structures influence this behaviour?**
   The simplified interaction loading, used only to explore trends, indicates redistribution of seismic demand that tends to amplify out-of-plane vulnerability at exposed façades. Because key contact and debris mechanisms were not modelled, these observations are not presented as quantitative results. The overall interpretation is that external interaction is a credible trigger for the most severe observed failures, and a defensible assessment would require richer data and modelling of contact transients, evolving pressure, eccentricity, and vertical load transfer.

9. Reflection and Recommendation

9.1. Reflection on Research Process

Technical Insights

When I moved from the proposal stage to the formal start of this thesis, the second research question felt daunting. I chose a simplified route for neighbour interaction: I modelled the collapsed RC building as a sustained one-sided lateral pressure superposed on the recorded base motion, with a short ramp only to avoid numerical transients. My intention was to probe trends, not to deliver calibrated impact predictions.

With that choice, I am clear about what the model does and does not represent. It does apply the site motion and a sustained façade pressure on the upper South wall to mimic debris "lock-in." It does not include short force spikes from rubble impacts, momentum transfer or restitution, frictional slip and wedging at contact points, time-varying contact area as rubble settles, eccentricity and vertical load transfer, or torsional coupling. I therefore expected the scheme to highlight redistribution of demand toward out-of-plane effects at exposed façades, while base reactions remained governed by the recorded motion.

For the isolated condition, the modal checks, pushover curves, and time-history run converged on the same mechanisms: cracking at openings and intermediate wall bands, and hinge formation at the roof–wall and dome–drum transitions. Throughout the thesis I use the word repairable in a qualitative sense only. By this I mean: cracks localised at known weakness zones, no crushing or stability loss, base reactions within the pushover plateau, and no persistent residual drifts that would force partial rebuilding. I did not compute quantitative thresholds such as residual drift limits or repair cost ratios, and I state that limitation explicitly.

Methodological Considerations

I balanced fidelity and feasibility. The solid macro model with a fixed-crack total strain law captured hinge lines, torsional participation, and mixed-mode cracking convincingly, but it demanded careful meshing and long run times. Light viscous damping was a practical stand-in for unmodelled dissipation.

Looking back, I would structure the workflow differently:

- Keep a fast 2D or shell benchmark in parallel for early "sanity checks," parameter scans, and mesh sensitivity,
- Reserve the solid model for mechanism studies and verification, and
- Adopt a layered interaction strategy: start with equivalent loads to explore plausible ranges, then progress to contact patches with evolving pressure and eccentricity when the question truly requires it.

For interaction and impact analysis, I also learned to document assumptions more explicitly. In this project, I assumed one contact patch on the upper south façade, a linear ramp in 0.5 s to a constant level, and mass and modal participation of the neighbour from a reconstructed frame.

These choices were reasonable with the available information, but they should be read as inputs to a sensitivity discussion, not as facts about the collapse.

Personal and Process-Related Reflection

The most difficult phase was the initial model setup. I spent roughly five to six weeks on geometry import, self-weight equilibrium, and checking the eigenvalue analysis. That pushed the greenlight to late September and created deadline pressure. I also waited on long dynamic runs while damping settings were being corrected. In hindsight, I should have treated troubleshooting as a deliverable in itself: short, documented cycles with checkpoints for geometry cleaning, mesh quality, reaction balance under gravity, and modal plausibility before moving on. That discipline would have saved time and reduced stress.

On the positive side, the pushover stage gave me the first confidence boost. It was the moment I saw the model behaving as expected and aligning with field-consistent mechanisms. That base then helped me interpret the dynamic runs and gave me the vocabulary to frame Chapter 7 as an exploratory trend analysis rather than a conclusive result.

Broader Relevance and Takeaways

This project changed how I think about seismic safety in dense urban areas. Intrinsic capacity may be adequate in isolation, yet secondary actions from neighbouring failure can govern outcomes. I also saw how modelling choices shape the story that analysis can tell; keeping assumptions explicit and conclusions at the mechanism level preserved credibility when evidence was limited. Despite setbacks, I gained technical depth in nonlinear masonry modelling and confidence in framing limitations honestly. If starting again, I would keep the same topic but plan a staged interaction study from the outset, with bounding contact scenarios and better constraints on the neighbour event.

9.2. Recommendation

Technical Recommendations

1. **Neighbouring-building interaction:** Move beyond the equivalent uniform pressure by introducing multiple contact patches, time-varying contact engagement, eccentric pressure resultants, and vertical load transfer through rubble. Where appropriate, allow for overturning moments from leaning debris. These refinements better capture timing, intensity, and localisation of interaction effects.
2. **Neighbour mass calibration:** Reduce reliance on assumed mass and modal participation by combining archival drawings, rubble photogrammetry/LiDAR, and structural analogues. Use a simple sensitivity bracket (minimum–likely–maximum) to propagate uncertainty into the equivalent force.
3. **Modelling strategies:** Adopt a staged workflow:
    a. Stage A: fast screening with shell/2D models and equivalent loads to map plausible ranges.

    b. Stage B: solid macro FE for mechanism confirmation and crack pattern realism.
    c. Stage C: local contact or discrete-element sub-models to study patch-wise impacts and crushing at contact points. Promotion between stages should be triggered only when the research question requires added fidelity.
4. **Dynamic calibration:** Calibrate damping and stiffness with modal testing (ambient vibration or simple hammer tests) so that time-history amplitudes and phase agree with the pushover plateaus and observed frequencies. Report the calibrated damping targets and achieved ratios.
5. **Acceptance criteria for qualitative states**: When quantitative damage indices are unavailable, state the qualitative thresholds explicitly: "repairable" means cracking without crushing or stability loss at roof–wall or dome–drum regions, base reactions within pushover plateaus, and no persistent residual drifts that would require partial rebuilding. Use these as reporting checks in future work.

Methodological Recommendations

1. **Troubleshooting and workflow efficiency:** The extended effort required during the initial modelling phase highlights the need for a more structured troubleshooting strategy. Documenting systematic checkpoints (geometry cleaning, mesh refinement, convergence tests) at early stages would shorten delays in future projects.
2. **Simplified validation models:** Running parallel shell-based or 2D frame models during early phases could provide quick benchmarks, helping to identify inconsistencies before committing to a complex full-scale model.
3. **Combination of analysis levels:** Where multiple contact patches are likely, couple global FE with small local models (macro–micro) instead of attempting a single monolithic model. This reduces computational burden while improving confidence in local stress predictions.

Broader Reflections

1. **Data acquisition for urban interaction:** For sites similar to Adıyaman, prioritise: measured façade gaps and heights of potential contact, wall-to-floor ties and diaphragm continuity, likely debris directions and contact areas, and neighbour geometry/mass from archives or post-event scans.
2. **Comparative case studies:** Extend the approach to additional mosques or historic masonry buildings in dense urban settings to test whether the domino-type collapse and demand redistribution observed here are typical or case-specific.
3. **Practice guidance:** Encourage heritage risk assessments to include neighbour-collapse scenarios explicitly, pairing building-specific capacity checks with context-driven interaction pathways.

Altogether, the study highlights that the seismic safety of historical buildings depends not only on their intrinsic resilience but also on the broader urban context, and that advancing this field requires both technical insight and a practical approach.

Appendix A. Literature Review Table

Table A-1 Literature Review Table

Author	Title	Year	Modelling Strategies					Methodology	Findings	Research Gaps
			Shell	Solid	Linear	Nonlinear	Modal			
P. B. Lourenço	*Experimental and Numerical Issues in the Modelling of the Mechanical Behaviour of Masonry*	1998	✖	✖	✓	✓	✖	• Reviewed **displacement-controlled experiments** to evaluate tensile, compressive, and shear properties. • Integrated experimental tests with numerical models to analyse crack propagation and joint behaviour. • Proposed continuum mechanics for macro-models.	• Micro-modelling accurately captures **unit-mortar behaviour** but is computationally expensive. • Macro-modelling simplifies masonry into a continuum for global analysis but misses localized behaviours. • Calibration requires extensive **experimental validation** of masonry properties.	• Limited **softening data** for post-peak masonry behaviour. • Insufficient integration of **experimental and numerical methods** for dynamic loading scenarios. • Challenges in capturing **nonlinear behaviour** in continuum models for historical structures.
P. B. Lourenço	*Analysis of Historical Constructions: From Thrust-Lines to Advanced Simulations*	2001	✖	✖	✓	✓	✖	• Applied **graphical thrust-line methods** for arches and vaults. • Conducted **nonlinear FEM simulations** to trace cracking and failure modes.	• Thrust-line methods are effective for simple collapse mechanisms but inadequate for dynamic loads. • Nonlinear FEM predicts cracking and	• Need for **dynamic analysis** to address seismic behaviour comprehensively. • Limited **material characterization**

Author	Title	Year	Modelling Strategies					Methodology	Findings	Research Gaps
			Shell	Solid	Linear	Nonlinear	Modal			
								• Utilized **case studies** (e.g., São Torcato Sanctuary) to validate the proposed methodologies.	material degradation accurately but requires substantial computational resources.	**data** (e.g., tensile and shear strength). • Lack of methods for **progressive collapse analysis** for irregular geometries.
P. B. Lourenço	*Computations on Historic Masonry Structures*	2002	✓	✖	✖	✓	✓	• Advocates for **macro-modelling** to simplify masonry behaviour. • Introduced **structural component models** for simplified geometric analyses. • Explored **analytical and FEM approaches**.	• Macro-modelling is efficient for **global behaviour** but lacks precision for localized failure. • Highlighted variability in **material properties** and its impact on modelling.	• Insufficient **material characterization** data for historic masonry. • Limited studies integrating **experimental and computational methods** for dynamic assessments.
P. B. Lourenço et al.	*Failure Analysis of the Monastery of Jerónimos: How to Learn from Sophisticated Numerical Models*	2006	✓	✓	✓	✓	✓	• Conducted **modal analysis** to validate mode shapes of FEM models. • Performed **pushover analysis** to simulate seismic behaviour. • Integrated **refined 3D FEM models** to assess critical vulnerabilities, including	• Simplified FEM is efficient for global behaviour but misses local failures. • Refined FEM models capture **localized failure mechanisms** such as hinge formation.	• Limited understanding of **dynamic interaction effects** between neighbouring structures. • Insufficient validation of **material properties**

Author	Title	Year	Modelling Strategies					Methodology	Findings	Research Gaps
			Shell	Solid	Linear	Nonlinear	Modal			
								hinge formation and **buckling**.	• Identified critical vulnerabilities in slender columns and towers under seismic loads.	(e.g., tensile strength). • Lack of methods to analyse **progressive failure mechanisms** under seismic scenarios.
Betti & Vignoli	*Numerical assessment of the static and seismic behaviour of the Basilica of Santa Maria all'Impruneta (Italy)*	2011	✓	✓	✓	✓	✓	• Finite element modelling (FEM) using **ANSYS v.11.0** • Nonlinear material modelling with **Mohr-Coulomb and Willam-Warnke failure criteria** • Pushover analysis for seismic assessment.	• Identified key failure mechanisms, including **out-of-plane failure of walls and overturning of façade elements**. • The **nave displayed weak lateral resistance due to insufficient buttressing**.	• Did not consider **interaction effects with surrounding structures** • Relied on **assumed material properties due to limited experimental data**.
Del Coz Díaz et al.	*Non-linear hygrothermal failure analysis of an external clay brick wall by FEM – A case study*	2011	✓	✓	✓	✓	✗	• FEM analysis in **ANSYS v.12.1** • Coupled **thermal-structural simulations** to assess the effects of **moisture expansion and thermal loads** on masonry failure.	• Identified that **hygrothermal expansion caused excessive stress in brick cladding, leading to progressive cracking and eventual collapse**.	• Did not assess **structural responses under dynamic seismic loading** • **Limited validation with experimental data**.

Author	Title	Year	Modelling Strategies					Methodology	Findings	Research Gaps
			Shell	Solid	Linear	Nonlinear	Modal			
P. B. Lourenço	*Analysis of Masonry Structures Without Box Behavior*	2011	✖	✖	✖	✓	✖	• Performed **nonlinear dynamic analysis** to evaluate seismic impacts on structures with weak wall-diaphragm connections. • Applied **pushover analyses** for lateral load resistance. • Developed case-specific **retrofitting recommendations** for box behaviour improvement.	• Structures lacking box behaviour exhibit poor seismic performance. • Retrofitting improves lateral resistance but is often costly. • Dynamic analysis reveals **collapse risks** due to weak inter-wall connections.	• Inadequate research on **progressive collapse mechanisms**. • Limited experimental data for **non-box behaviour validation**. • Need for cost-effective retrofitting techniques tailored to historical structures.
Giamundo et al.	*Evaluation of different computational modelling strategies for the analysis of low strength masonry structures*	2014	✖	✓	✓	✓	✖	• Compared FEM and DEM approaches for low strength masonry. • Evaluated different numerical modelling strategies.	• Found that DEM approaches perform better for low bond strength masonry, while FEM is more reliable for low unit strength masonry.	• Need for further validation against full-scale experimental tests. • Limited integration of hybrid modelling strategies.
Karanikoloudis & Lourenço	*Structural assessment and seismic vulnerability of earthen historic structures. Application of sophisticated*	2018	✖	✓	✖	✓	✓	• Applied nonlinear pushover and time-history analyses to evaluate seismic vulnerability of historic adobe structures. • Used macro-block limit analysis for performance-based assessment.	• Identified that adobe buildings are highly vulnerable due to weak connections and overturning resistance. • Validated the use of macro-modelling for	• Need for improved retrofitting strategies and better material characterization. • Limited studies on the effectiveness of

Author	Title	Year	Modelling Strategies					Methodology	Findings	Research Gaps
			Shell	Solid	Linear	Nonlinear	Modal			
	numerical and simple analytical models								large-scale adobe structures.	current strengthening techniques.
L.C. Silva et al.	*Seismic Structural Assessment of the Christchurch Catholic Basilica, New Zealand*	2018	✓	✓	✓	✓	✓	• Developed a **macro-modelling FEM** using DIANA software. • Combined **shell, solid, and beam elements** to represent structural components. • Conducted **pushover and modal analyses** to evaluate seismic response.	• Identified **bell towers** as the most vulnerable elements during seismic events. • Found that strengthening strategies (steel tie rods and ring beams) significantly improved structural behaviour but were insufficient to fully prevent collapse.	• **Vertical acceleration effects** were not incorporated into the model. • Limited representation of post-seismic retrofitting effects. • Need for better **calibration of material properties** with experimental data.
Maniatakis et al.	*Seismic response of a historic church considering pounding phenomena*	2018	✗	✗	✓	✓	✓	• Studied the impact of pounding on the Kaisariani Monastery church in Greece, using finite element analysis. Compared time-history and response spectrum methods.	• Found that pounding significantly affects seismic response, with response spectrum methods often underestimating damage.	• Need for improved unilateral contact modelling for masonry structures. • Lack of real-world validation studies.
A. Aşıkoğlu et al.	*Effectiveness of Seismic Retrofitting of*	2019	✓	✓	✓	✓	✓	• 3D FEM model combining **shell**, **solid**, and **beam elements**.	• Retrofitting using **steel girders** improved seismic performance.	• Limited **validation of the retrofitting**

Author	Title	Year	Modelling Strategies					Methodology	Findings	Research Gaps
			Shell	Solid	Linear	Nonlinear	Modal			
	a Historical Masonry Structure: Kütahya Kurşunlu Mosque, Turkey							• Performed **nonlinear pushover and dynamic analyses** to assess retrofitting strategies. • Calibrated FEM using ambient vibration measurements.	• Refined FEM captured **cracking in domes and walls**, correlating well with observed damage.	**technique** for future seismic scenarios. • Lack of **long-term performance assessment** for retrofitting measures.
Abdel Raheem et al.	*Numerical simulation of potential seismic pounding among adjacent buildings in series*	2019	✖	✓	✖	✓	✓	• Conducted nonlinear time-history analysis to assess seismic pounding effects on adjacent buildings in series. • Used ETABS for numerical modelling.	• Found that the severity of seismic pounding depends on building alignment, height differences, and ground motion characteristics. • Identified significant acceleration and displacement amplifications in taller buildings.	• Need for better mitigation strategies to reduce pounding effects in dense urban environments. • Limited validation against real-world earthquake data.
Miari et al.	*Seismic pounding between adjacent buildings: Identification of parameters, soil interaction issues, and mitigation measures*	2019	✖	✖	✓	✓	✓	• Reviewed past research on seismic pounding and its impact on various building types, including masonry structures. • Discussed soil-structure interaction effects.	• Identified that pounding can amplify seismic damage significantly, especially in buildings with different heights and stiffness.	• Limited experimental validation for soil-structure interaction effects on pounding. • No specific focus on historical masonry structures.

Author	Title	Year	Modelling Strategies					Methodology	Findings	Research Gaps
			Shell	Solid	Linear	Nonlinear	Modal			
									• Soil-structure interaction plays a crucial role.	
Aşıkoğlu et al.	*Pushover analysis of unreinforced irregular masonry buildings: Lessons from different modeling approaches*	2020	✖	✓	✖	✓	✓	• Conducted pushover analyses using different modelling approaches (continuum, macro-element, and equivalent frame models) on a two-story URM building with irregularities.	• Simplified models align well with experimental results but struggle to capture torsional effects accurately. • Found that structural irregularities significantly affect the reliability of simplified methods.	• Further refinement of simplified approaches is needed to better capture irregular masonry structures' seismic response. • Improved calibration for irregular geometries is required.
D'Altri et al.	*Modeling Strategies for the Computational Analysis of Unreinforced Masonry Structures: Review and Classification*	2020	✓	✓	✓	✓	✖	• Reviewed different computational modelling strategies for unreinforced masonry structures, classified into block-based, continuum, geometry-based, and macroelement models.	• Highlighted the strengths and limitations of each modelling strategy and their applicability to different structural problems.	• Need for better integration of modelling strategies for seismic assessment. • Limited experimental validation for hybrid approaches.
Brown & Elshaer	*Pounding of structures at*	2022	✖	✖	✓	✓	✓	• Conducted a comprehensive review of structural pounding cases, including city-scale assessments and	• Highlighted various pounding mechanisms and their consequences, including out-of-phase	• Lack of correlation between historical cases and modern analytical models.

Author	Title	Year	Modelling Strategies					Methodology	Findings	Research Gaps
			Shell	Solid	Linear	Nonlinear	Modal			
	proximity: A state-of-the-art review							experimental/numerical modelling approaches.	vibrations and progressive collapse risks.	• Need for guidelines integrating pounding effects into design codes.
Işık et al.	*Structural damage evaluation of Mosques and minarets in Adıyaman due to the 06 February 2023 earthquakes*	2023	✓	✓	✓	✓	✓	• Field survey of 27 Mosques and minarets • FEM-based analysis	• Identified minaret failures due to lack of engineering considerations • Collapse mechanisms mapped	• No assessment of multi-building interactions • Lack of progressive collapse studies
Bianchini et al.	*Influence of wall-to-floor connections and pounding on pre- and post-diction simulations of a masonry building aggregate tested on a shaking table*	2024	✖	✓	✖	✓	✓	• Conducted finite element analysis on masonry aggregates subjected to shaking table tests, comparing pre- and post-test numerical models.	• Found that wall-to-floor connections play a significant role in the response of adjacent masonry units. • Highlighted limitations in numerical modelling of pounding effects.	• Need for improved numerical validation against experimental data. • Limited integration of dynamic interaction effects.
Ergün & Tayfur	*Evaluation of the seismic performance pre- and post-restoration of a masonry clock tower*	2024	✓	✓	✓	✓	✓	• Experimental modal analysis • FEM updating via optimization • Time-history analysis	• Restoration increased seismic resilience but also altered stress distributions	• Limited assessment of long-term restoration effects • Lacks progressive collapse interaction studies

Author	Title	Year	Modelling Strategies					Methodology	Findings	Research Gaps
			Shell	Solid	Linear	Nonlinear	Modal			
İrfan Kocaman	*Examination of the Damage Limits and Collapse Mechanism of Adıyaman Ulu Mosque with Finite Element Model*	2024	✖	✓	✓	✓	✓	• Developed a **3D FEM model** using solid elements in ANSYS (SOLID65) with the Willam-Warnke material model. • Conducted **time-history analyses** with four ground motions to evaluate seismic behaviour. • Performed **modal and pushover analyses** to determine drift limits and collapse mechanisms.	• The collapse mechanisms observed in the model aligned with the actual damage sustained by the Mosque during the 2023 Kahramanmaraş earthquakes. • Displacement-based earthquake performance limits were determined and found to be lower than regulatory recommendations. • Identified the column and arch systems as the most seismically vulnerable parts of the Mosque.	• Did not use specific **ground motion records** from the Kahramanmaraş earthquake. • Ignored interaction effects of **nearby buildings**, which significantly influence urban seismic behaviour. • Generalized material properties limit model specificity and applicability to other heritage structures.
İzol et al.	*Seismic performance of masonry structures after 06 February 2023 earthquakes*	2024	✓	✓	✓	✓	✓	• Field surveys • Nonlinear time-history analysis on rural masonry buildings	• Identified shear and out-of-plane failures in masonry walls • Emphasized the role of poor materials	• Limited urban context assessment • No evaluation of neighbouring building collapse effects

Author	Title	Year	Modelling Strategies					Methodology	Findings	Research Gaps
			Shell	Solid	Linear	Nonlinear	Modal			
Kocaman et al.	*The effect of Kahramanmaraş earthquakes on historical Malatya Yeni Mosque*	2024	✖	✓	✓	✓	✓	• Field surveys • FEM analysis with city acceleration data	• Identified dome, minaret, and column failures due to seismic action • Emphasized strengthening needs	• No assessment of domino collapses effects. • Limited assessment of progressive collapse mechanisms
Kiral et al.	*A case study comparing seismic retrofitting techniques for a historically significant masonry building's minaret*	2024	✖	✓	✓	✓	✓	• SAP2000-based modelling of retrofitting techniques • Base isolation, viscous dampers, CFRP	• Viscous dampers were effective for minaret protection, while base isolation reduced stress overall	• No real-world validation of damping effectiveness • Lacks evaluation of entire building interactions
Malomo & DeJong	*M-DEM simulation of seismic pounding between adjacent masonry structures*	2024	✖	✓	✖	✓	✖	• Developed a Macro-Distinct Element Modelling (M-DEM) approach to simulate pounding damage in unreinforced masonry structures. • Validated against shake-table tests.	• M-DEM accurately reproduces base shear and interface opening but underestimates floor displacement demand. • Provides a low-cost computational alternative.	• Need for further refinement of M-DEM predictions. • Requires better calibration for transverse direction displacement.

Appendix B. Rayleigh Damping Parameter

From two eigenvalue analysis model, which are:

a. Model with minaret included, and
b. Model with minaret excluded.

It was found that both models had dominant frequency which lies around 4.6 – 11.9 Hz range. To be more precise, model a had dominant frequency at range of 4.678 to 11.937 Hz, while model b at 4.681 to 11.860 Hz. Given the nature of nonlinear dynamic analysis which require the input for Rayleigh Damping coefficients, which are formulated as

$$C = \alpha M + \beta K$$

Where

$$\beta = \frac{2\zeta}{\omega_1 + \omega_2}, and\ \alpha = \beta\omega_1\omega_2 = \frac{2\zeta\omega_1\omega_2}{\omega_1 + \omega_2}$$

With ζ denoted target damping (of 3% for this research), and $\omega_i = 2\pi f_i$, calculated according to observed frequency range.

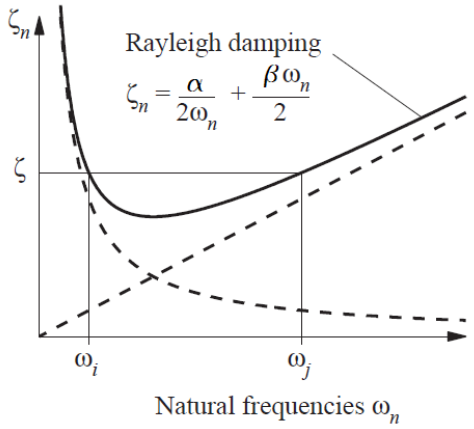

Figure B-1 Illustration of Rayleigh Damping

Based on the natural frequencies range of model a and model b, Rayleigh damping coefficients are formulated as

Table B-1 Rayleigh Damping Parameters

Model	a (Minaret Included)	b (Minaret Excluded)
ω_1 [rad/s]	29.390	29.416
ω_2 [rad/s]	75.002	74.518
α [s^{-1}]	1.267	1.265
β [s]	5.750 x 10^{-4}	5.770 x 10^{-4}

While the difference between the parameter's values are minimal, since the dominant modes are consistently clustered within similar range, for the purposes of this research, values from model b will be used.

Bibliography

- Abdel Raheem, S. E., Fooly, M. Y. M., Abdel Shafy, A. G. A., Taha, A. M., Abbas, Y. A., & Abdel Latif, M. M. S. (2019). Numerical simulation of potential seismic pounding among adjacent buildings in series. *Bulletin of Earthquake Engineering, 17(2)*, 439–471. https://doi.org/10.1007/s10518-018-0455-0

- Aşıkoğlu, A., Avşar, Ö., Lourenço, P. B., & Silva, L. C. (2019). Effectiveness of seismic retrofitting of a historical masonry structure: Kütahya Kurşunlu Mosque, Türkiye. *Bulletin of Earthquake Engineering, 17*, 3365–3395. https://doi.org/10.1007/s10518-019-00603-6

- Aşıkoğlu, A., Vasconcelos, G., Lourenço, P. B., & Pantò, B. (2020). Pushover analysis of unreinforced irregular masonry buildings: Lessons from different modeling approaches. *Engineering Structures, 218*, 110830. https://doi.org/10.1016/j.engstruct.2020.110830

- Betti, M., & Vignoli, A. (2011). Numerical assessment of the static and seismic behaviour of the Basilica of Santa Maria all'Impruneta (Italy). *Construction and Building Materials, 25*(10), 4308–4324. https://doi.org/10.1016/j.conbuildmat.2010.12.028

- Bianchini, N., Ciocci, M. P., Solarino, F., Romanazzi, A., Ramirez, R., D'Anna, J., & Aşıkoğlu, A. (2024). Influence of wall-to-floor connections and pounding on pre- and post-diction simulations of a masonry building aggregate tested on a shaking table. *Bulletin of Earthquake Engineering, 22*, 6141–6161. https://doi.org/10.1007/s10518-023-01641-x

- Brown, T., & Elshaer, A. (2022). Pounding of structures at proximity: A state-of-the-art review. *Journal of Building Engineering, 48*, 103991. https://doi.org/10.1016/j.jobe.2022.103991

- D'Altri, A. M., Sarhosis, V., Milani, G., Rots, J., Cattari, S., Lagomarsino, S., Sacco, E., Tralli, A., Castellazzi, G., & de Miranda, S. (2020). Modeling strategies for the computational analysis of unreinforced masonry structures: Review and classification. *Archives of Computational Methods in Engineering, 27*, 1153–1185. https://doi.org/10.1007/s11831-019-09351-x

- del Coz Díaz, J. J., Lozano Martínez-Luengas, A., Adam, J. M., & Martín Rodríguez, A. (2011). Non-linear hygrothermal failure analysis of an external clay brick wall by FEM – A case study. *Construction and Building Materials, 25*(10), 4454–4464. https://doi.org/10.1016/j.conbuildmat.2010.12.039

- Ergün, M., & Tayfur, B. (2024). Evaluation of the seismic performance pre- and post-restoration of a masonry clock tower's FE model updated via experimental and optimization methods. *Engineering Failure Analysis, 158*, 107986. https://doi.org/10.1016/j.engfailanal.2024.107986

- Ficici, S. [@Serkan_Ficici]. (2023, February 9). *Adıyaman Ulu Mosque before the earthquake* [Photograph]. X (formerly Twitter). https://x.com/Serkan_Ficici/status/1623732177614561283.
- Giamundo, V., Sarhosis, V., Lignola, G. P., Sheng, Y., & Manfredi, G. (2014). Evaluation of different computational modelling strategies for the analysis of low strength masonry structures. *Engineering Structures, 73*, 160–169. https://doi.org/10.1016/j.engstruct.2014.05.007
- Işık, E., Avcil, F., Arkan, E., Büyüksaraç, A., İzol, R., & Topalan, M. (2023). Structural damage evaluation of Mosques and minarets in Adıyaman due to the 06 February 2023 Kahramanmaraş earthquakes. *Engineering Failure Analysis, 151*, 107345. https://doi.org/10.1016/j.engfailanal.2023.107345
- Karanikoloudis, G., & Lourenço, P. B. (2018). Structural assessment and seismic vulnerability of earthen historic structures: Application of sophisticated numerical and simple analytical models. *Engineering Structures, 160*, 488–509. https://doi.org/10.1016/j.engstruct.2017.12.023
- Kiral, A., Ergün, M., Tonyali, Z., & Artar, M. (2024). A case study comparing seismic retrofitting techniques for a historically significant masonry building's minaret. *Engineering Failure Analysis, 166*, 108873. https://doi.org/10.1016/j.engfailanal.2024.108873
- Kocaman, I. (2024). Examination of the damage limits and collapse mechanism of Adıyaman Ulu Mosque with finite element model. *Structures, 70*, 107787. https://doi.org/10.1016/j.istruc.2024.107787
- Kocaman, I., Mercimek, Ö., Gürbüz, M., Erbaş, Y., & Anıl, Ö. (2024). The effect of Kahramanmaraş earthquakes on historical Malatya Yeni Mosque. *Engineering Failure Analysis, 161*, 108310. https://doi.org/10.1016/j.engfailanal.2024.108310
- Lourenço, P. B. (1998). Experimental and numerical issues in the modelling of the mechanical behaviour of masonry. *Structural Analysis of Historical Constructions II*, P. Roca, J. L. González, E. Oñate, & P. B. Lourenço (Eds.), CIMNE, Barcelona.
- Lourenço, P. B. (2001). Analysis of historical constructions: From thrust-lines to advanced simulations. In *Historical Constructions*, P. B. Lourenço & P. Roca (Eds.), Guimarães, pp. 91-116.
- Lourenço, P. B. (2002). Computations on historic masonry structures. *Progress in Structural Engineering and Materials, 4*(3), 301–319. https://doi.org/10.1002/pse.120
- Lourenço, P. B., & Gaetani, A. (2019). Finite element analysis for building assessment. CRC Press. https://doi.org/10.1201/9780429426503
- Lourenço, P. B., Mendes, N., Ramos, L. F., & Oliveira, D. V. (2011). Analysis of masonry structures without box behavior. *International Journal of Architectural Heritage, 5*(4-5), 369-382. https://doi.org/10.1080/15583058.2010.528824

- Lourenço, P. B., Krakowiak, K. J., Fernandes, F. M., & Ramos, L. F. (2007). Failure analysis of Monastery of Jerónimos, Lisbon: How to learn from sophisticated numerical models. *Engineering Failure Analysis, 14*(2), 280–300. https://doi.org/10.1016/j.engfailanal.2006.02.002
- Malomo, D., & DeJong, M. J. (2024). M-DEM simulation of seismic pounding between adjacent masonry structures. *Bulletin of Earthquake Engineering, 22*, 6067–6092. https://doi.org/10.1007/s10518-022-01545-2
- Maniatakis, C. A., Spyrakos, C. C., Kiriakopoulos, P. D., & Tsellos, K. P. (2018). Seismic response of a historic church considering pounding phenomena. *Bulletin of Earthquake Engineering, 16*, 2913–2941. https://doi.org/10.1007/s10518-017-0293-5
- Miari, M., Choong, K. K., & Jankowski, R. (2019). Seismic pounding between adjacent buildings: Identification of parameters, soil interaction issues and mitigation measures. *Soil Dynamics and Earthquake Engineering, 121*, 135–150. https://doi.org/10.1016/j.soildyn.2019.02.024
- İzol, R., Işık, E., Avcil, F., Arslan, M. H., Arkan, E., & Büyüksaraç, A. (2024). Seismic performance of masonry structures after 06 February 2023 earthquakes; site survey and FE modelling approach. *Soil Dynamics and Earthquake Engineering, 186*, 108904. https://doi.org/10.1016/j.soildyn.2024.108904
- Roca, P., Lourenço, P. B., & Gaetani, A. (2019). Historic construction and conservation: Materials, systems and damage. Routledge. https://doi.org/10.4324/9780429506212
- Silva, L. C., Mendes, N., Lourenço, P. B., & Ingham, J. (2018). Seismic structural assessment of the Christchurch Catholic Basilica, New Zealand. *Structures, 15*, 115–130. https://doi.org/10.1016/j.istruc.2018.06.004
- Tomaževič, M. (1999). Earthquake-resistant design of masonry buildings. Imperial College Press.